

AD-A161 889

ANALYTICAL PREDICTION OF TURBULENT HEAT TRANSFER  
PARAMETERS(U) DUKE UNIV DURHAM NC DEPT OF MECHANICAL  
ENGINEERING AND MATERIALS SCIENCE A BEJAN APR 85

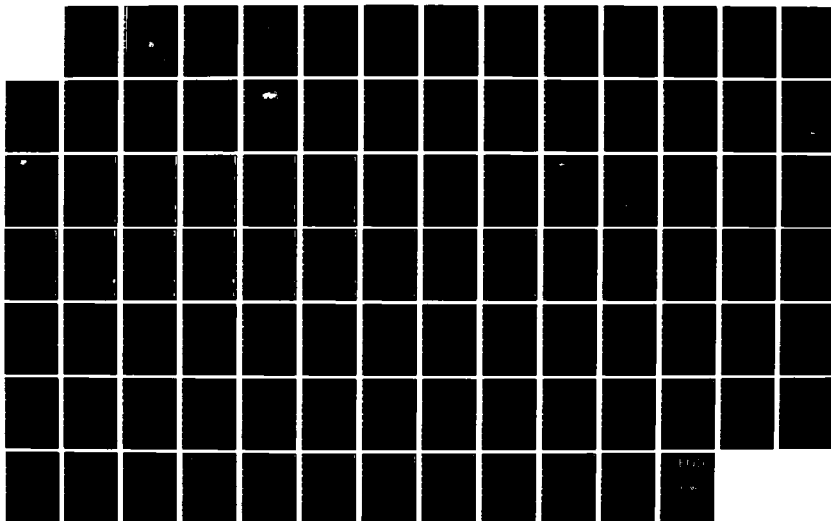
1/2

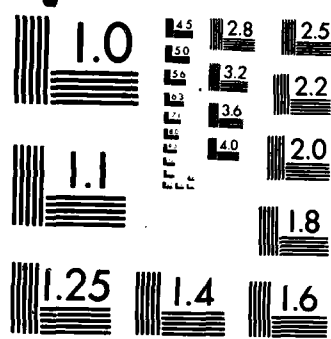
UNCLASSIFIED

DU-AB-1 N00014-79-C-0006

F/G 20/4

NL





MICROCOPY RESOLUTION TEST CHART  
NATIONAL BUREAU OF STANDARDS-1963-A

5

# Department of Mechanical Engineering and Materials Science

AD-A161 889

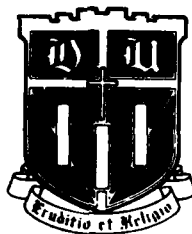
Analytical Prediction of Turbulent  
Heat Transfer Parameters

-The Final Report-

Adrian Bejan

DU-AB-1

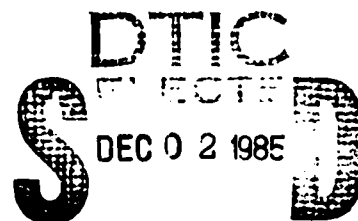
April 1985



**Duke University  
School of Engineering**

Durham, North Carolina 27706

THIS FILE COPY



D

**DISTRIBUTION STATEMENT A**

Approved for public release;  
Distribution Unlimited

85 11 26 002

Analytical Prediction of Turbulent  
Heat Transfer Parameters

-The Final Report-

Adrian Bejan

DU-AB-1

April 1985

DTIC  
ELECTE  
S DEC 0 2 1985 D  
D

## **DISCLAIMER NOTICE**

**THIS DOCUMENT IS BEST QUALITY  
PRACTICABLE. THE COPY FURNISHED  
TO DTIC CONTAINED A SIGNIFICANT  
NUMBER OF PAGES WHICH DO NOT  
REPRODUCE LEGIBLY.**

Unclassified

SECURITY CLASSIFICATION OF THIS PAGE (When Data Entered)

REPORT DOCUMENTATION PAGE		READ INSTRUCTIONS BEFORE COMPLETING FORM
1. REPORT NUMBER DU-AB-1	2. GOVT ACCESSION NO. <b>AD-A161889</b>	3. RECIPIENT'S CATALOG NUMBER
4. TITLE (and Subtitle) Analytical Prediction of Turbulent Heat Transfer Parameters: The Final Report		5. TYPE OF REPORT & PERIOD COVERED Final, 10/1/80-9/30/84
		6. PERFORMING ORG. REPORT NUMBER
7. AUTHOR(s) Adrian Bejan		8. CONTRACT OR GRANT NUMBER(s) N00014-79-C-0006
9. PERFORMING ORGANIZATION NAME AND ADDRESS Department of Mechanical Engineering and Materials Science, Duke University Durham, NC 27706		10. PROGRAM ELEMENT, PROJECT, TASK AREA & WORK UNIT NUMBERS Program Element 61153N24 Project RR024-03, Task Area RR024-03-02, Work Unit NR097-43
11. CONTROLLING OFFICE NAME AND ADDRESS Office of Naval Research 800 N. Quincy Street Arlington, VA 22217		12. REPORT DATE April 1985
14. MONITORING AGENCY NAME & ADDRESS (if different from Controlling Office)		13. NUMBER OF PAGES
		15. SECURITY CLASS. (of this report)
		15a. DECLASSIFICATION/DOWNGRADING SCHEDULE
16. DISTRIBUTION STATEMENT (of this Report) Approved for public release; distribution unlimited		
17. DISTRIBUTION STATEMENT (of the abstract entered in Block 20, if different from Report) Same as Block #16		
18. SUPPLEMENTARY NOTES		
19. KEY WORDS (Continue on reverse side if necessary and identify by block number) Heat transfer, turbulent flow, irreversibility, buckling theory.		
20. ABSTRACT (Continue on reverse side if necessary and identify by block number) The objective of this research is to construct a purely theoretical foundation for the phenomenon of turbulent heat transfer. The present final report summarizes the research accomplished during the four-year funded period. The strategy of this research is shown to have consisted of: (1) identifying the domain covered only by the present theory; and (2) identifying the intersection between the present theory and older theories. A complete summary of published articles, books, and theses is appended.		

DD FORM 1473 1 JAN 73

EDITION OF 1 NOV 65 IS OBSOLETE

SECURITY CLASSIFICATION OF THIS PAGE (When Data Entered)

ANALYTICAL PREDICTION OF TURBULENT HEAT TRANSFER PARAMETERS:

THE FINAL REPORT

April 1985

Adrian Bejan  
Professor  
Department of Mechanical Engineering and Materials Science  
Duke University  
Durham, NC 27706

Prepared for

M. K. Ellingsworth  
Program Monitor  
The Office of Naval Research  
Arlington, Virginia 22217

Accession For	
NTIS CRA&I	<input checked="checked" type="checkbox"/>
DTIC TAB	<input type="checkbox"/>
Unannounced	<input type="checkbox"/>
Justification	
By	
Distribution/	
Availability Codes	
Dist	Avail and/or special
A-1	23



Under Contract No. N00014-79-0006, Work Unit 097-431. Approved for public release; distribution unlimited. Reproduction in whole or in part is permitted for any purpose of the United States Government.

## THE BUCKLING THEORY OF TURBULENT FLOW

The research overviewed in this final report had as primary objective the establishment of a purely theoretical foundation for the existence of turbulent flows and engineering formulas that summarize the transport potential of such flows. From the early research - proposal stage, this work reflected my view that "tradition" has given us a fluid mechanics research methodology that is generally divorced from thermodynamics, and, with special regard to turbulence research, a research methodology that is divorced from theory. That even the analytical work in 20th century turbulence research is rooted in empiricism is best illustrated by how the empirical notion of "eddy" is never questioned and conveniently hidden behind the time-averaged terminology inherited from Osborne Reynolds.

The present research project was conducted over the three year period that coincided with the academic years 1980-81, 81-82, and 82-83. A one-year extension was added to the original contract period in order to facilitate the completion of ongoing thesis work and my own writings and preparations for the 1984 sabbatical leave and move to Duke University. Although the actual work is already documented in detail in the three annual reports [1-3], I welcome this opportunity to review it one more time and to stress its position relative to pre-1980 thinking.

The present work - the buckling theory of turbulent flow - departs from fluids mechanics tradition in two important respects. First, this new theory focuses on the equilibrium of a finite-size flow system (e.g., jet, wake, boundary layer), as opposed to the equilibrium of the infinitesimally small fluid packet used as subject in the Navier-Stokes equations. Second, it relies on the thermodynamics inspired idea that the flow system possess conservative mechanical properties (e.g. elasticity in bending) if it is



inviscid.

The analytical conclusion of the buckling theory is that an inviscid stream of finite transversal dimension  $D$  can buckle into a sinusoidal shape whose longitudinal wavelength  $\lambda_B$  scales with  $D$ . In this manner the buckling theory unveils two obvious but previously unexplained scales of the stream, the buckling (meandering) wavelength  $\lambda_B$  and the time scale associated with the growth of the deformation (i.e., the time of eddy formation)  $t_B \sim \lambda_B/(V/2)$ , where  $V$  is the longitudinal velocity scale of the flow. This new theory is therefore a theory of large scale orderly structure in turbulent flow.

The buckling theory - its enunciation, experimental verification and application to heat transfer engineering - has been published extensively through three equally important channels of peer review: journal articles, listed chronologically as Refs. [4-15], graduate theses [16-20] and books [21-23]. The permanent contact with the research community is greatly responsible for the diversity of the topics studied from the point of view of stream buckling, and for the balance between the theoretical and experimental segments of this study.

The strategy that served as guide for the definition of individual research topics during the four-year period consisted of identifying:

- I. The boundaries of the new theoretical viewpoint, i.e., how far the theory extends into the territory that is not explained by any existing theory.
- II. The intersections between the buckling theory and existing theories, i.e., pinpointing the phenomena that are explained by two theories.

If the domain labeled B in Fig. 1 represents the territory discovered until

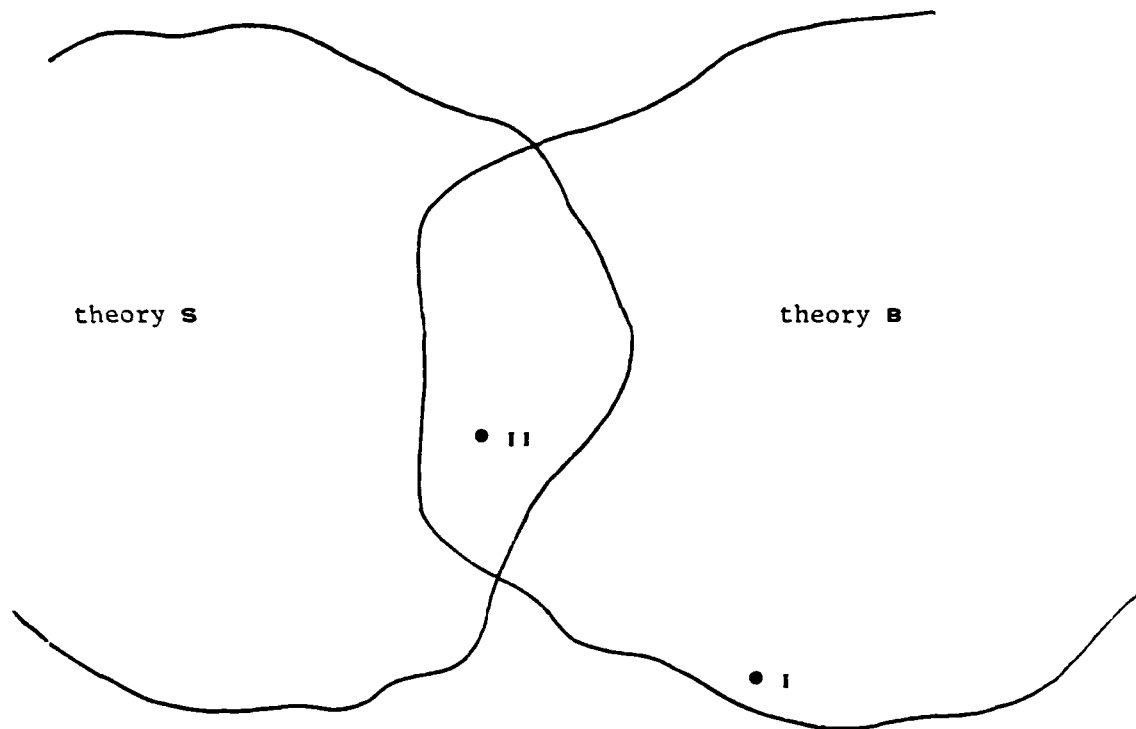


Figure 1. Charting the domain seen from a new theoretical point of view, and discovering the intersections with domains covered by older theories.

today from the point of view of Buckling theory, and if the domain S represents the things explained by an existing theory (e.g., hydrodynamic Stability theory), then the phenomenon plotted as point I is an example of work done on front (I). Specific examples of advances of type I are the explanation of the observed sinusoidal deformation during the transition to turbulence\* (Ref. [22], chapter 6), the Colburn analogy between momentum and heat transfer in turbulent flow (Ref. [22], chapter 7) and the "entrainment hypothesis" or the linear time-averaged growth of all turbulent mixing regions (Ref. [22], chapter 8).

The intersection between the new theory and an existing theory is represented by points labeled II in Fig. 1. One discovery of type II is the notion that the transition to turbulence in flows of many geometries and origins is associated universally with a "local Reynolds number" of order  $O(10^2)$  (Ref. [22], chapter 6; the "local Reynolds number" is based on the local longitudinal velocity scale and the local transversal length scale). Although this apparently universal criterion of transition to turbulence is consistent with both theories [10,11], it was first stated in the realm of buckling theory [4].

As a second example of an advance of type II - this time an observation explained by both S and B, but historically stated first in S - I use this opportunity to communicate that the classical Richardson number criterion regarding the instability of a density-stratified flow follows in very few steps from the main result of the buckling theory. Consider the inviscid jet of transversal length scale D and longitudinal velocity V sketched in Fig. 2. According to the buckling theory, since the stream is inviscid it has the

---

\* The theory of hydrodynamic stability cannot explain this observation: recall that in stability theory the "disturbance" shape is arbitrary and assumed given.

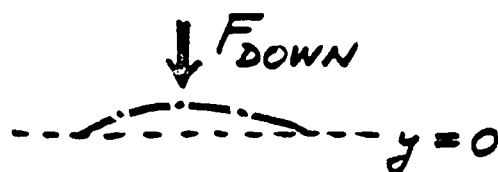
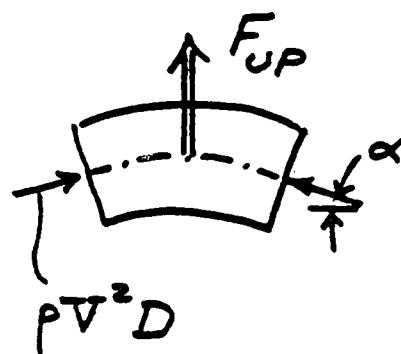
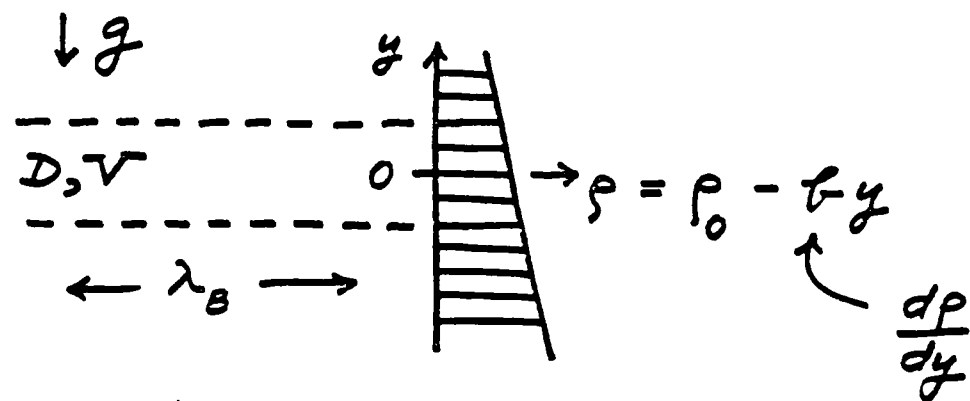


Figure 2. Determining the criterion for stability in density-stratified inviscid shear flow via buckling theory.

property to buckle with a longitudinal wavelength  $\lambda_B$ : as demonstrated in chapter 4 of Ref. [21], the subsequent and certain instability of the infinitesimally buckled stream can be thought of as the effect of the lateral net force  $F_{up}$  that acts on a control volume (elbow) of height  $D$  and length  $\lambda_B/2$ ,

$$F_{up} \sim \rho V^2 D \alpha, \quad (1)$$

where the angle  $\alpha$  is infinitesimally small.

The lateral instability and eventual roll-up (eddy formation) may not occur if the flow proceeds through a stably stratified environment

$$\rho(y) = \rho_0 - by, \quad (2)$$

where  $b = -d\rho/dy > 0$ . In such cases the finite-size control volume will be pushed down by a restoring force of order

$$F_{down} \sim \lambda_B D g \Delta \rho \quad (3)$$

where  $\Delta \rho \sim b \alpha \lambda_B$  is the density defect scale of the control volume.

The condition for stability can then be written sequentially as

$$F_{down} > F_{up} \quad (4)$$

$$\lambda_B D g b \alpha \lambda_B > \rho V^2 D \alpha \quad (5)$$

$$\frac{gb}{\rho \left(\frac{V}{D}\right)^2} > \left(\frac{D}{\lambda_B}\right)^2 \quad (6)$$

The left-hand-side in this inequality is the Richardson number. According to the buckling theory the right-hand-side is always a constant of order  $O(1)$ .

In conclusion, the stability criterion via buckling theory is

$$Ri > O(1) \quad (7)$$

The same criterion is a classical result of hydrodynamic stability theory, however, the analysis summarized as eqs. (1) - (7) is orders of magnitude simpler than the corresponding hydrodynamic stability analysis.

In conclusion, in Fig. 1 the Richardson number criterion (7) is covered by theory S and B: this, however, does not mean that theory S alone (or theory B alone) explains everything about transition in stably stratified shear flow. For example, theory S still does not explain the regular sinusoidal deformation that serves as initial condition for hydrodynamic instability.

The work started on fronts I and II is far from over. The success of buckling theory and the fact that none of the claims made so far on behalf of this theory have been proven false in the post-1980 literature, are two good reasons why this theory will continue to attract attention. Considering the naked simplicity of buckling theory, and recalling the thermodynamics origins of the essential idea, I invite my colleagues to join in this research and to give new life to the words spoken once by Josiah Willard Gibbs:

"One of the principal objects of theoretical research in any department of knowledge is to find the point of view from which the subject appears in its greatest simplicity."

Adrian Bejan  
Duke University  
April 16, 1985

## PUBLICATIONS

### Reports

1. A. Bejan, "Analytical Prediction of Turbulent Heat Transfer Parameters: The First Annual Report," Report CUMER 81-3, December 1981.
2. A. Bejan, "Analytical Prediction of Turbulent Heat Transfer Parameters: The Second Annual Report," Report CUMER 82-6, December 1982.
3. A. Bejan, "Analytical Prediction of Turbulent Heat Transfer Parameters: The Third Annual Report," Report CUMER 83-4, December 1983.

### Journal Articles

4. A. Bejan, "On the Buckling Property of Inviscid Jets and the Origin of Turbulence," Letters in Heat and Mass Transfer, Vol. 8, May/June 1981, pp. 187-194.
5. A. Bejan, "Comments on Viscous Buckling of Thin Fluid Layers," The Physics of Fluids, Vol. 24, September 1981, pp. 1764, 1765.
6. A. Bejan, "The Meandering Fall of Paper Ribbons," The Physics of Fluids, Vol. 25, No. 5, May 1982, pp. 741, 742.
7. A. Bejan, "Theoretical Explanation for the Incipient Formation of Meanders in Straight Rivers," Geophysical Research Letters, Vol. 9, No. 8, August 1982, pp. 831-834.
8. M. G. Stockman, and A. Bejan, "The Nonaxisymmetric (Buckling) Flow Regime of Fast Capillary Jets," The Physics of Fluids, Vol. 25, No. 9, September 1982, pp. 1506-1511.
9. A. Bejan, "Theory of Instantaneous Sinuous Structure in Turbulent Buoyant Plumes," Warme-und Stoffubertragung, Vol. 16, No. 4, 1982, pp. 237-242.
10. A. Bejan, and G. R. Cunnington, "Theoretical Considerations of Transition to Turbulence in Natural Convection near a Vertical Wall," International Journal of Heat and Fluid Flow, Vol. 4, September 1983, pp. 131-139.
11. S. Kimura, and A. Bejan, "Mechanism for Transition to Turbulence in Buoyant Plume flow," International Journal of Heat and Mass Transfer, Vol. 26, October 1983, pp. 1515-1532.
12. R. Anderson, and A. Bejan, "Buckling of a Turbulent Jet Surrounded by a Highly Flexible Duct," The Physics of Fluids, Vol. 26(11), November 1983, pp. 3193-3200.
13. S. Kirmura, and A. Bejan, "The Buckling of a Vertical Liquid Column," Journal of Fluids Engineering, Vol. 105, December 1983, pp. 469-473.

14. K. R. Blake, and A. Bejan, "Experiments on the Buckling of Thin Fluid Layers Undergoing End-Compression," Journal of Fluids Engineering, Vol. 106, March 1984, pp. 74-78.
15. R. Anderson, and A. Bejan, "The Instability of a Round Jet Surrounded by an Annular Shear Layer," forthcoming in the Journal of Fluids Engineering, 1985.

#### M.S. Theses

16. M. G. Stockman, "The Buckling Instability of Capillary Jets," 1981.
17. K. R. Blake, "Viscous Buckling of Thin Fluid Layers Undergoing End Compression," 1982.
18. A. Anand, "Transition to Turbulence in Rivulet flow between Two Parallel Plates," 1983.

#### Ph.D. Theses

19. R. Anderson, "Buckling of Turbulent Jets," 1983.
20. S. Kimura, "Buckling Flow and Transition to Turbulence in Axisymmetric Plumes," 1983.

#### Books

21. A. Bejan, Entropy Generation through Heat and Fluid Flow, Wiley, New York, 1982, pp. 264; Solutions Manual, Wiley, New York, 1984, pp. 50.
22. A. Bejan, Convection Heat Transfer, Wiley, New York, 1984, pp. 498; Solutions Manual, Wiley, New York, 1984, pp. 218.
23. A. Bejan, "The Method of Scale Analysis: Natural Convection in Fluids," Chapter in Natural Convection: Fundamentals and Applications, Eds. W. Aung, S. Kakac, and R. Viskanta, Hemisphere, Washington, D. C., 1985.



**JOURNAL ARTICLES**

ON THE BUCKLING PROPERTY OF INVISCID JETS AND  
THE ORIGIN OF TURBULENCE

Adrian Bejan  
Department of Mechanical Engineering  
University of Colorado, Boulder, Colorado

(Communicated by J.P. Hartnett and W.J. Minkowycz)

ABSTRACT

This letter outlines the analogy which exists between inviscid jets and elastic columns in axial compression. It is shown that straight inviscid jet columns possess the property of sinusoidal infinitesimal buckling. The buckling wavelength scales with the transversal dimension of the jet. The repeated buckling and breakup of the jet column is responsible for the observed whiplash motion of turbulent jets. The buckling theory predicts correctly the natural frequency of the whiplash motion and the Reynolds number for the laminar-turbulent transition in free jet flow.

Introduction

One aspect of jet turbulence receiving increased attention is the large scale "orderly" structure with a length scale of the same order as the jet diameter. Crow and Champagne [1] showed that as the Reynolds number increases from  $10^2$  to  $10^3$ , the whiplash motion of jets evolves from a sinusoid to a helix and eventually to a train of axisymmetric waves. Similar observations have been reported by Reynolds [2]. The characteristic snake-like shape of a turbulent round jet is shown very clearly in Fig. 1.

The purpose of this letter is to offer a theoretical explanation for the observed large-scale periodic structure of turbulent jets. The explanation is founded on a very interesting analogy which exists between jet flows and slender elastic columns in axial compression [4]. It may be recalled that Euler's theory of infinitesimal buckling (indifferent equilibrium) in axially compressed columns rests on only two premises [5,6]:

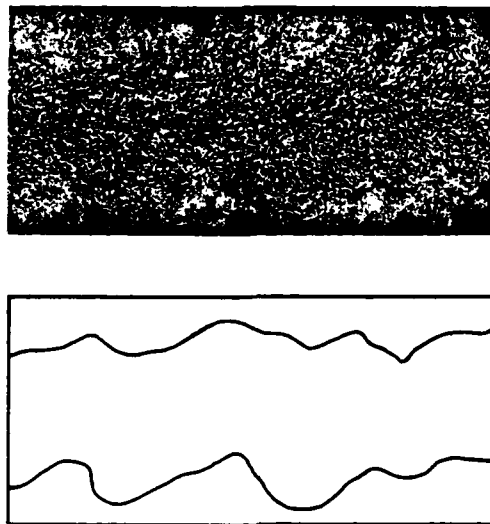


FIG. 1  
The characteristic meandering path of a turbulent jet (after Yih [3]).

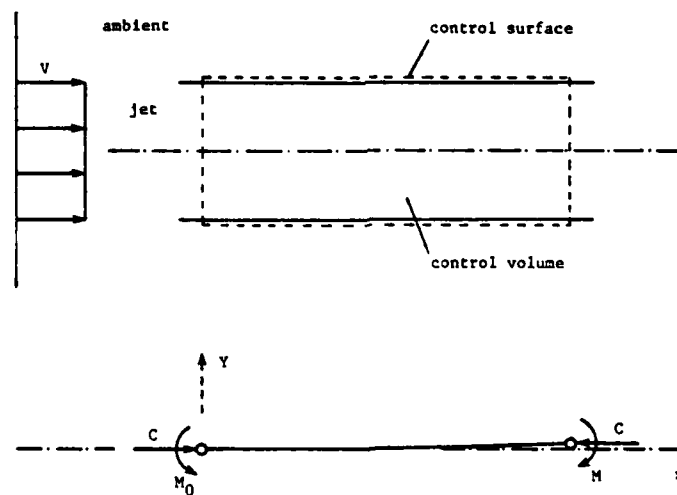


FIG. 2  
The static equilibrium of the envelope surrounding a straight jet.

- (i) the slender column is straight and in axial compression;
- (ii) if subjected to a separate bending test, the column develops in its cross-section a resistive bending moment which is proportional to the induced curvature.

Slender elastic columns, of course, meet these two conditions. However, it is shown in the next section that exactly the same conditions are met by inviscid streams discharging freely into larger reservoirs. Consequently, the column (control volume) occupied by an inviscid stream buckles sinusoidally, and the stream mixes periodically with the stagnant ambient. From this result, we conclude that the natural property of inviscid streams is to follow a sinusoidal (meandering) path as they travel through a stagnant ambient. This natural property of inviscid flow is the basis for the unexplained turbulent behavior of fluids.

#### The Static Equilibrium of the Jet Envelope

Consider a straight inviscid jet of density  $\rho$ , uniform velocity  $V$  and cross-sectional area  $A$ , as shown in Fig. 2. The static pressure inside the jet and in the ambient fluid is  $P_0$ . Imagine now a stationary envelope (control surface) which surrounds a certain length of the jet. This envelope and two transversal end-cuts define a stationary control volume.

In the spirit of the thermodynamics of open flow systems [7], the only forces which act on this control volume are the inlet and outlet compressive forces

$$C = \rho A V^2 \quad (1)$$

Forces  $C$  are shown schematically in the lower half of Fig. 2 where the control volume is symbolized by the solid line. At this point we conclude that the fluid-filled column represented by the control volume satisfies condition (i) for buckling.

When the control volume is slightly curved, each face of the transversal cut is exposed not only to a compressive force but also to a bending moment. Consider the separate bending test in which the jet is held (forced to flow) in a slightly curved duct. The radius of curvature of the duct,  $R_\infty$ , is infinitely greater than the transversal dimension of the jet,  $D$ . Bernoulli's equation for a streamline [8] dictates

$$\frac{1}{2} \rho V^2 + P_0 = \frac{1}{2} \rho v^2(z) + P(z) \quad (2)$$

where the right-hand-side of the equation corresponds to the curved duct. Coordinate  $z$  is measured radially from the jet centerline towards the center of curvature. Radial equilibrium of the jet fluid in the curved duct requires also [9]

$$-\frac{\rho v^2(z)}{R_\infty} = \frac{\partial P}{\partial z} \quad (3)$$

In the limit of vanishingly small curvature,  $D/R_\infty \rightarrow 0$ , equations (2) and (3) yield

$$v(z) = V(1 + \frac{z}{R_\infty}) \quad (4)$$

$$P(z) = P_0 - \frac{\rho V^2 z}{R_\infty} \quad (5)$$

The bending moment acting over the cross-section is

$$M = \iint_A (\rho v^2 + P) z \, dA = \frac{\rho V^2 I}{R_\infty} \quad (6)$$

where  $I = \iint_A z^2 \, dA$  is the area moment of inertia of the jet cross-section.

In conclusion, the cross-sectional bending moment  $M$  of a nearly straight jet column is proportional to the curvature of the column,  $1/R_\infty$ . This means that the inviscid jet column satisfies condition (ii) for the infinitesimal buckling of a straight column.

Consider now the static equilibrium of the straight jet envelope shown in Fig. 2. Clearly, the axial compressive forces  $C$  balance each other. In addition, the excentricity bending moment  $CY$  -- however small -- must be balanced at all times by the cross-sectional bending moment [10]

$$CY + M_0 - M(x) = 0 \quad (7)$$

Noting that  $1/R_\infty = -d^2Y/dx^2$ , the rotational equilibrium condition (7) constitutes a differential equation for the equilibrium centerline  $Y(x)$ ,

$$\rho V^2 I \frac{d^2 Y}{dx^2} + \rho V^2 A Y + M_0 = 0 \quad (8)$$

The solution satisfying the nozzle conditions  $Y = Y' = 0$  at  $x = 0$  is

$$Y(x) = K[\cos(x\sqrt{A/I}) - 1] \quad (9)$$

where the amplitude  $K$  is indeterminate and infinitely small compared with the transversal length scale  $\sqrt{I/A}$  or  $D$ .

We arrive at the important conclusion that the equilibrium centerline of the jet envelope is a sinusoid of infinitely small amplitude. The wavelength of this trajectory scales only with the transversal dimension of the jet,

$$\lambda = 2\pi\sqrt{I/A} \quad (10)$$

For example,  $\lambda/D = \pi/2$  for a round jet of diameter  $D$ , and  $\lambda/D = \pi/\sqrt{3}$  for a flat (two-dimensional) jet of thickness  $D$ . An analysis of the meandering contour of the round jet of Fig. 1 yields  $\lambda/D \approx 1.2$  which is in good agreement with the theoretical value of 1.57 (it is very likely that the 24% discrepancy between the two values is caused by the fact that the contour shown in Fig. 1 overestimates the real diameter of the turbulent jet).

#### Formation of Large-Scale Vortices

The analogy between the infinitesimal buckling of elastic columns and inviscid jet envelopes terminates with the equilibrium centerline given by equation (9). Whereas in slender elastic columns the equilibrium of the small-amplitude sinusoid is indifferent [10], in an inviscid jet the equilibrium is unstable. The unstable equilibrium of the inviscid column is described very well by the classical theory of hydrodynamic instability [11]. The slightest deviation of the jet from its rectilinear shape leads to the formation of lateral "lift" forces which consistently tend to amplify the deformation. As a result, the inviscid jet breaks up periodically as its overextended elbows penetrate and mix with the stagnant ambient. The degenerated elbow region becomes a "large scale turbulent structure" [1] which continues to move downstream with a speed of order  $V/2$ .

The repeated buckling and breakup phenomenon accounts for the observed whiplash and fluctuating motion of turbulent jets. The period of this fluctuation scales with the buckling time  $t_B = \lambda/V$ , i.e., with the time of fluid travel between successive elbows (breaks) in the jet column. The natural frequency of jet fluctuation can be expressed in dimensionless form as a Strouhal number

$$St = \frac{D}{t_B V} = \frac{D}{\lambda} \quad (11)$$

which, as shown in the preceding section, has a value of order 0.5. This order

of magnitude estimate agrees very well with experimental measurements of the natural frequency of turbulent jets exposed to a range of external excitation frequencies. For example, Bechert and Pfizenmaier [12] reported  $St = 0.5$  for maximum amplification of broadband jet noise. Most recently, Acton [13] conducted a computational simulation of a round turbulent jet by modeling the shear layer as a succession of discrete vortex ring elements. Acton showed that the natural periodicity of the round jet was  $St \approx 0.47$ , and that the jet was most sensitive when forced at approximately the same frequency ( $St = 0.5$ ).

#### The Transition to Turbulence

The buckling property and fluctuating nature of inviscid jets provide a theoretical basis for predicting the transition to turbulence. The transition from laminar jet flow to turbulent flow occurs when the stationary ambient is no longer capable of viscously communicating with the jet. The viscous communication time between the jet-ambient interface and the jet centerline follows from Stokes' first problem [14]

$$t_v = \frac{D^2}{16\nu} . \quad (12)$$

The jet is free to buckle, i.e., to get out of hand, if the viscous diffusion time  $t_v$  is longer than the buckling and breakup time  $t_B$ . Defining the buckling number  $N_B$  as the ratio of these two characteristic times of the flow configuration,

$$N_B = \frac{t_v}{t_B} > 1 , \quad (13)$$

we have a criterion which predicts the fluctuating (turbulent) behavior of the jet. Using equation (12) and  $t_B = \lambda/V$ , the buckling number can be written also as

$$N_B = \frac{VD}{\nu} \frac{D/\lambda}{16} \quad (14)$$

For a round jet, the transition criterion  $N_B > 1$  becomes

$$\frac{VD}{\nu} > 25 \quad (15)$$

It should be noted that this order-of-magnitude estimate of the transition Reynolds number agrees very well with experimental observations. For example, Viilu [15] found the value of 11.2 for the Reynolds number of breakdown of the

steady laminar jet. Viilu's observations were later confirmed by Reynolds [2] who reported the range  $10 < Re < 30$  for the transition Reynolds number.

The buckling number criterion of transition to turbulence, equation (13), explains also why the observed transition  $Re$  is a number considerably greater than unity. For a dimensionless group to truly delineate the transition from one mechanism to another, it must have a value of order one which, after all, reflects the balance between the competing mechanisms. The Reynolds number is not the correct dimensionless group to describe transition to turbulence. The Reynolds number is the experimental (measurable) reflection of the  $N_B$  transition criterion.

#### Concluding Remarks

This letter unveiled a theoretical basis for predicting the large scale structure and fluctuating behavior of inviscid jets. The analogy between jet envelopes and elastic columns in axial compression showed that the natural tendency of inviscid jets is to buckle over a precise wavelength which scales only with the jet diameter. The repeated buckling and breakup of the jet column is responsible for the sinusoidal, river-like, path of turbulent jets and also for their natural whiplash motion. The predicted natural frequency of the jet agrees very well with measurements from harmonic excitation experiments. Finally, we learned that the transition from laminar to turbulent jet flow occurs when the buckling and breakup time is shorter than the time of viscous diffusion across the jet. This last conclusion is supported strongly by experimental observations.

The buckling property described in this letter emerges as the fundamental property serving as origin for turbulent motion in inviscid flows.

Acknowledgement. This research is being supported by the Office of Naval Research.

#### References

1. S.C. Crow and F.H. Champagne, J. Fluid Mech., **48**, 547 (1971).
2. A.J. Reynolds, J. Fluid Mech., **14**, 552 (1962).
3. C.S. Yih, Fluid Mechanics, McGraw-Hill, New York (1969), 546.
4. A. Bejan, Buckling and Vibration Theory of Jets, Report CUMER 80-4, Department of Mechanical Engineering, University of Colorado, Boulder, 1980.



5. A.E.H. Love, The Mathematical Theory of Elasticity, 4th edition, Cambridge University Press (1927), 3.
6. J.P. Den Hartog, Strength of Materials, McGraw-Hill, New York (1949), 184.
7. W.C. Reynolds and H.C. Perkins, Engineering Thermodynamics, 2nd edition, McGraw-Hill, New York (1977), 348.
8. L. Prandtl, Essentials of Fluid Dynamics, Blackie & Son, London (1969), 40.
9. L. Prandtl, Op. cit., 47.
10. J.P. Den Hartog, Op. cit., 185.
11. L. Prandtl, Op. cit., 51.
12. D. Bechert and E. Pfizenmaier, J. Sound Vib., **43**, 581 (1975).
13. E. Acton, J. Fluid Mech., **98**, 1 (1980).
14. H. Schlichting, Boundary Layer Theory, 4th edition, McGraw-Hill, New York (1960), 72.
15. A. Viilu, Preliminary Report of the M.I.T. Department of Aeronautics and Astronautics for NASA, Grant No. NSG-31-60, 1960.

## Comments on "Viscous buckling of thin fluid layers"

Adrian Bejan

Department of Mechanical Engineering, University of Colorado, Boulder, Colorado 80309

(Received 23 February 1981; accepted 26 June 1981)

Suleiman and Munson<sup>1</sup> recently presented a sequence of interesting experiments concerning the buckling of thin viscous fluid layers. In their paper the authors referred to Taylor's observations on the buckling of slender viscous filaments.<sup>2</sup> His early observations and the Suleiman and Munson experiments point toward an important analogy between the buckling of elastic columns and the buckling of viscous filaments in longitudinal compression.

The object of this Comment is two-fold. First, it brings to the readers' attention the fact that a buckling theory of thin viscous layers already exists. Second, it points out that the buckling of slender columns in axial compression is not a property only of elastic solids and highly viscous fluids, but also a property of *invisible* columns (streams).

The buckling of a thin viscous layer was considered theoretically by Buckmaster, Nachman, and Ting.<sup>3</sup> They showed that viscous layers in longitudinal compression satisfy two basic requirements: (i) the viscous layer is in axial compression and the compressive force is proportional to the relative velocity between the two ends of the layer; (ii) if curved, the viscous layer develops in its cross section a bending moment which is proportional to the time-rate of change in the local curvature. The momentum equations integrated over the viscous layer led Buckmaster, *et al.*<sup>3</sup> to a global equation for the evolution of the layer centerline. This equation was solved by assuming various initial disturbances as the starting shape in the evolution of the viscous layer. In a subsequent paper, Buckmaster and Nachman<sup>4</sup> have extended this theory to the case where surface tension effects play an important role.

Of fundamental interest are the similarities between the buckling of a viscous layer (the *viscida* problem) and the buckling of a slender elastic column (the *elastica* problem). A close examination of the Euler theory for slender elastic columns reveals that, for infinitesimal buckling, elastic columns must satisfy only two conditions (Ref. 5, p. 184): (iii) the column is straight and in axial compression; (iv) if subjected to a separate bending test, the column develops a resistive bending moment in its cross section which is proportional to the local curvature. The infinitesimal buckling of the straight column follows from invoking static equilibrium for the system sketched in Fig. 1. For a straight or nearly straight column there are two equilibrium conditions to consider. The first is the obvious balance of compressive forces  $C$  in the longitudinal direction. The second is one of rotational equilibrium which states that the eccentricity bending moment  $Cy$ , however small, must be balanced at all times by the cross-sectional bending moment  $M$ . In the case of a column containing elastic material, a special bending test of prescribed curvature (Ref. 5, p. 37) combined with knowledge of the elastic properties of individual fibers in the slender column leads to the notion of a cross-sectional bending moment proportional to the local curvature (iv). Combining this notion with the rotational equilibrium condition yields the equilibrium shape of the straight column, namely, a sinusoid of infinitely small amplitude. The infinitesimal amplitude is indeterminate, hence, the equilibrium of the nearly straight elastic column is indifferent. If present, the slightest lateral force is able to push the column away from the straight equilibrium shape into a nearly straight (sinusoidal) equilibrium shape (Ref. 5, p. 184).

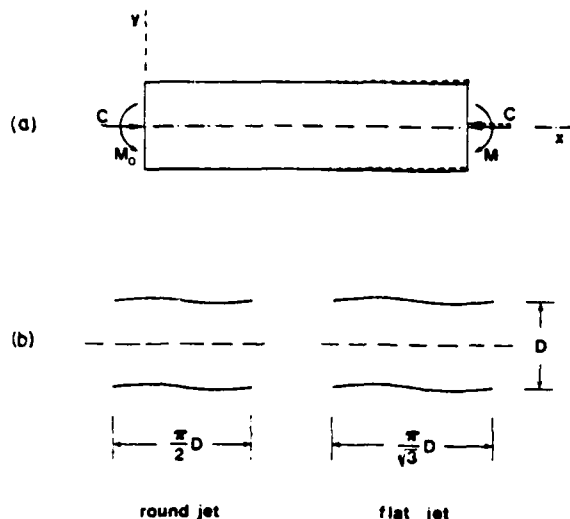


FIG. 1. (a) Translational and rotational equilibrium of a slender column (control volume) in axial compression. (b) The natural buckling wavelength of circular and two-dimensional inviscid jets.

In this discussion it is important to include the case of inviscid fluid columns: Do such columns conform to buckling of type (i, ii) or to buckling of type (iii, iv)? Thermodynamic reasoning alone suggests that inviscid columns should buckle according to model (iii, iv) because, like elastic solids and unlike highly viscous fluids, inviscid fluids are free of entropy generation.<sup>6</sup>

Referring again to Fig. 1, we note that a column containing inviscid fluid is none other than the imaginary control surface drawn around an inviscid jet flowing through an inviscid fluid at rest. Since the column is stationary, its equilibrium is described by the two static conditions (force and moment) discussed in connection with the Euler buckling of elastic columns. The remaining problem is to determine what special forms  $C$  and  $M$  take in the case of inviscid stream columns. For the compressive force on the control volume,  $C$ , we know from the thermodynamics of open flow systems that<sup>7</sup>

$$C = \rho A V^2, \quad (1)$$

where  $\rho$ ,  $A$ ,  $V$  are the density, cross-sectional area, and velocity of the stream. In order to determine the cross-sectional bending moment  $M$ , we conduct a special bending experiment where the inviscid stream is held in a duct of known radius of curvature,  $R_\infty$ . In the limit of vanishingly small curvature, the inviscid flow equations show that the resistive bending moment in the cross section is<sup>8</sup>

$$M = \rho V^2 I / R_\infty, \quad (2)$$

where  $I$  is the area moment of inertia of the cross section (Ref. 5, p. 37). Equations (1) and (2) show that inviscid fluid columns obey conditions (iii, iv) for in-

finitesimal buckling. The corresponding equilibrium shape of the column is a sinusoid of infinitely small amplitude,<sup>8</sup> whose wavelength is

$$\lambda = 2\pi(I/A)^{1/2}. \quad (3)$$

Inviscid streams, like elastic rods and viscous layers, possess the natural property of buckling. The wavelength of the buckled shape scales only with the transverse dimension of stream; for example, Eq. (3) for a jet of round cross section, yields  $\lambda/D = \pi/2$ . Unlike buckled elastic columns, whose equilibrium is indifferent (Ref. 5, p. 184), buckled inviscid columns are unstable. The post-buckling evolution of the inviscid column is well understood, forming the subject of the classical theory of hydrodynamic stability.<sup>9</sup> However, the buckling property is to be recognized as responsible for the wave-like "disturbance" assumed routinely (*empirically*) as a starting point in any hydrodynamic stability analysis.

In essence, the buckling property of inviscid streams guarantees that such streams cannot flow straight through another fluid or through a flexible duct. This new property of inviscid fluids stands at the very root of the phenomenon of *turbulence*. For example, the interaction between the elbows of the buckled stream and the stagnant medium leads to the periodic formation of large eddies. These large-scale turbulent structures are responsible for the river-like shape of turbulent jets, wakes, and plumes: It is widely observed that the wavelength of this large-scale meandering path scales with the diameter of the stream, as predicted in Eq. (3). The natural buckling of inviscid streams is particularly visible in the case of streams flowing within flexible boundaries, like rivers and capillary rivulets at high Reynolds numbers. The buckling property serves as the theoretical basis for predicting other turbulence parameters, for example, the natural frequency of turbulent jets (the Strouhal number) and the critical Reynolds number for transition to turbulence.<sup>8</sup>

<sup>1</sup>S. M. Suleiman and B. R. Munson, *Phys. Fluids* 24, 1 (1981).

<sup>2</sup>G. I. Taylor, in *Proceedings of the 12th Congress of Applied Mechanics*, Stanford, 1968 (Springer-Verlag, Berlin, 1969), p. 382.

<sup>3</sup>J. D. Buckmaster, A. Nachman, and L. Ting, *J. Fluid Mech.* 69, 1 (1975).

<sup>4</sup>J. D. Buckmaster and A. Nachman, *Q. J. Mech. Appl. Math.* 31, 157 (1978).

<sup>5</sup>J. P. Den Hartog, *Strength of Materials* (McGraw-Hill, New York, 1949), p. 184.

<sup>6</sup>A. Bejan, *J. Heat Transfer* 101, 718 (1979).

<sup>7</sup>A. H. Shapiro, *The Dynamics and Thermodynamics of Compressible Fluid Flow* (Ronald, New York, 1953), Vol. 1, p. 225.

<sup>8</sup>A. Bejan, *Letters in Heat and Mass Transfer* 8, 187 (1981).

<sup>9</sup>L. Prandtl, *Essentials of Fluid Dynamics* (Blackie and Son, London, 1969), p. 51.

# The meandering fall of paper ribbons

Adrian Bejan

Department of Mechanical Engineering, University of Colorado, Boulder, Colorado 80309  
(Received 14 August 1981; accepted 22 February 1982)

This paper discusses experimental observations of the meandering fall of light-weight tissue paper ribbons. The photographs show that the ribbons assume a sinusoidal shape with a unique wavelength which scales with the thickness of the airstream entrained by the ribbon.

The objective of this paper is to present a series of interesting experimental observations concerning the meandering motion executed by highly flexible ribbons falling through the air. The experiment consisted of dropping a length of light-weight toilet tissue paper through the air and photographing its shape as it falls to the ground. The reader may take note of the fact that this falling-ribbon phenomenon occurs naturally when excited sports fans launch rolls of tissue paper from the stands onto the playing field. Another natural phenomenon related to the falling-ribbon experiments described in this paper is the "waving of flags"<sup>1</sup> and the "vibration" of tape drives used in the computer technology.<sup>2</sup> The classical perspective in the study of flag waving falls in the realm of hydrodynamic stability theory, where one questions the stability of the flexible solid surface. The starting point in the stability study is the assumption of an initial deformation of *arbitrary* wavelength.

In the present experiments, ribbons of various lengths were dropped from heights in the range 3–7 m, through the quiescent air of the laboratory. The time of free fall was measured with a digital stopwatch; it was found that the ribbon reached its terminal velocity very quickly, therefore, the free-fall velocity  $U$  could be determined by dividing the total travel by the measured time of free-fall. In order to force the ribbon to fall "head first," one end was loaded with a lead refill for a mechanical pencil.

This simple experiment was repeated many times and, in all cases, the photographs showed that the falling ribbon acquires a sinuous shape: the wavelength of this shape was the same for all the cases involving a ribbon of fixed length. Figures 1(a) and 1(b) show very clearly the characteristic sinuous shape observed in these experiments. A longer ribbon [Fig. 1(b)] exhibits a relatively longer wavelength.

Another important observation is the fact that the sinuous shape travels as a solid body downward, at a speed of order  $U/2$ , where  $U$  is the speed of the tissue paper itself. The wave speed was measured photographically, as shown in Fig. 2. This photograph was obtained with the shutter open in complete darkness, while lighting the falling ribbon with a strobe light three times, at precise time intervals ( $t = 0.025$  sec). The fact that the sinuous shape travels at half-speed is strong evidence that the sinuous shape is produced not by the tissue paper, but by the airstream whose centerline moves at top speed  $U$  through an ambient at rest.

The key measurement facilitated by the falling-ribbon experiment is that of the meander wavelength. Measuring the distance between the elbows of the sinuous shape of Figs. 1(a) and 1(b), and averaging these measurements over the sinuous portions of each ribbon, yields the wavelengths listed under  $\lambda_0$  in Table I. The relatively small standard deviations of these measurements indicate that the elbow-to-elbow distance does not vary appreciably along the wavy portion of the ribbon.

The effective thickness  $D_e$  of the air stream entrained by the ribbon can be calculated based on the following energy-conservation argument. During its steady fall at terminal velocity  $U$ , the ribbon weight  $W$  performs the mechanical work  $W\Delta L$  on its ambient;  $\Delta L$  is the linear increment in downward travel, equal to  $U\Delta t$ , where  $\Delta t$

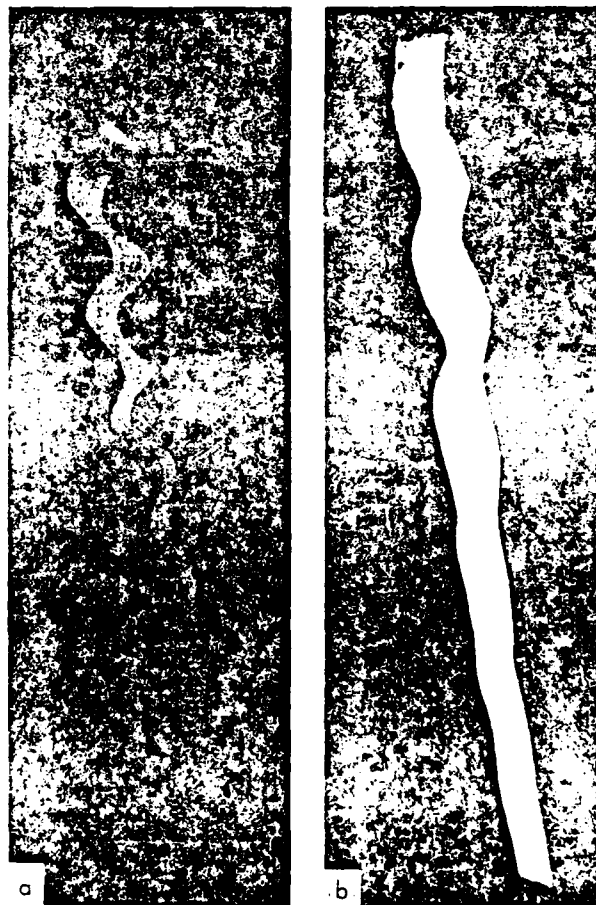


FIG. 1. (a) Fall of a 1.25 m ribbon of tissue paper. (b) Fall of a 1.83 m ribbon of tissue paper.

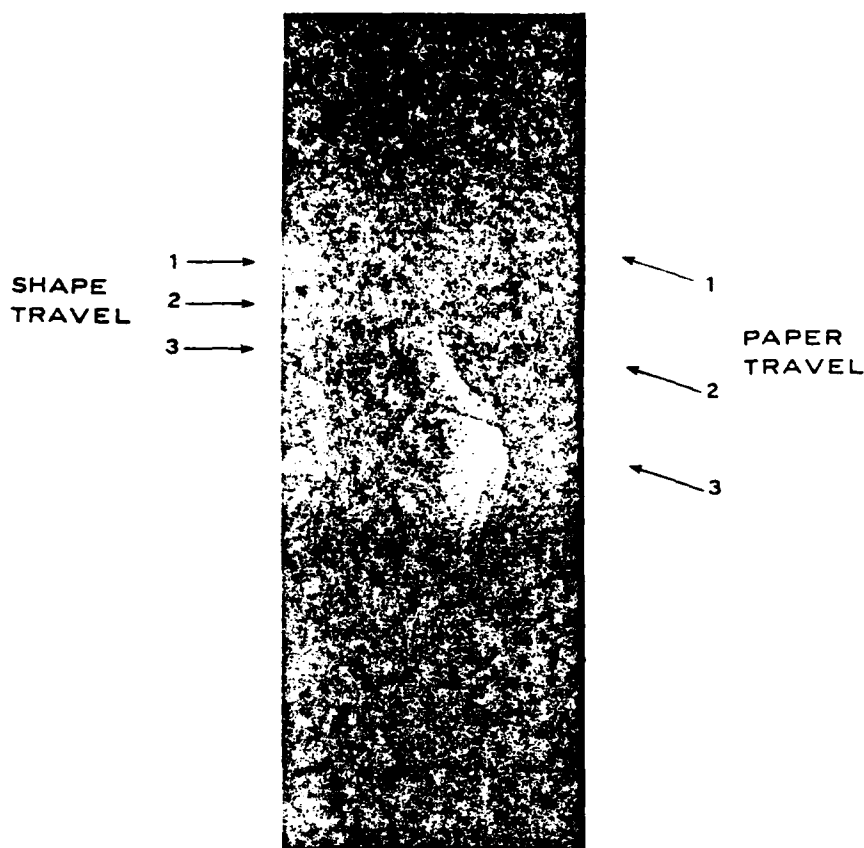


FIG. 2. Superposition of three images during the fall of the 1.25 m ribbon, showing that the sinuous shape falls half as fast as the ribbon material.

TABLE I. Laboratory measurements of the meandering wavelength of the inviscid air stream driven by a falling ribbon.

Experiment	Ribbon dimensions length $\times$ width $L \times b$ (cm <sup>2</sup> )	Total weight $W$ (g)	Terminal speed $U$ (m/s)	Meander wavelength $\lambda_B$ (cm)	Effective air-stream thickness $D_e$ (cm)
Fig. 1(a)	125 $\times$ 11.4	3.21	2.93 $\pm$ 0.15	15.5 $\pm$ 1.3	5.5 $\pm$ 0.56
Fig. 1(b)	183 $\times$ 11.4	4.97	3.04 $\pm$ 0.09	28 $\pm$ 1.5	7.86 $\pm$ 0.46

is the time increment. The work done by the weight is first converted into the kinetic energy imparted to the airpacket pierced by the tip of the ribbon during the time  $\Delta t$  (at the same time, the ribbon-air train sheds a moving air packet of the same size: the kinetic energy of this air packet is eventually dissipated in the wake). Equating the two energy increments, we write

$$W\Delta L = (\rho D_e \Delta L b)(U^2/2) \text{ or } D_e = 2(W/\rho U^2 b), \quad (1)$$

where  $b$  is the ribbon width and  $\rho$  is the air density. The results of this calculation are listed in Table I. Clearly, the meander wavelength scales with the air stream thickness.

A possible explanation for the above observations may be offered based on the buckling theory of inviscid streams.<sup>3,4</sup> One key result of this theory is the universal proportionality which must exist between stream

thickness ( $D$ ) and "buckling" wavelength ( $\lambda_B$ ). For a two-dimensional stream one finds  $D = (\sqrt{3}/\pi)\lambda_B$ , which agrees in an order of magnitude sense with the measurements listed in Table I. Additional evidence supporting this explanation is the fact that, from Fig. 1(a) to 1(b), both  $\lambda_B$  and  $D_e$  increase.

#### ACKNOWLEDGMENT

This research work was supported by the Office of Naval Research.

<sup>3</sup>H. Lamb, *Hydrodynamics* (Dover, New York, 1945), p. 374.  
<sup>4</sup>S. K. Datta and W. G. Gottenberg, *J. Appl. Mech.*, **97**, 195 (1975).

<sup>5</sup>A. Bejan, *Lett. Heat Mass Transfer*, **8**, 187 (1981).

<sup>6</sup>A. Bejan, *Phys. Fluids*, **24**, 1764 (1981).

THEORETICAL EXPLANATION FOR THE INCIPIENT FORMATION OF MEANDERS IN STRAIGHT RIVERS

Adrian Bejan

Reprinted from

**Geophysical  
Research  
Letters**

Volume 9, Number 8, August 1982

THEORETICAL EXPLANATION FOR THE INCIPIENT FORMATION OF MEANDERS IN STRAIGHT RIVERS

Adrian Bejan

Department of Mechanical Engineering, Campus Box 427, University of Colorado  
Boulder, Colorado 80309 USA

**Abstract.** This paper advances a theoretical explanation for the lateral periodicity and geometric similarity of meanders observed in rivers of many sizes. Invoking the static equilibrium of a straight river bed, it is shown analytically that the equilibrium shape of the bed is a unique sinusoid. The theoretical wavelength of the sinusoidal shape is proportional to the width of the river, in agreement with visual observations of rivers of all sizes.

1. The Geometric Similarity of River Meanders

The most basic feature of the meander phenomenon is the proportionality between meander wavelength  $\lambda$  and stream width  $W$  (Leopold and Wolman 1960). As concluded in a recent review article (Callander 1978), significant theoretical progress has been made in the direction of explaining the occurrence of meanders and accounting for measured meander parameters. The theories developed over the past thirty years have in common the thinking framework offered by the Theory of Hydrodynamic Stability: according to this approach, one analyzes the stability or instability of sinusoidal waves (disturbances) superimposed on the straight river flow. As summarized by Parker (1976), consideration of gravity waves led Werner (1951) to the conclusion that  $\lambda/W = 2F$ , where  $F$  is the flow Froude number. Hansen (1967) posed the linearized stability problem associated with a meandering (sinusoidal) disturbance and found  $\lambda/H = 7 F^2/S$ , where  $H$  is the river depth and  $S$  is the dip angle of the river bed. Anderson (1967) analyzed transverse oscillations and obtained  $\lambda/W = \text{constant} \times (F H/W)^{1/2}$ . A number of improved models of hydrodynamic stability have been reported more recently: for example, Callander (1969), Sukegawa (1970), Hayashi (1974), Englund and Skovgaard (1973) and Parker (1976).

The chief contribution of the theoretical research reviewed above and, in greater detail, in Callander (1978), is to have shown that the bed of a channel with straight banks is unstable: since the bed is composed of moving sediment, the amplitude of a certain class of disturbances is likely to grow the fastest. In addition, this research predicted correctly the direction of migration and the downstream wave speed of meanders. These conclusions are important and will be adopted without debate in the theory developed in this paper. However, the chief limitation of the existing theories is also important: note should be made of the fact that the ratio  $\lambda/W$  predicted by hydrodynamic stability considerations (Table 1) does not have

a characteristic (unique) range of values, contrary to the statistical evidence compiled over natural streams of widely varying sizes (Leopold and Wolman 1960). This limitation is accepted from the start by every stability analyst who postulates the existence of disturbances of every wavelength and then tries to identify which of these disturbances will develop the most rapidly.

Inasmuch as the constancy of the ratio  $\lambda/W$  appears to be an intrinsic property of all streams, the stability theories explain the evolution (behavior) of existing meanders but not their origin.

The theory constructed in this paper addresses the question which has not yet been addressed, namely, why does a straight (undisturbed) river choose a sinuous shape of precise wavelength? Before presenting the theoretical answer to this fundamental question, the author finds it necessary to review a class of very useful experiments which shed light on the natural properties of the (river)-(flexible bed) system.

2. The Stream Plate Experiments

The original stream plate experiment was proposed by Tanner (1960) as a means of visualizing the natural tendency of streams to meander. The same technique was used in a comprehensive study by Gorycki (1973a). The experiment consists of a smooth plane surface which supports a water jet flow issuing from a nozzle tangent to the surface. Thus, the stream plate experiment is the laboratory version of water tricklings commonly observed on shower walls and car windshields. The water columns generated in this fashion meander in much the same way as rivers do. However, there is one important advantage to this experiment, namely, the opportunity to observe the incipient phase of the meandering process in a straight jet.

Of interest here are Tanner's and Gorycki's observations, and the clever mechanical analog visualized by Gorycki to simulate river meandering. First, the stream plate visualization of the meander formation process is strong evidence that the meander is a property of the stream; this property is independent of the effects of sediment. In comparing various stream plate experiments, Gorycki (1973b) argues further that plate roughness is not necessary for meander formation.

The experiments also showed (Tanner 1962) that meandering is independent of the secondary flow or disturbances which may be present in the nozzle. This conclusion is strengthened by the statement made by Schumm and Khan (1972) who observed meanders made in the laboratory under straight entrance conditions: "...a perturbation or disturbance of the flow may not be an essential cause of meandering" (Gorycki 1973a, p. 178).

Gorycki presented also a mechanical analog of the river meandering mechanism: he held a slender

Copyright 1982 by the American Geophysical Union.

Paper number 2L1032.  
0094-8276/82/002L-1032\$3.00

TABLE 1. Comparison of the Present Theory with Meander Wavelength Observations

	Reference	$\lambda/W$	Remarks
time, or direction of meander amplitude growth ↓	present theory	2.22	incipient buckling (absolutely straight stream)
	Gorycki (1973a)	2-3	stream plate simulations
	Leopold, Wolman and Miller (1964), Leopold and Wolman (1970), Dury (1964)	2-3	field studies in straight rivers
	Schumm and Khan (1972) Table 3	$3.24 \pm 0.64$	laboratory channel during development
	Keller (1972)	3-5	channel experiments during development
		5-7	during late stages of development
	Leopold and Wolman (1960) Table 1	6.5 - 11	natural (long history)

piece of elastic (a slender cylindrical column of rubber) between two parallel pieces of glass. He then moved the glass pieces relative to one another, in the direction parallel to the cylinder axis. As a result, the piece of elastic assumed a shape which resembles very closely that of a meandering stream in a stream plate experiment.

It is shown in the next section that the mechanism responsible for elastic meandering is also responsible for river meandering. In Mechanical Engineering, which is the present author's education, the sinusoidal shape of the elastic column has been explained as the buckling property of slender spaces in longitudinal compression. The buckling of slender columns represents an important and voluminous chapter in the centuries-old discipline of Strength of Materials (Den Hartog, 1961). The theoretical basis for this chapter was established by Euler, who pointed out that in order for a slender space to buckle into an equilibrium sinusoidal shape it must satisfy only two conditions (Love 1927):

- (i) the slender space must be in a state of axial (longitudinal) compression.
- (ii) the material which fills the space must be such that if the space is subjected to a separate bending test of prescribed curvature, then the space develops in its cross-section a resistive bending moment (couple) which is proportional to the local curvature.

The piece of elastic described by Gorycki satisfies the above conditions. But it is important to keep in mind that conditions (i) and (ii) do not refer to a specific material such as an elastic solid: they refer to a space (column) of finite size. The objective of the following analysis is to prove that the river and its bed, as a slender space, also satisfy conditions (i) and (ii) necessary for sinusoidal buckling.

### 3. The Static Equilibrium of a Straight River

Consider a straight, inviscid, river flow of uniform velocity  $V$ , density  $\rho$ , width  $W$  and depth  $H$ . The bed of the river is horizontal. In the stationary frame of reference of the bed, the river cross-section exhibits a uniform compressive stress  $\rho V_0^2 + P_0(z)$ , where  $P_0$  is the excess pressure

$$P_0(z) = \rho g (H - z) \quad (1)$$

and  $g$  is the gravitational acceleration. The resultant of this compressive stress, integrated over the river cross-section, is

$$C = \rho V_0^2 WH \left(1 + \frac{gH}{2V_0^2}\right) \quad (2)$$

Therefore, in the frame of reference of the bed, the straight river is a slender column in longitudinal compression. This means that condition (i) is satisfied. In order to see that the bed, as a duct, is in a state of longitudinal compression, the reader should think of a piece of garden hose through which the flowrate is high (turbulent). The hose is pushed axially by the reactive compressive force associated with the stream leaving through the open end. The same hose is pushed axially in the opposite direction by the impactive force associated with the stream entering it from the faucet.

As shown in Fig. 1, the static equilibrium of the bed requires two statements, one for translational equilibrium (obvious,  $C \equiv C$ ) and the other for rotational equilibrium. The rotational equilibrium condition is made necessary by the fact that no straight river is ever "mathematically" straight; in other words, all straight rivers are subjected to an infinitesimally small couple  $CY$  due to the imperfect colinearity of the axial



forces  $C$ . The rotational equilibrium condition is (Den Hartog 1961)

$$CY - M + M_0 = 0 \quad (3)$$

where  $M$  is the couple acting over the river cross-section.

It is easy to show that the river column also satisfies condition (ii), or that a net couple  $M$  is present whenever the column  $Y(X)$  is locally curved. Consider a separate bending test in which the river radius of curvature  $R$  is infinitely greater than the river width  $W$  (Fig. 2). The new velocity  $V$  and pressure distribution  $P$  in the cross-section can be determined immediately from Bernoulli's equation (Prandtl 1969)

$$\frac{1}{2} \rho V^2 + P = \frac{1}{2} \rho V_0^2 + P_0 \quad (4)$$

combined with a local force balance in the radial direction  $y$  (Prandtl 1969),

$$\frac{\rho V^2}{R_\infty} = \frac{\partial P}{\partial y} \quad (5)$$

In the limit of vanishingly small curvature,  $W/R_\infty \rightarrow 0$ , we obtain

$$V = V_0 \left( 1 - \frac{y}{R_\infty} \right) \quad (6)$$

$$P = \rho V_0^2 \frac{y}{R} + \rho g(H - z). \quad (7)$$

A related result is that the free surface  $z_f(y)$  acquires a slight tilt

$$z_f(y) = H + \frac{V_0^2 y}{g R_\infty} \quad (8)$$

Due to the slight tilt, the center of mass of the cross-section shifts from  $y = 0$  to  $y_0 = V_0^2 W^2 / (12 g H R_\infty)$ , where  $y_0 \ll W$ .

According to the standard methods of mechanical engineering, the net bending moment  $M$  about the vertical line passing through the center of mass of the cross-section is

$$M = \int_{y=-W/2}^{y=W/2} \int_{z=0}^{z=z_f(y)} (\rho V^2 + P)(y - y_0) dz dy = - \frac{\rho V_0^2 H W^3}{8 R_\infty} \quad (9)$$

This result demonstrates that the river cross-section experiences a bending moment as soon as the river trajectory has curvature. Equation (9)



Fig. 1. Static equilibrium of a straight river bed (view from above).

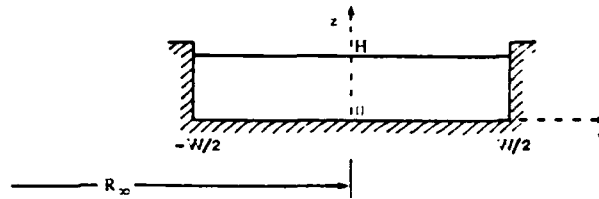


Fig. 2. Cross-section through the river.

proves that rivers also obey condition (ii) for sinusoidal buckling.

#### 4. The Natural Sinusoidal Shape of Rivers

In the limit of infinitesimally small deviations from the rectilinear shape, the river curvature  $1/R_\infty$  is equal to  $-d^2Y/dX^2$ . Based on this approximation and equation (9), the static equilibrium condition (3) becomes

$$CY + \frac{1}{8} \rho V_0^2 H W^3 Y'' + M_0 = 0 \quad (10)$$

The general equilibrium shape of the river bed follows from equation (10),

$$Y(X) = \frac{M_0}{C} [\cos(2\pi \frac{X}{\lambda}) - 1], \quad (11)$$

where the wavelength  $\lambda$  has a precise value given by

$$\frac{\lambda}{W} = \frac{\pi}{[2 + gH/V_0^2]^{1/2}} \quad (12)$$

For shallow rivers and for stream plate simulations ( $gH/V_0^2 \ll 1$ ) we find

$$\frac{\lambda}{W} = \frac{\pi}{\sqrt{2}} = 2.22, \text{ universal constant} \quad (13)$$

In conclusion, the natural (equilibrium) shape of the river bed is a sinusoid whose wavelength is a precise multiple of the river width. The amplitude of this shape is unknown (infinitely small), because the analysis leading to equation (12) invoked the static equilibrium of a straight river. It is well known, however, that the equilibrium of a nearly straight river bed is unstable (cf. Hydrodynamic Stability Theory, Section 1) and that the highly regular, sinuous, shape determined here is destined to grow in amplitude.

#### 5. Conclusion

The fundamental contribution of this theoretical argument is the prediction of a universal proportionality between meander wavelength and river width, equations (12, 13). This prediction is supported strongly by observations of meander formation in straight rivers and in stream plate experiments. Attention is drawn first to the stream plate experiments (Gorycki

1973a, p. 179, Figs. 3, 8, 9, 10, 13) which conclusively show "that the spacing between the sinuous curves or point bars in straight streams is approximately two to three times the stream width", as in equation (13). Similar values of  $\lambda/W$  in straight rivers were reported by numerous field studies; for example, in Leopold, Wolman and Miller (1964), Leopold and Wolman (1970, Fig. 7.8) and Dury (1964, Figs. 26, 28). A ratio  $\lambda/W$  between 2 and 3 appears to be a universal feature of all straight streams. Keller (1972, p. 1534) showed that only in the late stages of meander development  $\lambda/W$  reaches values in the range of 5-7, whereas during development the ratio  $\lambda/W$  is in the range 3-5.

Table 1 shows a summary of experimental observations next to the constant ratio  $\lambda/W$  predicted by the present theory of river buckling. The present theory agrees with observations made in straight or nearly straight rivers, which conform to the type of system selected here for analysis in Section 2. Table 1 shows also that, as time passes, the ratio  $\lambda/W$  increases from the initial theoretical value (2.22) to the natural (long-history) value of approximately 10. Thus, the present theory offers a concise explanation for the origin of meanders in straight rivers.

**Acknowledgement.** This research was supported by the U.S. Office of Naval Research.

#### References

- Anderson, A. G., On the development of stream meanders, Proc. 12th Cong. IAHR, Fort Collins, Colorado, Vol. 1, 370-378 (1967).
- Callander, R. A., Instability and river channels, J. Fluid Mech., 36, 465-480 (1969).
- Callander, R. A., River meandering, Ann. Rev. Fluid Mech., 10, 129-158 (1978).
- Den Hartog, J. P., Strength of Materials, Dover, New York (1961), Chapter IX.
- Dury, G. H., Principles of underfit streams, U.S. Geol. Survey Prof. Paper 452-A (1964).
- Keller, E. A., Development of alluvial stream channels: a five-stage model, Geol. Soc. America Bull., 83, 1531-1536 (1972).
- Engelund, F. and Skovgaard, O., On the origin of meandering and braiding in alluvial streams, J. Fluid Mech., 57, 289-302 (1973).
- Gorycki, M. A., Hydraulic drag: a meander initiating mechanism, Geol. Soc. America Bull., 84, no. 1, 175-186 (1973).
- Gorycki, M. A., Hydraulic drag: a meander initiating mechanism: Reply, Geol. Soc. America Bull., 84, no. 9, 3119-3122 (1973b).
- Hansen, E., The formation of meanders as a stability problem, Hydraul. Lab., Tech. Univ. Denmark, Basic Res. Prog. Rep. no. 13 (1967).
- Hayashi, T., The formation of meanders in rivers, Proc. Japan Soc. Civil Engrs., no. 180 (1970).
- Leopold, L. B., and Wolman, M. G., River meanders, Bull. Geological Soc. America, 71, 769-794 (1960).
- Leopold, L. B., and Wolman, M. G., River channel patterns, in Dury, G. H., ed., Rivers and River Terraces, Praeger Publishers, New York (1970).
- Leopold, L. B., Wolman, M. G. and Miller, J. P., Fluvial Processes in Geomorphology, W. H. Freeman, San Francisco (1964).
- Love, A. E. H., The mathematical theory of elasticity, 4th ed., Cambridge University Press, Cambridge (1927), p. 3.
- Parker, G., On the cause and characteristic scales of meandering and braiding in rivers, J. Fluid Mech., 76, 457-480 (1976).
- Prandtl, L., Essentials of Fluid Dynamics, Blackie & Son, London, Chapter II, (1969).
- Schumm, S. A., and Khan, H. R., Experimental study of channel patterns, Geol. Soc. America Bull., 83, 1755-1770 (1972).
- Sukegawa, N., Conditions for the occurrence of river meanders, J. Faculty Eng., Univ. Tokyo, 30, 289-306 (1970).
- Tanner, W. F., Helical flow, a possible cause of meandering, J. Geophys. Res., 65, 993-995 (1960).
- Tanner, W. F., Inexpensive models for studying helical flow in streams, J. Geol. Education, 10, no. 4, 116-118 (1962).
- Werner, P. W., On the origin of river meanders, Trans. Am. Geophys. Un., 32, 898-902 (1951).

(Received October 13, 1981;  
revised December 9, 1981;  
accepted June 15, 1982.)

# The nonaxisymmetric (buckling) flow regime of fast capillary jets

Michael G. Stockman and Adrian Bejan

Department of Mechanical Engineering, University of Colorado, Boulder, Colorado 80309

(Received 16 December 1981; accepted 5 May 1982)

This paper reports an experimental study of the nonaxisymmetric flow of a fast liquid jet discharging into the atmosphere. The nonaxisymmetric shape of the jet was photographed and subjected to a wavelength analysis. The results of the wavelength analysis demonstrate that the jet shape is governed by a narrow band of wavelengths associated with a characteristic value  $\lambda_{max}$  which scales with the jet diameter  $D$ . It is shown that the experimental observations are in agreement with predictions based on hydrodynamic stability theory and buckling theory.

## I. INTRODUCTION

The problem of capillary jet flow and breakup has a long history beginning with the qualitative studies of Bidone<sup>1</sup> and Savart,<sup>2</sup> which were extended by Savart, Plateau, and Rayleigh, and summarized later by Rayleigh.<sup>3</sup> These studies focused on the low-speed regime where the jet forms radially symmetric, regularly shaped, drops of measurable frequency. Rayleigh studied the symmetric (varicose) breakup theoretically, by imposing hypothetical infinitesimal disturbances on the jet and examining the stability (or instability) of each disturbance in time. Rayleigh's theory was summarized and extended in several directions by Chandrasekhar.<sup>4</sup>

Much of the post-Rayleigh work focused almost exclusively on the axisymmetric (varicose) regime, although there have been a number of instances in which a nonaxisymmetric breakup mode was observed. Crane, Birch, and McCormick<sup>5</sup> employed an electronically driven vibrator to study the dispersion curve of low-speed jets (the dispersion curve is the graphical representation of the response of the capillary jet to a continuous set of imposed disturbance frequencies). Their results agreed only qualitatively with Rayleigh's. A similar experiment was described by Donnelly and Glaberson,<sup>6</sup> who studied the response of a capillary jet to external disturbances generated by a loudspeaker and audio oscillator. Donnelly and Glaberson, like Crane *et al.*, noted parcels of liquid between the large drops predicted by Rayleigh's theory. They termed these parcels "ligaments" and accounted for their appearance by arguing that the ligaments were due to higher-order harmonics present in the disturbing frequency. Donnelly and Glaberson found excellent agreement between Rayleigh's linearized theory and their experimental results, despite the fact that Rayleigh's theory does not predict the existence of ligaments.

During the past fifteen years we have witnessed a large volume of research aimed at explaining and predicting the formation of ligaments in the process of varicose break-up; examples of this research effort are the theoretical work of Yuen,<sup>7</sup> Nayfeh,<sup>8</sup> and Lafrance,<sup>9</sup> Experimentally, the ligament and satellite drop formation mechanism was investigated by Goedde and Yuen,<sup>10</sup> Rutland and Jameson<sup>11</sup> and, in a comprehensive three-paper study, by Chaudhary and Redekopp,<sup>12</sup> and Chaudhary and Maxworthy.<sup>13,14</sup>

Relative to the wealth of information on the varicose

regime, the nonaxisymmetric breakup is practically unknown. Photographs of the meandering path of fast capillary jets appeared as early as 1931 in the writings of Weber<sup>15</sup> and Haenlein<sup>16</sup>; these photographs were reproduced later in a famous textbook by Prandtl,<sup>17</sup> who referred to the crests of nonaxisymmetric shape as "wavy bulges." The subject of nonaxisymmetric breakup resurfaced only recently in the literature, triggered by the need for improved fire-fighting equipment. Hoyt, Taylor, and Runge<sup>18</sup> reported an experimental study of the breakup of fast water jets and on the effect of adding drag-reducing polymer to the water solution. The authors refer to the meandering section of the jet as an "unstable wave region." Greater photographic resolution of the meandering breakup regime was achieved in a subsequent descriptive study by Hoyt and Taylor.<sup>19</sup>

In summary, much of the existing work on the breakup of capillary jets has dealt with the axisymmetric (varicose) regime. The work on the nonaxisymmetric regime is sketchy and, in all cases, qualitative. The object of this paper is to report a quantitative study of the nonaxisymmetric flow regime of fast capillary jets. For the first time, the photographed shape of such jets is subjected to a rigorous wavelength analysis which shows conclusively that the nonaxisymmetric shape is governed by a characteristic, meander-type, wavelength which scales with the jet diameter.

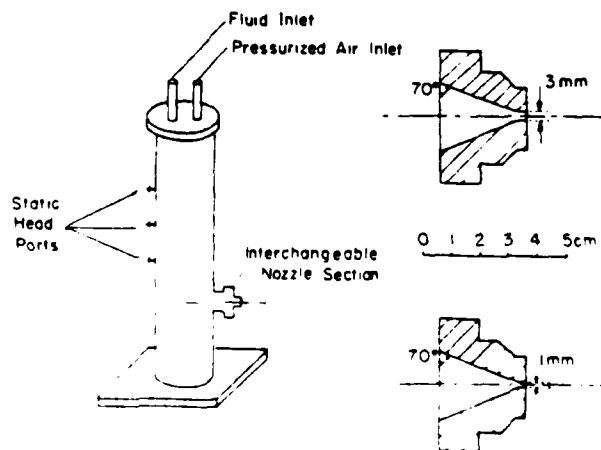


FIG. 1 Schematic of experimental apparatus and nozzle design.

## II. EXPERIMENT

The breakup modes of a capillary jet issuing into the surrounding atmosphere were studied in the laboratory using the apparatus shown in Fig. 1. The fluid reservoir consisted of a 1.83 m tall Plexiglas cylinder with an internal diameter of 14 cm. The reservoir had a number of fluid drainage ports distributed equidistantly over its height. The nozzle adaptor included a "rounded" internal duct design, and was located 15 cm from the bottom of the cylinder in order to avoid the flow distortion caused by the bottom. The reservoir was safely pressurized to 2 atm (30 psig) while the cylinder was full, yielding a jet velocity range of 0–25 m/sec. The range of low jet velocities was produced without pressurization by controlling the height of the reservoir column via an appropriate drainage port. Figure 1 shows also the two nozzles employed in this study. The 3 mm nozzle was made from a plastic compound which was cast in a precision-made mold and later machined to final dimensions. The 1.1 mm nozzle was machined directly from a Plexiglas rod.

The jet flow was recorded photographically using the set up shown schematically in Fig. 2. The photographic equipment consisted of a Hasselblad 500EL/M view camera fitted with extension tube No. 21 for detailed closeup shots, a Sunpak model 320 photoflash and a 45 cm × 75 cm section of translucent glass for diffusing the light from the flash. As shown in Fig. 2, the jet was positioned *between* light source and camera. The proper combinations of f-stop and shutter speed (in total darkness at "full" flash power), determined after a number of trials, are reported here in Table I.

To provide a reasonable range of fluid properties, this study was based on three different fluids;

I. distilled water,

II. glycerol in water solution, 30% by volume,

III. glycerol in water solution, 70% by volume.

The physical properties of the three fluids are reported in Table II. For each of the three fluids and the two nozzles, four different jet velocities ranging from 2 m/sec to 20 m/sec were observed. Thus, a total of 24 jets were observed and recorded.

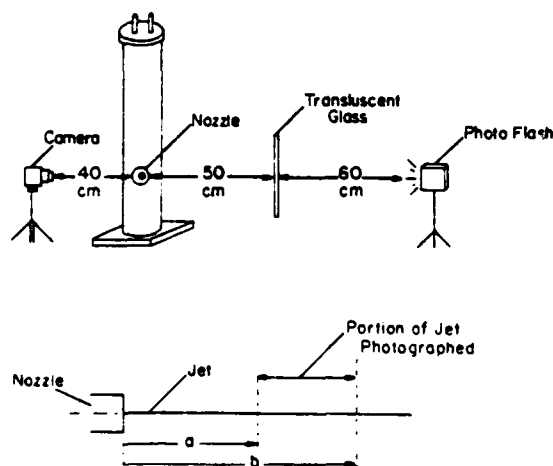


FIG. 2. Photographic arrangement, and the coordinates of the photographed jet segment.

TABLE I. Proper exposure settings for photography in total darkness at "full" flash power.

Film type	f-stop	Shutter speed
Kodak EPR 120	4	1/30 sec
Kodak PXP 120	5.6	1/30 sec

## III. THE CHARACTERISTIC WAVELENGTH

The domain covered by the present study is shown on the Weber number–Reynolds number chart of Fig. 3. The following definitions apply,

$$We = \rho V^2 D / \sigma, \quad (1)$$

$$Re = \rho V D / \mu \quad (2)$$

where  $\rho$ ,  $V$ ,  $D$ ,  $\sigma$ , and  $\mu$  are, respectively, the jet density, velocity, diameter, surface tension (in contact with air), and viscosity. As illustrated in Fig. 2, (a) and (b) denote the extremities of the photographed portion of the jet. The complete photographic record is available in a thesis written by Stockman.<sup>20</sup> Due to space limitations, in the present paper we analyze only a representative sample of this record.

Three photographs of the fast capillary jet flow are shown in Figs. 4(a), 5(a), and 6(a). Each photograph corresponds to one of the three different liquids used in this study. It is useful to take a close look at the shape (contour) of the photographed jets in order to recognize the large-scale meandering path followed by the jet. As the jet fluid viscosity increases from Figs. 4(a) to Fig. 6(a), the sharpness of the meandering path is enhanced to the point where, in Fig. 6(a), the sinusoidal contour of the jet is illustrated with amazing clarity.

The central objective of our study was to document in quantitative terms the meandering shape of fast capillary jets. To meet this objective, the jet contours were subjected to a wavelength analysis. In each case, the jet contour was projected (enlarged) on a screen and traced by hand on paper. This operation produced two waveforms, one for the upper edge of the jet column and another for the lower edge. The waveforms were then digitized and fed into a computer program which calculated their Fourier transforms and determined the respective power spectra and cross correlation functions.

In order to learn how the characteristic wavelength var-

TABLE II. Physical properties of the working fluids.

Fluid	Density (g/cm <sup>3</sup> )	Viscosity (cSt)	Surface tension (g/s <sup>2</sup> )
I. Distilled water (18 °C)	1	1	73
II. Glycerol–water, 30% by volume (20 °C)	1.18	17	68
III. Glycerol–water, 70% by volume (20 °C)	1.24	333.6	64.5

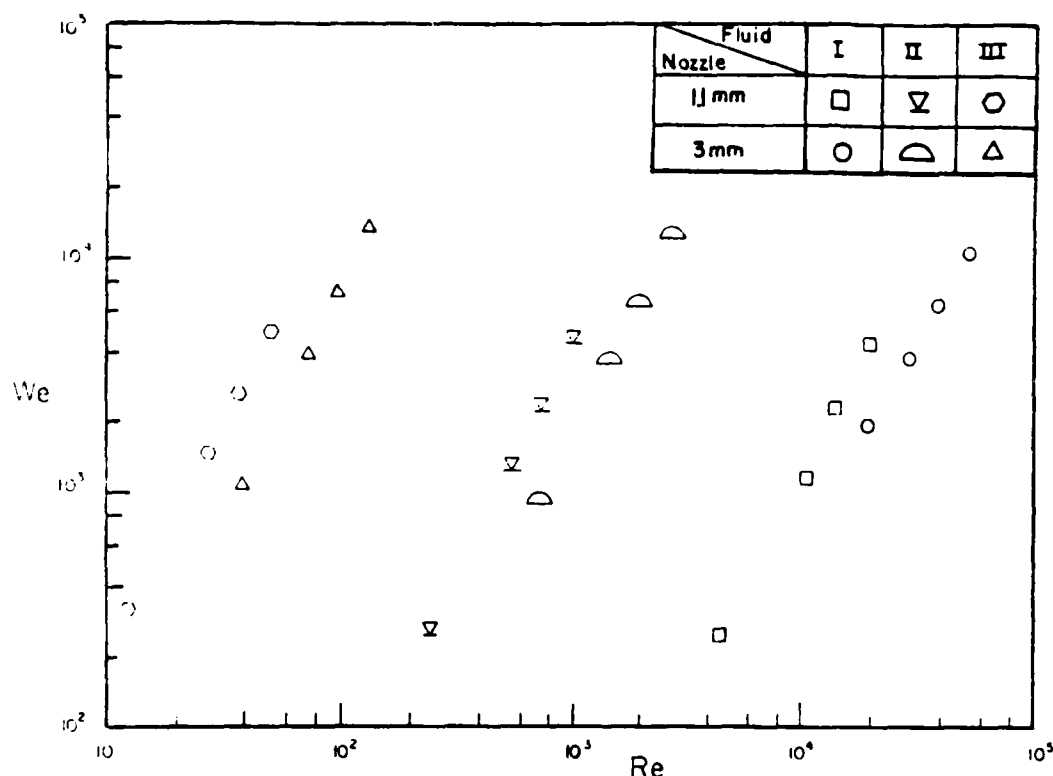


FIG. 3. Weber number-Reynolds number domain covered by the present experiments.

ies with position along the jet, each photographed contour was divided into a number of segments [for example, three segments for the jet column shown in Fig. 4(a)]. Each segment was analyzed, and the results are presented in Figs. 4-6 as power spectra with  $\lambda/D$  on the abscissa and  $P^*$  on the ordinate.  $P^*$  is defined by

$$P^* = \frac{1}{D^4} \lim_{T \rightarrow \infty} \frac{1}{T} \int_0^T |X(f)|^2 dt, \quad (3)$$

$$X(f) = \int_{-\infty}^{\infty} x(t) e^{-j\omega t} dt, \quad (4)$$

where  $x(t)$  is the contour waveform,  $\omega = 2\pi f$ ,  $f = V/\lambda$ , and  $T$  is the sample length.

Figures 4(b)-4(d) demonstrate that, regardless of longitudinal position along the jet axis, the upper and lower waveforms have a single (narrow) band of wavelengths which dominate the power spectrum. In this study we refer to the predominant wavelength ( $\lambda$  corresponding to maximum  $P^*$ ) as the meander wavelength  $\lambda_{\max}$ . Figures 4(b)-4(d) show also that the upper and lower waveforms have the same meander wavelength and, in all cases, the meander wavelength scales with the jet diameter. Furthermore, the upper and lower waveforms are *in phase*: this conclusion follows from the cross correlation function

$$r^* = \frac{1}{D^2} \lim_{T \rightarrow \infty} \frac{1}{T} \int_0^T x(t) y(t + \tau) dt, \quad (5)$$

where  $x(t)$  and  $y(t)$  are the two waveforms, and  $\tau$  is the predetermined phase shift (lag) between the two waveforms. As shown in Fig. 4(e) the cross correlation function  $r^*$  reaches

its peak value at zero lag, which indicates that the upper and lower waves are in phase. In conclusion, the flow regime documented in this study is not axisymmetric (varicose), but one which is characterized by a large-scale sinuous shape of wavelength  $\lambda_{\max}$ .

Similar conclusions regarding the existence of a characteristic meander wavelength emerge from the analysis of Figs. 5(a) and 6(a). Due to space limitations, only two samples are reported here as Figs. 5(b) and 6(b), while the complete record of the wavelength analysis may be found in Ref. 20.

Figure 7 shows a summary of the  $\lambda_{\max}$  measurements yielded by the present study. The plotted  $\lambda_{\max}$  represents the average over the given  $x$  segment, however, in reality the meander wavelength is continuous in  $x$ .

#### IV. DISCUSSION OF EXPERIMENTAL RESULTS

A theoretical interpretation of the present results is possible, based on both the theory of hydrodynamic stability and the buckling theory of fluid columns. Batchelor and Gill<sup>21</sup> considered the linear stability problem associated with an inviscid round jet discharging into a quiescent fluid. They showed that sufficiently far downstream from the nozzle, the jet is least stable to a temporal nonaxisymmetric ("sinuous"<sup>21</sup>) disturbance whose axial wavelength is larger than several times the jet diameter. Similar conclusions were reached by Mattingly and Chang,<sup>22</sup> who treated the linear stability of spatial disturbances imposed on the same jet configuration. In addition, Mattingly and Chang<sup>22</sup> studied the

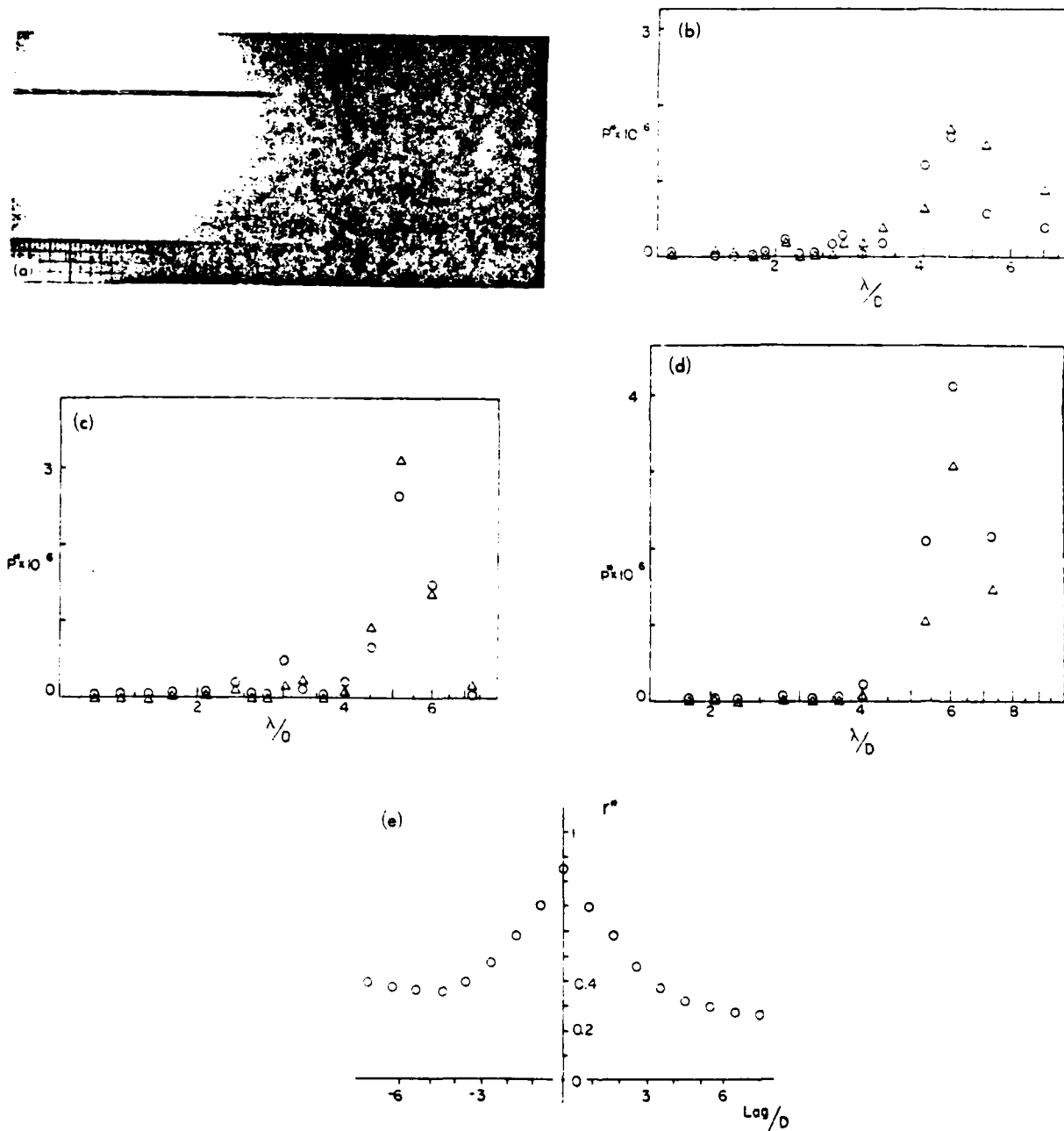


FIG. 4. Meandering jet of fluid I,  $D = 1.1$  mm,  $V = 17$  m/sec,  $a = 0$  mm,  $b = 165$  mm. (a) photograph, (b) spectral density of segment 51-71 mm downstream from nozzle, (c) spectral density of segment 71-91 mm downstream from nozzle, (d) spectral density of segment 91-111 mm downstream from nozzle, (e) cross-correlation function of segment 51-71 mm downstream from nozzle. The upper and lower waveforms are labeled  $\Delta$  and  $\circ$ , respectively.

natural instability of the jet in the laboratory and reported excellent agreement between experimental measurements and theoretical stability predictions. The same problem and conclusions were discussed in a most recent study by Lopez and Kurzweg.<sup>23</sup>

The connection between the nonaxisymmetric shape and fast capillary jets and the least stable disturbance pre-

dicted in Refs. 21-23 was recognized by Hoyt and Taylor.<sup>24</sup> Based on photographs similar to the ones obtained in the present study, Hoyt and Taylor<sup>24</sup> were able to identify a visible axial wavelength of what is clearly a nonaxisymmetric jet shape. In Fig. 10 of their study, Hoyt and Taylor<sup>24</sup> report that the visible axial wavelength increases in the downstream direction, much in the same manner as  $\lambda_{max}$  of fluids

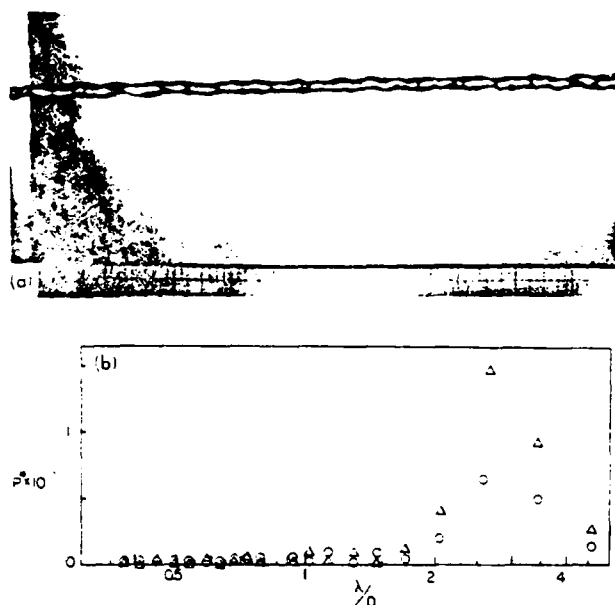


FIG. 5. Meandering jet of fluid II,  $D = 3$  mm,  $V = 11.2$  m/s,  $a = 146$  mm,  $b = 324$  mm. (a) photograph, (b) spectral density of segment 168-183 mm downstream from nozzle; the upper and lower waveforms are labeled  $\Delta$  and  $O$ , respectively.

I and II considered in the present study (Fig. 7). Inspired by the existing theoretical work of Batchelor and Gill<sup>21</sup> and Mattingly and Chang,<sup>22</sup> Hoyt and Taylor<sup>24</sup> interpreted their two-dimensional photographic record as a helical (three-dimensional) instability with long axial wavelength, as predicted by stability theory.

In a more recent experimental report, Freeman and Tavlarides<sup>25</sup> showed that when a liquid jet is suspended in a

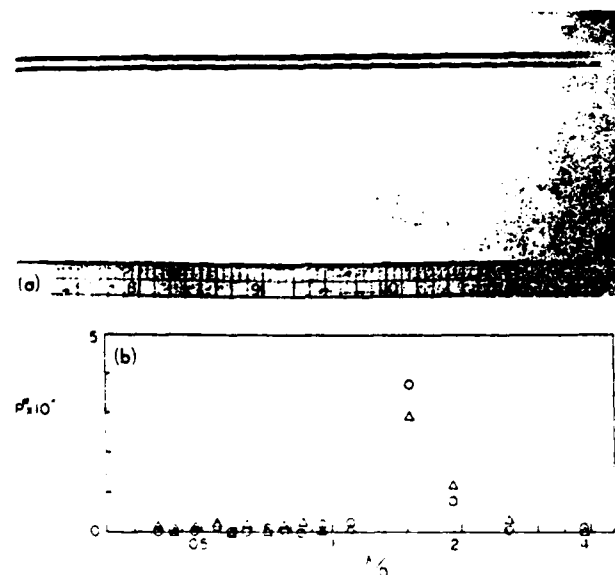


FIG. 6. Meandering jet of fluid III,  $D = 3$  mm,  $V = 15.2$  m/sec,  $a = 140$  mm,  $b = 305$  mm. (a) photograph, (b) spectral density of segment 267-278 mm downstream from nozzle; the upper and lower waveforms are labeled  $\Delta$  and  $O$ , respectively.

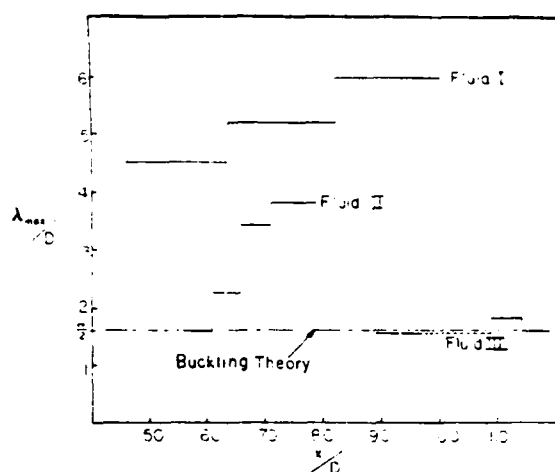


FIG. 7. The measured meandering or buckling wavelength versus longitudinal position along the jet.

confluent stream, the jet develops a nonaxisymmetric shape when the relative velocity between jet and stream reaches a high enough value. Figures 2 and 3(a) published by Freeman and Tavlarides<sup>25</sup> show a sinuous contour whose ratio (axial wavelength)/(diameter) appear to be nearly identical to the ratio visible in Fig. 6(a) of the present study. Specifically, averaging over three complete wavelengths visible in Fig. 2 of Ref. 25, we obtain  $\lambda_{\max}/D \approx 1.67$ . Also, averaging over four complete wavelengths visible in Fig. 3(a) of Ref. 25 we estimate  $\lambda_{\max}/D \approx 1.47$ . Note that these two values of  $\lambda_{\max}/D$ , 1.67 and 1.47, fall right in the middle of the narrow band of characteristic wavelengths revealed by the power spectrum of Fig. 6(b) in the present study.

To summarize, classical hydrodynamic stability arguments predict correctly the instability of the jet column to nonaxisymmetric disturbances, as well as the scale of the axial wavelength of such disturbances. However, there is one additional result which now has been documented by three independent experiments (Refs. 24 and 25 and the present study) which is not predicted by existing hydrodynamic stability analyses. This additional result is the tendency of the nonaxisymmetric wave to show a  $\lambda_{\max}/D$  value which approaches 1.5 in a region close enough to the nozzle where, as discussed by Hoyt and Taylor,<sup>24</sup> the nonaxisymmetric disturbance has not had time to be amplified due to the form drag interaction between the liquid jet and the ambient air.

Insight into the origins of this additional feature is offered by the *buckling* of fluid columns.<sup>26-31</sup> It is worth noting that as a theoretical viewpoint in fluid mechanics, the buckling theory is much newer than hydrodynamic stability theory. The novelty of the concept of fluid column buckling may indeed be responsible for the early interpretation of nonaxisymmetric disturbances in fast capillary jets as helical. In fact, the experimental record available for this interpretation is exclusively two-dimensional and, as such, the *same* record can be interpreted as evidence of local buckling in a plane determined randomly by the presence of random disturbances at the air interface.

This alternative interpretation is recommended strongly.

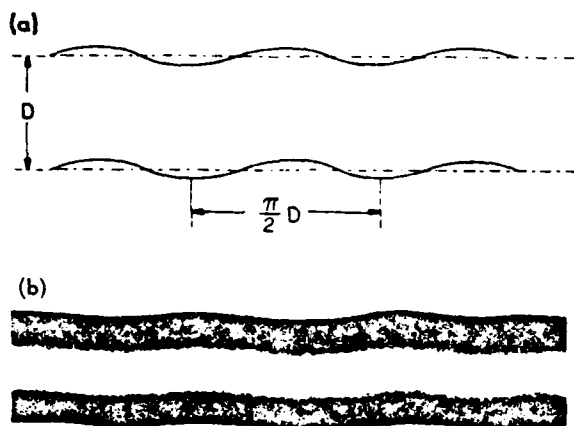


FIG. 8. The theoretical (Ref. 30,31) shape of a buckled inviscid jet vis-à-vis a closeup of Fig. 6(a).

ly by the first observations of fast capillary jet flow, in particular by Weber's<sup>15</sup> Figs. 1(b), 1(d), and 1(e). In these early photographs the lateral deformation of the liquid column has a local (nonperiodic) character, however, the wavelength of this deformation is always a characteristic multiple of the jet thickness. The same effect is visible in Fig. 6(a) of the present study, where entire sections of the jet appear to be undisturbed while other segments show the characteristic wave  $\lambda_{\max}$ .

Theoretically, it has been shown that a column of viscous fluid can buckle in a way similar to rods in axial compression,<sup>26,27</sup> however, the wavelength of the buckled shape depends solely on the wavelength of the initial lateral disturbance. On the other hand, for a column of *inviscid fluid*, it is found that the buckling wavelength always scales with the column diameter,<sup>30,31</sup>  $\lambda/D = \pi/2 = 1.57$ . This prediction can then serve as explanation for the observed axial wavelength of incipient nonaxisymmetric deformations in fast capillary columns.

Figure 8 compares graphically the theoretical buckling shape of a round jet<sup>30,31</sup> with a closeup view of the jet photographed in Fig. 6(a). The similarity of the two waveforms is striking.

A strong indication that the buckling theory of inviscid jets accounts correctly for the meandering wavelength documented in this study is that the wave of Fig. 6(a) agrees well with the wave photographed by Freeman and Tavlarides.<sup>25</sup> Note that for fluid III the Reynolds number is in the range 10–100 and the Weber number in the range  $10^3$ – $10^4$ ; these ranges are quite different from Ref. 25 where  $Re \sim 10^3$  and  $We \sim 14$ . The fact that despite such discrepancies the photographed wavelengths agree with each other and with the buckling wavelength  $\pi D/2$  supports the buckling theory very strongly. The key result of the buckling theory is that the buckling wavelength must depend only on  $D$ , in other words, it must be independent of  $V$  and physical properties.

For the same reason, the fact that for fluids I and II  $\lambda_{\max}$  increases with  $x$  is a reflection of the thickening of the air stream entrained by the liquid jet. Thus, sufficiently far downstream the liquid jet meanders according to the buckled shape of the surrounding (thicker) air stream.

The connection between the nonaxisymmetric flow of fast jets and fluid buckling requires further study. Some researchers have already expressed the view that fluid buckling may serve as origin for the turbulent motion of fluids.<sup>30–33</sup> Along the same lines, it is interesting to note Lopez and Kurzweg's statement that the nonaxisymmetric instability of jet flow may actually account for "the breakdown phenomenon in boundary layer flow," hence, for the well-documented bursting process.<sup>34</sup>

## ACKNOWLEDGMENTS

This research was conducted under the auspices of the Office of Naval Research. The experimental apparatus was constructed by Karl Rupp.

- <sup>1</sup>G. Bidone, *Imprimerie Royal*, Turin, Italy, 1–136 (1829).
- <sup>2</sup>E. Savart, *Ann. Chem.* **53**, 337 (1833).
- <sup>3</sup>Lord Rayleigh, *The Theory of Sound* (Dover, New York, 1945), Chap. XX.
- <sup>4</sup>S. Chandrasekhar, *Hydromechanics and Hydromagnetic Stability* (Clarendon, Oxford, 1961).
- <sup>5</sup>L. Crane, S. Birch, and P. McCormack, *Brit. J. Appl. Phys.* **15**, 743 (1964).
- <sup>6</sup>R. Donnelly and W. Glaberson, *Proc. R. Soc. London Ser. A* **290**, 547 (1966).
- <sup>7</sup>M. C. Yuen, *J. Fluid Mech.* **33**, 151 (1968).
- <sup>8</sup>A. H. Nayfeh, *Phys. Fluids* **13**, 841 (1970).
- <sup>9</sup>P. Lafrance, *Phys. Fluids* **18**, 428 (1975).
- <sup>10</sup>E. F. Goedde and M. C. Yuen, *J. Fluid Mech.* **40**, 495 (1970).
- <sup>11</sup>D. F. Rutland and G. J. Jameson, *J. Fluid Mech.* **46**, 267 (1971).
- <sup>12</sup>K. C. Chaudhary and L. G. Redekopp, *J. Fluid Mech.* **96**, 257 (1980).
- <sup>13</sup>K. C. Chaudhary and T. Maxworthy, *J. Fluid Mech.* **96**, 275 (1980).
- <sup>14</sup>K. C. Chaudhary and T. Maxworthy, *J. Fluid Mech.* **96**, 287 (1980).
- <sup>15</sup>C. Weber, *Z.A.M.M.* **11**, 136 (1931).
- <sup>16</sup>A. Haenlein, *Forschung* **2**, 139 (1931).
- <sup>17</sup>L. Prandtl, *Essentials of Fluid Dynamics* (Blackie and Son, London, 1969), p. 325.
- <sup>18</sup>J. W. Hoyt, J. J. Taylor, and C. Runge, *J. Fluid Mech.* **63**, 635 (1974).
- <sup>19</sup>J. W. Hoyt and J. J. Taylor, *Phys. Fluids* **20**, S253 (1977).
- <sup>20</sup>M. G. Stockman, M. S. thesis, University of Colorado, Boulder, Colorado, 1981.
- <sup>21</sup>G. K. Batchelor and A. E. Gill, *J. Fluid Mech.* **14**, 529 (1962).
- <sup>22</sup>G. E. Mattingly and C. C. Chang, *J. Fluid Mech.* **65**, 541 (1974).
- <sup>23</sup>J. L. Lopez and U. H. Kurzweg, *Phys. Fluids* **20**, 860 (1977).
- <sup>24</sup>J. W. Hoyt and J. J. Taylor, *J. Fluid Mech.* **83**, 119 (1977).
- <sup>25</sup>R. W. Freeman and L. L. Tavlarides, *Phys. Fluids* **22**, 782 (1979).
- <sup>26</sup>J. D. Buckmaster, A. Nachman, and L. Ting, *J. Fluid Mech.* **69**, 1 (1975).
- <sup>27</sup>J. D. Buckmaster and A. Nachman, *Q. J. Mech. Appl. Math.* **31**, 157 (1978).
- <sup>28</sup>S. M. Suleiman and B. R. Munson, *Phys. Fluids* **24**, 1 (1981).
- <sup>29</sup>B. R. Munson, *Phys. Fluids* **24**, 1780 (1981).
- <sup>30</sup>A. Bejan, *Lett. Heat Mass Transfer* **8**, 187 (1981).
- <sup>31</sup>A. Bejan, *Phys. Fluids* **24**, 1766 (1981).
- <sup>32</sup>B. R. Munson, *Phys. Fluids* **24**, 1766 (1981).
- <sup>33</sup>J. O. Cruickshank, Ph. D. thesis, Iowa State University, Ames, Iowa, 1980.
- <sup>34</sup>H. T. Kim, S. J. Kline, and W. C. Reynolds, *J. Fluid Mech.* **50**, 133 (1971).



## Theory of Instantaneous Sinuous Structure in Turbulent Buoyant Plumes

A. Bejan, Boulder, Colorado

**Abstract.** This paper reports a theory which explains the flickering motion of turbulent plumes as well as their large-scale sinuous structure. The theory is based on the fact that the inviscid region of the plume (the "plume column") possesses elastic properties analogous to those of elastic rods subjected to longitudinal compression. It is shown that the straight plume column is not stable and buckles. The distance between two consecutive elbows is proportional to the local plume diameter, in other words, the shapes of all buckled plumes are geometrically similar. A buckled plume collapses periodically due to the interaction of its lateral elbows with the stagnant ambient. This interaction is responsible for the intermittent formation of large-scale buoyant eddies on the periphery of the turbulent plume.

### Theorie der veränderlichen gewundenen Struktur in turbulenten Auftriebsfahnen

**Zusammenfassung.** Diese Arbeit versucht, die flatternde Bewegung turbulenter Auftriebsfahnen und ihre großräumige gewundene Struktur aufzuklären. Man geht davon aus, daß der nicht-zähe Bereich der Fahne (die „Fahnnensäule“) elastische Eigenschaften besitzt ähnlich jener elastischer Stäbe, die longitudinalen Verdichtungen unterworfen sind. Die gerade Fahnnensäule ist nicht stabil und verbiegt sich. Der Abstand zwischen zwei Krümmungen ist dem örtlichen Fahnnendurchmesser proportional, d. h. die Formen aller gekrümmten Fahnen sind geometrisch ähnlich. Die gekrümmte Fahne bricht periodisch zusammen infolge der Wechselwirkung ihrer zeitlichen Krümmungen und der ruhenden Umgebung. Dadurch entstehen intermittierend großräumige Auftriebswirbel am Umfang turbulenter Auftriebsfahnen.

### 1 Introduction

Turbulent plumes represent an extremely frequent natural phenomenon, in the atmosphere as well as in the hydrosphere. Furthermore, in heat transfer and environmental engineering, the turbulent plume constitutes one of the most effective mixing mechanisms known to man. The state of knowledge on turbulent plumes has been summarized by Turner [1] and, as part of a comprehensive monograph on buoyancy-driven flows, by Turner [2]. Another extensive overview of the field was published most recently by Fischer, List, Koh, Imberger and Brooks [3]. A critical examination of these review works leads to

the conclusion that the favored approach in turbulent plume research is one where the "complications" of the turbulent flow field can be smoothed out by the classic method of time-averaging (Townsend, [4]). Consequently, most of the theoretical work on buoyant jets relies on the axisymmetric flow model which lends itself very well to boundary layer-type analysis.

Although mathematically attractive, the time-averaged turbulent plume concept does gross injustice to the physics of the phenomenon. A turbulent exhaust plume does not rise straight up into the air, with a fixed shape resembling that of an inverted cone or funnel. A real plume executes a periodic lateral movement; the plume is not straight, rather, it has recognizable bends separated by distances of the same order as the plume diameter. The smoke rising from a barbecue or camp fire "snakes" into the air. This large scale motion, which is so effectively blacked out by time-averaging, can be seen clearly in Fig. 1.

The object of this paper is to present a theory which explains for the first time the instantaneous structure and the "flickering" nature of turbulent plumes.

### 2 The Concept of Elastic Plume Column

Consider a fluid of density  $\rho$  rising vertically through a heavier fluid of density  $\rho + \Delta\rho$ . We model the starting section of this buoyant stream as inviscid. This means that for a certain height at the base of the plume we are neglecting the shear interaction between the plume fluid and the stagnant ambient. This is permissible for a height of the order of 4-6 times the plume diameter, where, as shown by Crow and Champagne [5], the plume-ambient shear layer is thin compared with the plume diameter. Having neglected the interaction at the plume-ambient interface, it is helpful to imagine the plume fluid as being surrounded by a thin flexible sleeve (control surface) which is stationary with respect to the stagnant ambient.



Fig. 1. Large-scale periodic structure in the plume above a natural gas well on fire – Douglas Pass, Colorado (AP Laserphoto, reprinted from the Longmont Daily Times-Call, Oct. 18–19, 1980)

Imagine now a cut perpendicular to the plume axis. If the column is straight, in the cross-section generated by the cut we distinguish only the compressive force (impulse [6])

$$C = \iint_A \rho V^2 dA, \quad (2.1)$$

where  $V$  and  $A$  are the plume velocity and cross-sectional area. If the plume column is slightly curved, we distinguish also a cross-sectional bending moment  $M$ . This bending moment is due primarily to the fact that the plume fluid travels relatively faster through regions of the cut which are located on the inside bank of the bend. It is easy to show that the cross-sectional bending moment  $M$  is present as soon as the column acquires curvature. Consider for this purpose a bending test in which the uniform stream ( $\rho, V, A$ ) passes through a slightly curved duct: the radius of curvature of the duct centerline  $R_\infty$  is infinitely greater than the plume diameter,  $D$ . The Bernoulli equation applied along a streamline requires (Prandtl [7]),

$$\frac{1}{2} \rho V^2 = \frac{1}{2} \rho v^2 + P \quad (2.2)$$

where the left hand side applies to the straight section ( $P=0$ ) while the right hand side corresponds to the curved section. Equilibrium in the radial direction requires also (Prandtl [8]),

$$\frac{\rho V^2}{R_\infty} = - \frac{dP}{dr} \quad (2.3)$$

where  $r$  is the radial coordinate measured in the plane of curvature away from the plume centerline, toward the center of curvature. Combining Eqs. (2.2) and (2.3), we obtain

$$v = V \left[ 1 - \frac{r}{R_\infty} \right], \quad \frac{v}{R_\infty} \rightarrow 0 \quad (2.4)$$

The cross-sectional bending moment  $M$  can now be calculated by writing

$$M = \iint_A (\rho v^2 + P) r dA \quad (2.5)$$

which, using Eqs. (2.4) and (2.2), yields

$$M = \frac{\rho V^2}{R_\infty} \iint_A r^2 dA. \quad (2.6)$$

Note that the area integral appearing in Eq. (2.6) is the area moment of inertia ( $I = \pi D^4/64$ ) employed routinely in the study of elastic beam flexure (Den Hartog [9]). The group  $\rho V^2$  plays the role of "modulus of elasticity": this is why it becomes increasingly difficult to manually bend a hose as the turbulent (inviscid) flow rate through it increases.

At this point we conclude that the plume column is in axial compression and that the cross-sectional bending moment is proportional to the curvature of the centerline ( $1/R_\infty$ ). With such properties, the straight plume column becomes analogous to an elastic column subjected to axial compression (Den Hartog [10]). This analogy guarantees that if the plume is tall enough, it will buckle like an elastic rod compressed between the ends. In the next section we develop the "buckling theory" of turbulent plumes viewed as elastic columns.

### 3 The Natural Buckling of a Straight Plume Rising from Rest

Consider the stationary control volume defined by two cuts normal to the plume column, at  $z$  and  $z + dz$  (Fig. 2). The balance of vertical forces acting on this volume dictates

$$\frac{dC}{dz} = \rho g A g, \quad (3.1)$$

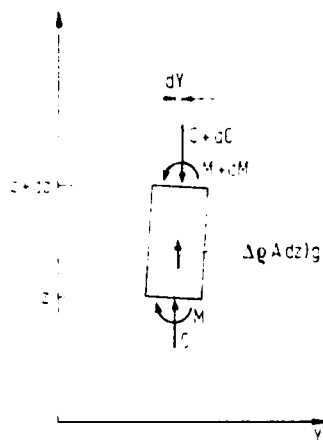


Fig. 2. Static equilibrium of a segment of vertical plume column

The conservation of mass through the control volume requires also

$$V(z) A(z) = Q, \quad \text{constant}, \quad (3.2)$$

where  $Q$  is the volumetric flowrate through the plume column. Combining these conservation statements we obtain

$$V(z) = \left( 2 \frac{\Delta \rho}{\rho} g z \right)^{1/2}, \quad A(z) = Q/V(z), \quad (3.3)$$

where we made the additional assumption that the plume fluid originates from rest,  $V(0) = 0$ .

As in the buckling theory of a vertical flagpole (Timoshenko and Gere [11]; Den Hartog [12]), the rotational equilibrium of the plume element  $dz$  requires

$$C dY + M - (M + dM) = 0 \quad (3.4)$$

or, using Eq. (2.1) and (2.6),

$$\rho A V^2 \frac{dY}{dz} + \frac{d}{dz} \left( \rho I^{1/2} \frac{d^2 Y}{dz^2} \right) = 0. \quad (3.5)$$

Note that in the limit of vanishingly small curvature,  $1/R_\infty = -d^2 Y/dz^2$ . Taking into account the  $z$ -dependence of  $V$  and  $A$ , Eq. (3.3), the equation of flexure (3.5) becomes

$$\frac{d^3 Y}{dz^3} + \frac{4\pi(2g \Delta \rho / \rho)^{1/2}}{Q} z^{1/2} \frac{dY}{dz} = 0. \quad (3.6)$$

The first important conclusion of this analysis is that the plume column develops a "structure" whose characteristic vertical dimension scales with

$$z_0 = \left( \frac{Q^2}{32\pi^2 g \Delta \rho / \rho} \right)^{1/5}. \quad (3.7)$$

The vertical length scale can also be written as

$$z_0 = \left( \frac{z D^4}{256} \right)^{1/5}, \quad \text{constant} \quad (3.7a)$$

where  $D(z)$  is the plume diameter at level  $z$  (note that  $D(z) \sim z^{-1/4}$ ). Introducing the dimensionless coordinate  $x = z/z_0$ , the equation of flexure becomes

$$\frac{d^3 Y}{dx^3} + x^{1/2} \frac{dY}{dx} = 0. \quad (3.8)$$

The general solution to this equation is expressible in terms of Bessel functions (Watson [13])

$$\frac{dY}{dx} = K_1 x^{1/2} J_{2/5}(4/5 x^{5/4}) + K_2 x^{1/2} J_{-2/5}(4/5 x^{5/4}) \quad (3.9)$$

where  $K_1$  and  $K_2$  are arbitrary constants. Noting that

$$\lim_{x \rightarrow 0} \frac{dY}{dx} = K_1 x + K_2, \quad (3.10)$$

we set  $K_2 = 0$ , which accounts for the fact that in the very beginning the buoyant fluid rises vertically. The shape of the plume column,  $Y(x)$ , is obtained by integrating (3.9),

$$Y(x) = K \int_0^{\xi} m^{1/5} J_{2/5}(m) dm \quad (3.11)$$

where

$$\xi = 4/5 x^{5/4}. \quad (3.12)$$

The integral appearing in (3.11) was calculated with sixth-digit accuracy, by first expanding  $J_{2/5}(m)$  in a power series. The principal values of this integral are reported here in Table 1, because they are not available in the literature.

Table 1

$\xi$	$\int_0^{\xi} m^{1/5} J_{2/5}(m) dm$
0.5	0.172638
1	0.492870
1.5	0.852135
2	1.168617
2.5	1.380308
3	1.452918
3.5	1.384381
4	1.203166
4.5	0.960384
5	0.717376
5.5	0.531599
6	0.443935
6.5	0.470241
7	0.598886
7.5	0.794658
8	1.007952
8.5	1.186949
9	1.289889
9.5	1.294589
10	1.203059
10.5	1.040267
11	0.847522
11.5	0.672151
12	0.556040
12.5	0.525758
13	0.586530

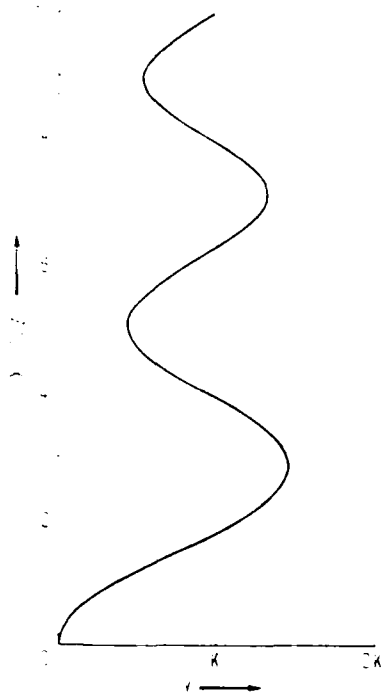


Fig. 3. The buckled shape of the plume column centerline

The magnified shape of the buckled plume column is shown in Fig. 3 as the function  $Y(x)/K$ . It should be remembered that Eq. (3.11) is the result of a small amplitude analysis ( $dY/dz \ll 1$ ), hence, the amplitude  $K$  is negligible when compared with the vertical length scale  $z_0$ . The static equilibrium of the straight plume column is indifferent [10]; however, given the slightest lateral disturbance, the plume buckles in accordance with the vertical periodicity shown in Fig. 3. The buckled shape is a succession of elbows whose spatial frequency increases with height. The first four elbows are located at

$$x_1 = 2.878, \quad x_2 = 5.101, \quad x_3 = 7.101, \quad x_4 = 8.967.$$

According to the classical arguments of Hydrodynamic Stability Theory [14], the sinuous shape will be amplified due to the dynamic interaction of the elbows with the stagnant ambient. It is this interaction which leads to the formation of large turbulent eddies visible in most atmospheric plumes (Fig. 1).

#### 4 Formation and Evolution of Large Eddies

The mechanism of elbow turbulence formation is shown schematically in Fig. 4. Speaking only qualitatively, in the first phase of the process the segment of plume column located in the vicinity of a natural elbow is pushed to the side by the horizontal resultant of the two axial compressive forces. The lateral movement of the elbow is eventu-

ally blocked by the pressure build-up associated with either the stagnation of some plume fluid into the still ambient, or with accelerating some of the ambient fluid. This pressure build-up is consistent with the fact that in a column of finite curvature the pressure increases in the radial direction, Eq. (2.3). At the end of the first phase of the process, the elbow has degenerated into a buoyant eddy of mixed fluid; this eddy rotates as shown in the figure, and rises slower than the unmixed plume fluid found at the same altitude.

The second phase of the mechanism is triggered by the effect of high pressure nodules already present on both sides of the plume column: the plume buckles in a new mode, feeding its stream through the structures generated by the old set of elbows. At the end of the second phase, the new column gives birth to a new set of large eddies which continue to rise. In general, the eddies produced by the upper elbows interfere with older eddies rising from lower levels. This interaction is partly responsible for lateral growth of the turbulent plume, as  $x$  increases.

The most regular feature in the evolution of the turbulent plume column is the root section,  $0 < x < x_1$ , which precedes the formation of the first elbow. The root of the plume swings back and forth, not necessarily in the same plane, with a characteristic frequency,  $f_1 = 1/(2\Delta t)$ . The half period  $\Delta t$  of this flickering motion can be calculated by integrating the first of equations (3.3):  $\Delta t$  is the time interval needed by plume fluid to rise from  $z = 0$  to the first elbow,  $z_1 = x_1 z_0$ . Combining this result with Eqs. (3.7) and (3.3), we discover that the Strouhal number based on the plume velocity and diameter at the first elbow,  $V_1$  and  $D_1$ , is a universal constant for all inviscid (turbulent) plumes

$$St_1 = \frac{f_1 D_1}{V_1} = 0.534. \quad (4.1)$$

Another interesting result of the buckling theory is that the large elbow structure (the distance between elbows) scales only with the plume diameter, which means that the buckled shapes of all inviscid plumes are geometrically similar. This prediction agrees with the observed structure

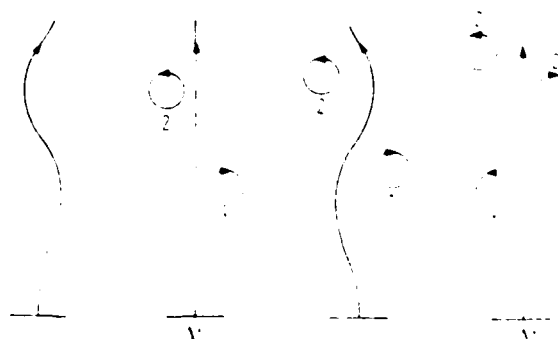


Fig. 4. Mechanism of formation of large-scale eddies in a turbulent plume rising from rest

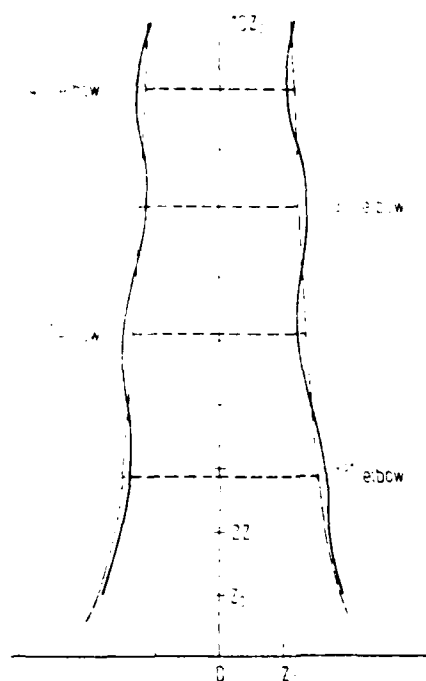


Fig. 5. Universal geometry of buckled plume columns

of atmospheric plumes. According to Eq. (3.7a), the plume diameters corresponding to the first four elbows are,

$$\frac{D_i}{z_0} = \frac{4}{x_i^{1/4}} = 3.071, 2.662, 2.45, 2.332. \quad (4.2)$$

Figure 5 shows a scale drawing of a round plume and the relative location of the first four elbows. This universal geometry agrees very well with visual observations of turbulent plumes rising above barbecues and camp fires. It also agrees with the plume photographed in Fig. 1.

### 5 Laminar Plumes vs. Turbulent Plumes: The Transition

The instantaneous sinuous structure and the eddy formation mechanism described so far, apply only to large Reynolds number (turbulent) plumes which can be modeled as inviscid. The present theory does not apply to laminar plumes. It is important to note, however, that the universality of the sinuous structure (Fig. 5) provides a theoretical explanation for the phenomenon of transition from laminar to turbulent plume flow.

According to Eq. (4.1), the base of the plume fluctuates within a characteristic time interval which is proportional to the diameter and inversely proportional to the velocity. This local characteristic time,

$$t_{\text{fluctuation}} \sim \frac{D_i/V_i}{S/V_i} \quad (5.1)$$

represents the "natural heartbeat" of the plume as an inviscid stream. If the plume flow is highly viscous (laminar), the plume column has a different characteristic time: the viscous local time is associated with the travel of information by viscous diffusion from the plume-ambient interface to the plume centerline (total distance  $D/2$ ). The viscous communication time is given by the solution to Stokes' first problem [15],

$$\frac{D_i/2}{2(\nu t_{\text{viscous}})^{1/2}} \sim 1, \text{ or } t_{\text{viscous}} \sim \frac{D_i^2}{16\nu}. \quad (5.2)$$

The plume flow remains laminar if the ambient can communicate viscously with the stream faster than the stream can fluctuate. If the column can fluctuate faster than the viscous diffusion time, then, of course, the flow opts for the inviscid (turbulent) regime. At transition, the viscous and inviscid time scales are of the same order of magnitude; combining Eqs. (5.1) and (5.2) we conclude that the laminar-turbulent transition is marked by

$$\frac{V_i D_i}{\nu} \sim 30. \quad (5.3)$$

This theoretical estimate of the transition Reynolds number agrees very well with experimental observations and with estimates based on hydrodynamic stability experiments. Experimentally, it is well known that the transition in free jet and wake flow occurs in the vicinity of  $Re \sim 30$  (see, for example, Schlichting [16]). The hydrodynamic stability of buoyant plumes and wall layers has been studied extensively, as summarized by Gebhart [17]. For example, the lowest Reynolds number where instability has been detected in vertical laminar boundary layer flow over a constant-flux wall is of order 67 (Fig. 8-21, [17]). The difference between this estimate and Eq. (5.3) is explained by the fact that in [17] the local Reynolds number ( $G^*$ ) is based on the thickness of the laminar boundary layer. If, instead, the Reynolds number is expressed based on the displacement or momentum thickness (more consistent with the slug flow model employed in the present theory) the transition  $Re$  is a number of the same order as in Eq. (5.3).

### 6 Concluding Remarks

The demonstrated ability to correctly predict the transition to turbulence is additional evidence that the sinuous structure (Fig. 5) and the characteristic time scale (Eq. 4.1) are real properties of all turbulent buoyant plumes. It is important to recognize also that the *large-scale buckling phenomenon* described in this paper is not observed only in buoyant plumes as in Fig. 1. The same phenomenon has been observed and described as "orderly structure", "corkscrew shape", and "whiplash motion" in the starting section of low speed turbulent jets (Crow and Champagne [5]; Reynolds [18]). Others have recognized this snake-like

shape as the cause of the intermittency phenomenon (Yih [19], Fig. 8b, and pp. 545, 546). In the field of boiling heat transfer we are familiar with the occurrence of tall S-shaped vapor bubbles (buckled vapor plumes) on intensely heated horizontal surfaces: this phenomenon is recognized as the "continuous vapor column regime" (Figs. 2d and 2j in Moissis and Berenson [20]).

The reader can easily reproduce the natural buckled shape by experimenting with the continuous water column falling from the kitchen faucet. This water column is a "sinking" plume defined not by a flexible plume-ambient interface as in Fig. 1, but by the flexible hose provided by capillary forces. Placing his finger about 1–2 cm under the faucet, the reader can buckle this sinking plume into a shape which resembles very closely the shape shown in Fig. 5, rotated by 180°. In the kitchen faucet experiment the buckled column does not break up, since the lateral growth of its elbows is suppressed by the effect of surface tension. The same stabilizing effect is present in the S-shaped tall bubbles photographed during intense boiling by Moissis and Berenson [20].

From the point of view of theoretical research in fluid mechanics, the Buckling Theory reported in this paper represents a dramatic departure from accepted methods such as Hydrodynamic Stability analyses. For the first time, the Buckling Theory focuses on the equilibrium of fluid flow as a *finite size system*: the new result is that the inviscid plume possesses a new property – buckling – and that the buckled shape is behind the observed "large-scale structure" of turbulent plumes. The Buckling Theory predicts for the first time the transition to turbulent plume flow: the transition is an internal property of the stream, the competition between two stream properties ( $l_{\text{fluctuation}}$  and  $l_{\text{viscous}}$ ). Thus, the Buckling Theory explains the origin of turbulent fluid motion [21].

#### Acknowledgement

This research was sponsored by the U.S. Office of Naval Research, The Power Program, under Contract No. N00014-79-C-0006.

#### References

1. Turner, J. S.: Buoyant plumes and thermals. *Ann. Rev. Fluid Mech.* 1 (1969) 29–44
2. Turner, J. S.: *Buoyancy Effects in Fluids*. Cambridge: University Press 1979
3. Fisher, H. B.; List, E. J.; Koh, R. C. Y.; Imberger, J.; Brooks, N. H.: *Mixing in Inland and Coastal Waters*. New York: Academic Press 1979
4. Townsend, A. A.: *The Structure of Turbulent Shear Flow*. Cambridge: University Press 1976
5. Crow, S. D.; Champagne, F. H.: Orderly structure in jet turbulence. *J. Fluid Mech.* 48 (1971) 547–591
6. Shapiro, A. H.: *The Dynamics and Thermodynamics of Compressible Fluid Flow*. New York: Ronald 1953
7. Prandtl, L.: *Essentials of Fluid Dynamics*. London: Blackie & Son 1969
8. Prandtl, L.: *Op. Cit.* 47
9. Den Hartog, J. P.: *Strength of Materials*. New York: Dover 1961
10. Den Hartog, J. P.: *Op. Cit.* 184–188
11. Timoshenko, S.; Gere, J. M.: *Theory of Elastic Stability*. New York: McGraw-Hill 1961
12. Den Hartog, J. P.: *Advanced Strength of Materials*. New York: McGraw-Hill 1952
13. Watson, G. N.: *Theory of Bessel Functions*. Cambridge: University Press 1966
14. Prandtl, L.: *Op. Cit.* 51
15. Schlichting, H.: *Boundary Layer Theory*. New York: McGraw-Hill 1960
16. Schlichting, H.: *Op. Cit.* 17
17. Gebhart, B.: *Heat Transfer*. New York: McGraw-Hill 1971
18. Reynolds, A. J.: Observations of a liquid into liquid jet. *J. Fluid Mech.* 14 (1962) 552–556
19. Yih, C. S.: *Fluid Mechanics*. New York: McGraw-Hill 1969
20. Moissis, R.; Berenson, P. J.: Hydrodynamic transitions in nucleate boiling. *J. Heat Transfer*, C 85 (1963) 221–230
21. Bejan, A.: On the buckling property of inviscid jets and the origin of turbulence. *Letters in Heat and Mass Transfer* 8 (1981) 187–194

Dr. A. Bejan  
Assistant Professor  
Department of Mechanical Engineering  
Campus Box 427  
University of Colorado  
Boulder, Colorado 80309  
USA

Received 29 July, 1981

# Theoretical considerations of transition to turbulence in natural convection near a vertical wall

A. Bejan and G. R. Cunnington\*

Hydrodynamic stability analysis of an inviscid wall jet shows that instability is possible above a characteristic disturbance wavelength which is proportional to the jet thickness. This scaling is the basis for an argument that transition occurs when the fluctuating time period of the unstable (inviscid) wall jet is of the same order as the viscous diffusion time normal to the jet. The transition must occur when the jet Reynolds number is of the order of  $10^2$ . Published observations of transition along a heated vertical wall are reviewed in order to test the validity of the proposed scaling argument. Specifically, numerous observations on buoyant jets near isothermal walls, near constant-heat-flux walls, and in enclosures with vertical isothermal walls are shown to support the validity of the transition mechanism proposed.

**Key words:** convection, turbulence, fluid flow

Transition phenomena have been studied extensively during the past half-century. This work has been brought in perspective in a number of review papers, for example by Tani<sup>1</sup> and Reshotko<sup>2</sup> for boundary layer flow and by Gebhart<sup>3</sup> for natural convection flow.

The object of this study is to propose a scaling argument as basis for transition to turbulence in the wall jet flows encountered in natural convection along heated vertical walls. First, linear stability analysis of a wall jet indicates that the flow is unstable to disturbance wavelengths greater than a certain multiple of the jet thickness  $D$ . Based on this proportionality, it will be argued that transition is ruled by the internal competition between two time scales, the jet fluctuation period and the time of viscous penetration normal to the flow direction. A comprehensive review of the published experimental observations on transition supports the validity of this scaling argument. Finally, it is shown that photographs and numerical simulations of transition in vertical enclosures heated from the side visualise the transition mechanism described.

## Hydrodynamic instability of an inviscid wall jet

Consider the flow of an inviscid jet  $U(y)$  next to a vertical wall, as shown in Fig 1. We want to know the waviness of the jet as it becomes unstable, in other words, the frequency of its fluctuation relative to a fixed spot on the wall, which can be obtained by performing a linearised stability analysis of the flow. This analytical approach is outlined by Lamb<sup>4</sup>. By

superimposing on the base flow ( $u = U$ ,  $v = 0$ ) unspecified disturbances:

$$u = U + u' \quad (1)$$

$$v = v' \quad (2)$$

the inviscid flow (Euler) equations yield the vorticity transport equation:

$$\frac{\partial \tau}{\partial t} + (U + u') \frac{\partial \tau}{\partial x} + v' \frac{\partial \tau}{\partial y} = 0 \quad (3)$$

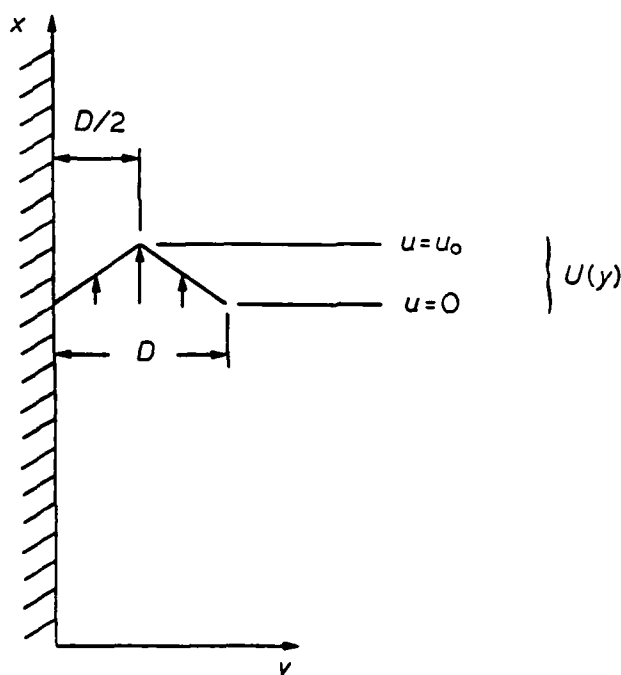


Fig 1 Wall jet velocity profile

\* Department of Mechanical Engineering, University of Colorado, Box 427, Boulder, Colorado 80309, USA

Received 9 August 1982 and accepted for publication on 12 April 1983

with the vorticity defined as:

$$\tau = \frac{\partial v'}{\partial x} - \frac{\partial u'}{\partial y} - \frac{dU}{dy} \quad (4)$$

Linearising Eq (3) yields:

$$\left( \frac{\partial}{\partial t} + U \frac{\partial}{\partial x} \right) \left( \frac{\partial v'}{\partial x} - \frac{\partial u'}{\partial y} \right) - \frac{d^2 U}{dy^2} v' = 0 \quad (5)$$

Next assume that the disturbance velocity components are both periodic in  $x$ :

$$u' = u_* e^{ikx + \sigma t} \quad (6)$$

$$v' = v_* e^{ikx + \sigma t} \quad (7)$$

where  $k$  is the wavenumber ( $k = 2\pi/\lambda$ ). Substitution of Eqs (6, 7) into the vorticity transport equation and the mass continuity equation, and the elimination of  $u_*$  yields a single equation for the transversal disturbance amplitude  $v_*$ :

$$(\sigma + kU) \left( \frac{\partial^2 v_*}{\partial y^2} - k^2 v_* \right) - \frac{d^2 U}{dy^2} k v_* = 0 \quad (8)$$

Our interest is in the wavelengths  $\lambda$  or wavenumbers  $k$  for which  $\sigma$  is imaginary, ie for which the assumed disturbance is likely to be amplified (Eqs 6, 7). As shown in Fig 1, we assume a triangular velocity profile, so that in all regions of the flow  $d^2 U/dy^2 = 0$ :

$$\text{I) } U = \frac{u_0}{D/2} y, \quad 0 < y < D/2$$

$$\text{II) } U = \frac{u_0}{D/2} (D - y), \quad D/2 < y < D \quad (9)$$

$$\text{III) } U = 0, \quad D < y$$

Solving Eq (8), the corresponding expressions for  $v_*$  in the three regions are:

$$\text{I) } v_* = A e^{-ky} + B e^{ky}$$

$$\text{II) } v_* = C e^{-ky} + D_0 e^{ky} \quad (10)$$

$$\text{III) } v_* = E e^{-ky} + F e^{ky}$$

The solid wall condition,  $v_* = 0$  at  $y = 0$ , and the condition that  $v_*$  must be finite infinitely far from the wall, mean that:

$$A + B = 0 \quad (11)$$

$$F = 0 \quad (12)$$

Two more equations follow the condition that  $v_*$  must vary continuously from region I to II, and from II to III:

$$A e^{-kD/2} + B e^{kD/2} = C e^{-kD/2} + D_0 e^{kD/2} \quad (13)$$

$$C e^{-kD} + D_0 e^{kD} = E e^{-kD} \quad (14)$$

Finally, the condition that the pressure must vary continuously from one region to the next amounts to integrating Eq (8) across one region-to-region interface (eg from  $y = D^-$  to  $y = D^+$ ):

$$(\sigma + kU) \left[ \left( \frac{\partial v_*}{\partial y} \right)_+ - \left( \frac{\partial v_*}{\partial y} \right)_- \right] - kv_* \left[ \left( \frac{dU}{dy} \right)_+ - \left( \frac{dU}{dy} \right)_- \right] = 0 \quad (15)$$

## Notation

$A, B, C,$	Coefficients (Eq 10)
$D_0, E, F$	
$D$	
$g$	
$G^*$	$5^{4/3} \left( g \frac{\beta H^4}{k\nu^2} \right)$ (Eq 49)
$H$	Vertical length scale
$k$	Wavenumber ( $2\pi/\lambda$ )
$L$	Horizontal dimension of enclosure
$m$	$\sigma D/u_0 + 1$ (Eq 18)
$N_B$	$t_w/t_{min}$ (Eq 29)
$Pr$	Prandtl number
$Ra$	Rayleigh number: $Ra_H$ —based on vertical length scale $H$ ; $Ra_L$ —based on cavity width $L$
$Re$	Reynolds number
$S$	vertical temperature gradient
$t$	Time
$T$	Temperature
$u$	Velocity parallel to the wall ( $x$ -direction)
$v$	Velocity normal to the wall ( $y$ -direction)

$u_*, v_*$	Disturbance amplitudes
$\alpha_c$	Critical wavenumber ( $2\pi L/\lambda_c$ )
$\alpha$	Thermal diffusivity
$\beta$	Coefficient of thermal expansion
$\gamma$	$e^{-kD/2}$ (Eq 18)
$\gamma$	Dimensionless stratification parameter $\left( \frac{1}{4} S \frac{L}{\Delta T} Ra_L \right)^{1/4}$
$\delta_T$	Thermal boundary layer thickness
$\delta_v$	Boundary layer where vertical velocity obeys a no-slip condition
$\lambda$	Wavelength
$\tau$	Vorticity
$\sigma$	Disturbance growth rate
$\nu$	Kinematic viscosity

## Subscripts and superscripts

*	Uniform heat flux
'	Disturbances
min	Minimum
v	Viscous
B	Buckling <sup>6,8,32</sup>



Applying this condition twice, at  $y = D/2$  and at  $y = D$ , yields two more equations:

$$D_0 \left( \frac{\sigma D}{u_0} + 1 \right) e^{kD/2} + C e^{-kD/2} = 0 \quad (16)$$

$$\left[ 1 - \frac{D}{4u_0} (\sigma + ku_0) \right] C + \left[ 1 + \frac{D}{4u_0} (\sigma + ku_0) \right] D_0 + \frac{D}{4u_0} (\sigma + ku_0) (A - B) = 0 \quad (17)$$

Eqs (11, 13, 14, 16, 17) are all homogeneous and, together, they constitute a system for determining the five unknown coefficients  $A, B, C, D_0, E$ . A non-trivial solution is possible if the determinant of this system is zero:

$$m^2 + m(2\gamma^2 + kD - 3 - \gamma^4) - \gamma^4(1 + kD) + 2\gamma^2 = 0 \quad (18)$$

where  $\gamma = e^{-kD/2}$  and  $m = \sigma D/u_0 + 1$ . Eq (18) is obtained by systematically eliminating the five coefficients among Eqs (11, 13, 14, 16, 17). Whether or not  $\sigma$  is imaginary depends on the character of  $m$ : since Eq (18) is a quadratic in  $m$ ,  $am^2 + bm + c$ , imaginary roots are possible if the discriminant  $\Delta = b^2 - 4ac$  is negative, ie when:

$$\Delta = (2\gamma^2 + kD - 3 - \gamma^4)^2 + 4\gamma^4(1 + kD) - 8\gamma^2 < 0 \quad (19)$$

Solving  $\Delta = 0$  we find that the wall jet of Fig 1 is unstable ( $\Delta < 0$ ) if

$$1.337 < kD < 3.427 \quad (20)$$

In other words, the inviscid wall jet is likely to acquire a waviness described by wavelengths in the range

$$1.833 < \frac{\lambda}{D} < 4.701 \quad (21)$$

The conclusion that an inviscid wall jet of thickness  $D$  is unstable only in a certain range of disturbance wavelengths, agrees with earlier results concerning other inviscid flows. For example, Rayleigh<sup>5</sup> found that a free two-dimensional jet of triangular profile is unstable for wavelengths  $\lambda > 1.714D$ . Rayleigh also found<sup>5</sup> that a free shear layer of thickness  $D$  is unstable if  $\lambda > 4.914D$ . It is significant that for several different base flows, from the wall jet of Fig 1 to Rayleigh's free shear layer, the edges of the wavelength domains for inviscid instability are marked by wavelengths which scale with the flow thickness  $D$ . We feel that this scaling is important and, ultimately, responsible for the phenomenon of transition to turbulence<sup>6</sup>. This scaling is the basis for the transition criterion outlined next.

### Time scale criterion for transition

Each longitudinal length scale  $\lambda$  and the jet velocity  $U$  define a time scale:

$$t \sim \frac{\lambda}{U/2} \quad (22)$$

This time scale is the period of the jet fluctuation as seen by an observer positioned on the vertical wall. Note that  $U/2$  is, in an order of magnitude sense, the wave velocity relative to a fixed spot on the wall.

Thus, the fluctuation time of the wall jet as an inviscid stream is:

$$t \geq t_{\min} = \frac{\lambda_{\min}}{U/2} \quad (23)$$

where, according to Eq (21):

$$\lambda_{\min} = 1.833D \quad (24)$$

In conclusion,  $t_{\min} \sim D$ ; this proportionality appears as a straight line in Fig 2, showing that an inviscid wall jet of thickness  $D$  can become unstable within a time interval  $t > t_{\min}$ .

The issue of whether or not the wall jet will become unstable is decided by examining the 'inviscid' of the flow. Inviscid or viscosity is a flow property, not a fluid property. If the wall jet tends to fluctuate (wave), then jet fluid will tend to make contact with the solid wall and the adjacent semi-infinite fluid reservoir intermittently, at time intervals  $t > t_{\min}$ . The wall jet, as a flow, remains inviscid if during each interval  $t$  it cannot learn by viscous diffusion of the presence of a restraining ambient. The characteristic time of viscous penetration ( $t_v$ ) from the wall and from the outer edge of the jet to the jet centreline (over a distance  $D/2$ ) is given by the solution to Stokes' first problem<sup>7</sup>:

$$\frac{D/2}{2\sqrt{\nu t_v}} \sim 1 \quad (25)$$

or:

$$t_v \sim \frac{D^2}{16\nu} \quad (26)$$

Locally, no jet will remain inviscid forever. Fig 2 shows that if the fluctuation time exceeds the viscous

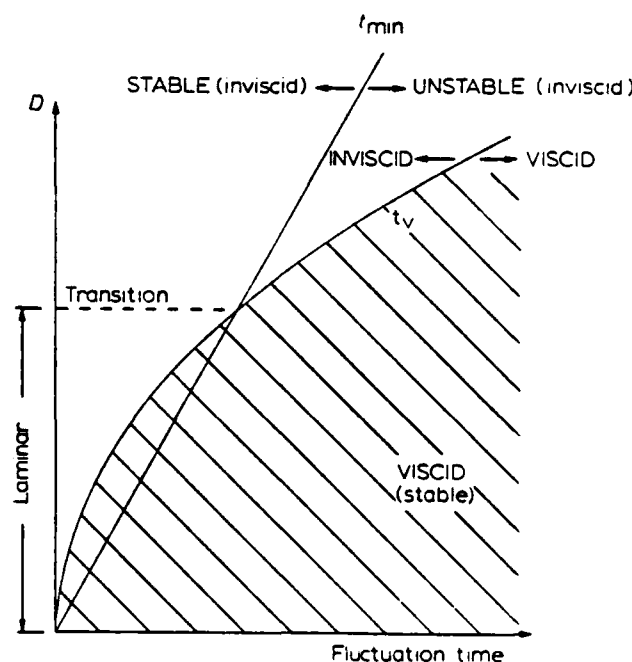


Fig 2 Internal competition between two characteristic times, the minimum period for inviscid instability ( $t_{\min}$ ) and the viscous communication time ( $t_v$ )

communication time  $t_v$ , the jet will remain laminar because it will continue to be restrained viscously by its ambient.

The instability predicted by so many hydrodynamic stability studies is therefore possible only if  $t_v$  exceeds  $t_{min}$ . In Fig 2, this condition corresponds to the intersection of the  $t_{min} \sim D$  line with the  $t_v \sim D^2$  line:

$$t_{min} = t_v \quad (27)$$

The phenomenon of transition to non-laminar flow appears to be governed by the time criterion:

$$O(N_B) = 1 \quad (28)$$

where:

$$N_B = \frac{t_v}{t_{min}} = \frac{DU}{58\nu} \quad (29)$$

The object of the remaining presentation is to test the  $N_B \sim 1$  criterion against the voluminous experimental record available on transition in natural convection along a vertical heated wall. Note at this point that the  $N_B \sim 1$  criterion is equivalent to  $Re \sim 58 \gg 1$ , where the Reynolds number  $Re$  is based on the local  $U$ ,  $D$  scales of the buoyant wall jet. Experimentally (as described later) it is found that the transition corresponds to a  $Re$  constant considerably greater than unity ( $Re \sim 10^2$ ). The contribution of the time scale argument that led to Eq (29) is to predict a transition  $Re$  much greater than unity; unlike the present arguments, classical scaling arguments regarding the relative size of viscous and inertial terms in the Navier-Stokes equations or in the Orr-Sommerfeld equation reveal  $Re \sim 1$  as a critical dimensionless parameter.

It is also worth noting that, theoretically, the same transition criterion ( $N_B \sim 1$ , or  $Re \sim 10^2$ ) is recommended by the buckling (meandering) property of inviscid streams<sup>9</sup>. This coincidence arises because the buckling wavelength of a two-dimensional inviscid jet<sup>8</sup>,  $\lambda_B = \pi\sqrt{3}D = 1.81D$ , is practically the same as the minimum wavelength for inviscid instability,  $\lambda_{min} = 1.83D$ . It has been shown<sup>8</sup> that the  $N_B \sim 1$  criterion anticipates correctly the transition to turbulence in free jet and wake flow.

### Scale analysis of natural convection along a vertical heated wall

To be able to apply the time-scale criterion, a theoretical understanding of the two wall jet scales ( $U$ ,  $D$ ) is essential. Consider the flow near a vertical wall, driven by the temperature difference  $\Delta T$  between wall and fluid reservoir. In general, the flow thickness ( $D$ ) will differ from the thickness of the fluid layer heated by the wall<sup>9</sup> ( $\delta_T$ ). The boundary layer-approximated equations governing the conservation of mass, momentum and energy in the system shown in Fig 3 are<sup>10</sup>:

$$\frac{\partial u}{\partial x} + \frac{\partial v}{\partial y} = 0 \quad (30)$$

$$u \frac{\partial u}{\partial x} + v \frac{\partial u}{\partial y} = \nu \frac{\partial^2 u}{\partial y^2} + g\beta(T - T_\infty) \quad (31)$$

$$u \frac{\partial T}{\partial x} + v \frac{\partial T}{\partial y} = \alpha \frac{\partial^2 T}{\partial y^2} \quad (32)$$

where  $x$ ,  $y$ ,  $u$ ,  $v$ ,  $T$ ,  $\nu$ ,  $g$ ,  $\beta$  and  $\alpha$  are the co-ordinates, velocity components, temperature, kinematic viscosity, gravitational acceleration in the negative  $x$  direction, coefficient of thermal expansion and thermal diffusivity, respectively.

Let  $\delta_T$  be the thermal boundary layer thickness, ie the slender fluid region in which the wall heating effect is felt. In this region, the heat conducted horizontally from the wall into the fluid, represented by the scale  $\alpha \Delta T / \delta_T^2$  from the energy equation (Eq (32)), is converted into enthalpy flow in the vertical direction,  $u \Delta T / H$ . Thus, the balance between conduction and convection in the layer of thickness  $\delta_T$  requires the following equivalence between the corresponding scales:

$$\frac{u \Delta T}{H} \sim \alpha \frac{\Delta T}{\delta_T^2} \quad (33)$$

or:

$$u \sim \alpha H / \delta_T^2 \quad (34)$$

The momentum equation (31) accounts for the competition between three forces: inertia, friction and buoyancy. The scales of these forces are, in order:

$$\frac{u^2}{H}, \quad \nu \frac{u}{\delta_T^2}, \quad g\beta \Delta T \quad (35)$$

Assuming first that the effect of inertia is negligible, and that Eq (31) is a balance between buoyancy and friction, we write:

$$\nu \frac{u}{\delta_T^2} \sim g\beta \Delta T \quad (36)$$

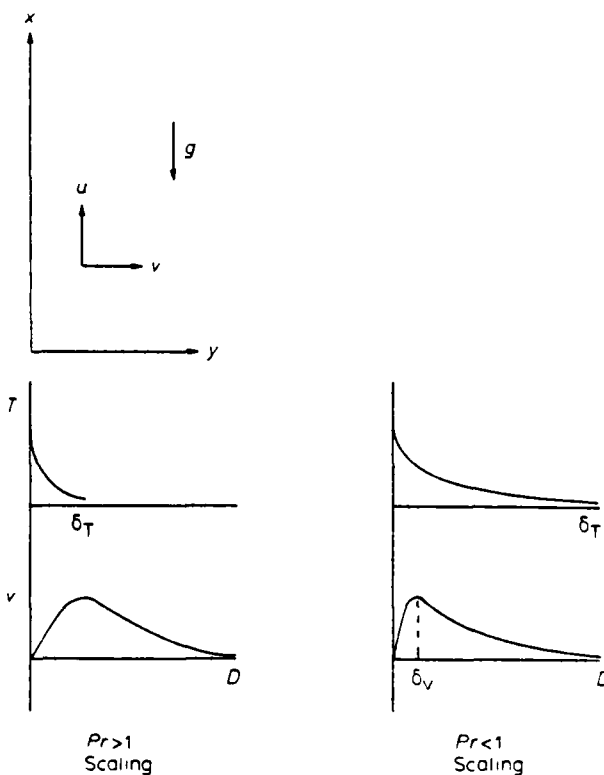


Fig 3 Relative sizes of thermal and velocity boundary layers for high and low  $Pr$  fluids

Using Eq (34) we find that, in a  $\delta_T$  layer dominated by a balance between buoyancy and friction, the scales are:

$$\begin{aligned}\delta_T &\sim H Ra_H^{-1/4} \\ u &\sim \alpha Ra_H^{1/2} / H\end{aligned}\quad (37)$$

The Rayleigh number based on vertical length scale  $H$ ,  $Ra_H$ , is defined as

$$Ra_H = \frac{g\beta \Delta T H^3}{\alpha \nu} \quad (38)$$

With the same assumptions that led to the scales above (Eq (37)), the negligibly small ratio inertia/friction, or inertia/buoyancy, requires

$$\frac{u^2/H}{u/\delta_T^2} \sim \frac{1}{Pr} \ll 1 \quad (39)$$

In conclusion, the scales are valid in high Prandtl number fluids ( $\nu/\alpha \gg 1$ ): as shown on the left side of Fig 3,  $Pr \gg 1$  fluids develop an additional length scale  $D$ , which is the thickness of the wall jet referred to in the time criterion for transition (Eqs (28, 29)). The  $D$  scale follows from the momentum equation scales (Eq (35)). Outside the thermal boundary layer the fluid is isothermal, hence, the buoyancy force is negligible relative to both inertia and friction. The equivalence of inertia and friction scales in the layer of thickness  $D$ :

$$\frac{u^2}{H} \sim \nu \frac{u}{D^2} \quad (40)$$

in conjunction with scales (37) yields:

$$D \sim Pr^{1/2} \delta_T \sim H Pr^{1/2} Ra_H^{-1/4} \quad (41)$$

for  $Pr \gg 1$ . The size of the wall jet relative to the thermal boundary layer is shown schematically in Fig 3. The  $D$  scale (Eq (41)), will be used later in the application of the transition criterion.

It remains to establish the  $u$ ,  $\delta_T$  and  $D$  scales prevailing in the case where the momentum equation represents a balance between buoyancy and inertia in the layer of thickness  $\delta_T$  (note that the  $Pr \gg 1$  scales (37) and (41) are based on a friction ~ buoyancy balance in the  $\delta_T$  layer). Writing:

$$\frac{u^2}{H} \sim g\beta \Delta T \quad (42)$$

and using Eq (34) yields:

$$\begin{aligned}\delta_T &\sim H (Ra_H Pr)^{-1/4} \\ u &\sim \alpha (Ra_H Pr)^{1/2} / H\end{aligned}\quad (43)$$

The inertia ~ buoyancy balance governs the  $\delta_T$  layer, except in a layer  $\delta_v$  immediately adjacent to the wall where the vertical velocity  $v$  obeys the no-slip condition. In the  $\delta_v$  layer friction is an important effect, hence:

$$\nu \frac{u}{\delta_v^2} \sim g\beta \Delta T \quad (44)$$

Combining this result with the  $u$  scale given by Eq (43) yields:

$$\delta_v \sim H Ra_H^{-1/4} Pr^{1/4} \sim \delta_T Pr^{1/2} \quad (45)$$

The relative magnitude of the  $\delta_T$  and  $\delta_v$  scales is shown in the right half of Fig 3. Thus, we draw two important conclusions: that the flow scales (43, 45) which follow from a balance between inertia and buoyancy in the  $\delta_T$  layer correspond to low Prandtl number fluids; and that the thickness of the wall jet in this case is the thickness of the entire layer heated by the wall,

$$D \sim \delta_T \sim H (Ra_H Pr)^{-1/4} \quad (46)$$

for  $Pr \ll 1$ . In what follows we shall rely on the above dimensions to translate the time-scale criterion (28, 29) into the terminology in which the phenomenon of transition has been recorded by previous studies of natural convection.

### Transition along a vertical heated wall

A relatively wide selection of experimental observations on the beginning of transition along an isothermal wall was compiled already by Mahajan and Gebhart<sup>11</sup>. Table 1 reproduces this compilation and shows the number  $G$  above which the buoyant wall jet was noticed to become nonlaminar. The number  $G$  is defined as:

$$G = 4^{3/4} \left( \frac{g\beta \Delta T H^3}{\nu^2} \right)^{1/4}$$

in other words:

$$G = 4^{3/4} Ra_H^{1/4} Pr^{-1/4} \quad (47)$$

The time criterion (28, 29) can be rewritten in terms of  $G$ , by using scales (37, 41) for  $Pr > 1$  fluids; taking  $U \sim u$  we have:

$$N_B = \frac{DU}{58\nu} \sim \frac{1}{58} Ra_H^{1/4} Pr^{-1/2} \sim \frac{G}{164 Pr^{1/4}} \quad (48)$$

Table 1 shows the  $N_B$  value corresponding to each experimental report: in all cases  $O(N_B) = 1$ , which is the same as the time criterion for transition. In conclusion, the experimental data on transition along isothermal walls supports the theoretical argument that the transition phenomenon is marked by the equivalence of time scales  $t_{min} \sim t_c$ .

Table 2 is a compilation of transition observations made using a vertical wall with constant heat

**Table 1 Experimental observations on beginning of transition along a vertical isothermal wall**

	$Pr$	$G$	$N_B$
Warner and Arpaci <sup>12</sup>	0.72	466	3.08
Colak-Antic <sup>13</sup>	0.72	572	3.79
Cheesewright <sup>14</sup>	0.72	600	3.97
Regnier and Kaplan <sup>15</sup>	0.72	622	4.12
	0.77	460-547	2.99-3.56
	0.77	645-702	4.20-4.57
	0.77	541	3.52
	0.77	605	3.94
	0.77	378	2.46
Eckert and Soehngen <sup>16</sup>	0.72	400	2.65
Hugot et al <sup>17</sup>	0.7	724	4.83
	0.7	665	4.43
Szewczyk <sup>18</sup>	6.7	534	2.02

flux  $q''$ . The observations have been catalogued in terms of  $Pr$  and the number  $G^*$  defined<sup>11</sup> as:

$$G^* = 5^{4.5} \left( \frac{g\beta q'' H^4}{k\nu^2} \right)^{1.5} \quad (49)$$

In order to obtain the relationship between  $N_B$  and  $G^*$ , we make the observation that for  $Pr > 1$  fluids the thermal boundary layer thickness and vertical velocity scale<sup>23</sup> as:

$$\delta_T \sim H \left( \frac{g\beta q'' H^4}{k\nu\alpha} \right)^{-1/5} \quad (50)$$

$$u \sim \frac{\alpha H}{\delta_T^2} \quad (51)$$

Substituting  $D \sim \delta_T Pr^{1/2}$  and  $U \sim u$  into Eq (29) yields:

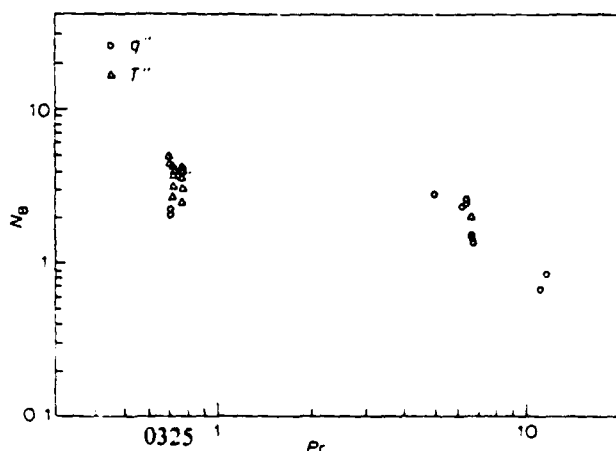
$$N_B \sim \frac{G^*}{210 Pr^{1/10}} \quad (52)$$

The  $N_B$  values corresponding to the experimental observations are listed in the last column of Table 2. Once again, the measured  $N_B$  number is of order one, in agreement with the theoretical criterion.

Fig 4 summarizes Tables 1 and 2. The experimental observations on transition fall consistently in the  $O(N_B) = 1$  domain in the Prandtl number range 0.7–11.4.

**Table 2** Experimental observations on beginning of transition along a wall with constant heat flux

	$Pr$	$G$	$N_B$
Mahajan and Gebhart <sup>11</sup>	0.71	388–620	2.05–3.27
	0.71	400–650	2.11–3.43
Jaluria and Gebhart <sup>19</sup>	6.7	504–802	1.36–2.16
	6.7	563–802	1.52–2.16
Godaux and Gebhart <sup>20</sup>	6.7	528–979	1.42–2.63
Vliet and Liu <sup>21</sup>	6.2	855	2.36
	6.4	955	2.61
	6.4	900	2.46
	5.05	960	2.81
Lock and Trotter <sup>22</sup>	11.0	293	0.68
	11.4	368	0.84

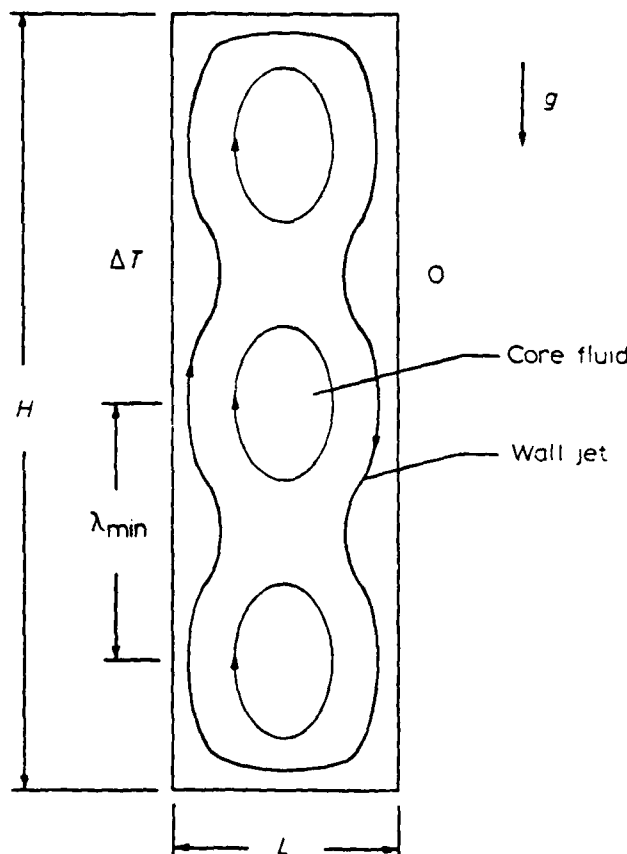


**Fig 4** Variation of time ratio  $N_B$  with  $Pr$

## Transition in enclosures heated from the side

In the preceding section we saw that the experimental observations on transition accumulated over the past three decades support the idea that the fluctuation (waving) time  $t_{min}$  matches the time of viscous diffusion across the wall jet. Now, by focusing on enclosures heated from the side, we have the opportunity to actually see the incipient waviness of the two wall jets during transition. The visualisation of the wall jet wavelength  $\lambda$  is made possible by the slow motion of the 'core'<sup>24</sup>, i.e. the motion of the cavity fluid sandwiched between the two fast-moving wall jets. It has been discovered experimentally<sup>25</sup> that in a characteristic Rayleigh number range the core fluid engages in a cellular motion of the type shown schematically in Fig 5. A large number of experimental and numerical studies have confirmed this phenomenon, especially the fact that the number of core cells increases as the Rayleigh number increases. Table 3 shows a representative sample of experimental and numerical observations.

In view of the theoretical discussion presented earlier, it is reasonable to regard the cellular structure of the slow-moving core as the reflection (the fingerprint) of the waviness acquired by the wall jets during transition. Thus, the cell-to-cell distance visible in



**Fig 5** Representation of buoyancy induced flow in a cavity of large aspect ratio with one wall heated, the other cooled, and the top and bottom insulated

published photographs<sup>25-29</sup> can be interpreted as the wavelength  $\lambda_{min}$  of the wall jet. The distance we measured from each photograph is listed as  $(H/\lambda_{min})_{experimental}$  in Table 3.

Fig 6 shows the relationship between the measured  $H/\lambda_{min}$  and  $Ra_H$ . The wavelength  $\lambda_{min}$  decreases as the Rayleigh number increases. However, the data supplied by an individual experiment (at constant  $Pr$ ) show very clearly the existence of a proportionality of the type:

$$\frac{H}{\lambda_{min}} \sim Ra_H^{1/4} \quad (53)$$

Theoretically, such a proportionality is to be expected because  $\lambda_{min} \sim D$  and  $D \sim H Ra^{-1/4}$  (Eqs 41 and 46). Thus the core flow data of Table 3 and Fig 6 reconfirm the theoretical result that at transition the jet wavelength always scales with the jet thickness.

The theoretical scale of  $H/\lambda_{min}$  can be calculated by writing  $\lambda_{min} = 1.833D$ , and by using Eqs (41, 46) to evaluate the scale of  $D$ . Thus we obtain:

$$\left(\frac{H}{\lambda_{min}}\right)_{theory} \sim \frac{Ra_H^{1/4}}{1.833 Pr^{1/2}} \quad (54)$$

for  $Pr \gg 1$ , and:

$$\left(\frac{H}{\lambda_{min}}\right)_{theory} \sim \frac{Ra_H^{1/4} Pr^{1/4}}{1.833} \quad (55)$$

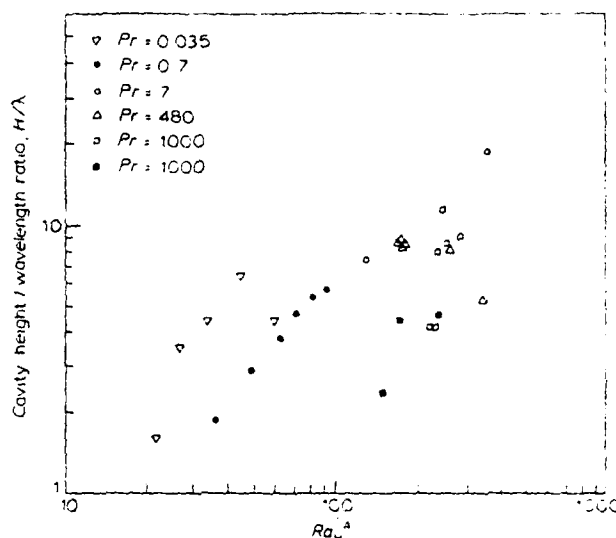


Fig 6 Variation of  $H/\lambda$  with  $Ra_H^{1/4}$

for  $Pr \ll 1$ . The theoretical order of magnitude of  $H/\lambda_{min}$  is also listed in Table 3. Finally, the ratio  $(\lambda_{min})_{exp}/(\lambda_{min})_{theory}$  was calculated and plotted in Fig 7. It is clear that the measured cell-to-cell distance,  $(\lambda_{min})_{exp}$ , has the same scale as the theoretical  $\lambda_{min}$ .

Table 3 Experimental and numerical observations on transition to turbulence in enclosures heated from the side

	$Pr$	$Ra_H$	$H/L$	$H/\lambda_{min}$	
				Experimental	Theoretical
Jones <sup>26</sup>	0.035	$2.5 \times 10^5$	10	1.61	5.28
	0.035	$5.0 \times 10^5$	10	3.49	6.27
	0.035	$1.0 \times 10^6$	10	4.36	7.46
	0.035	$4.0 \times 10^6$	20	6.45	10.55
	0.035	$1.1 \times 10^7$	20	4.42	10.59
Lee and Korpela <sup>27</sup>	0.7	$1.8 \times 10^6$	5.0	1.87	18.28
	0.7	$6.0 \times 10^6$	7.5	2.81	24.7
	0.7	$1.4 \times 10^7$	10.0	3.73	30.52
	0.7	$2.8 \times 10^7$	12.5	4.65	36.30
	0.7	$4.8 \times 10^7$	15.0	5.37	41.54
	0.7	$7.6 \times 10^7$	17.5	5.67	46.59
	0.7	$1.1 \times 10^8$	20.0	7.46	51.10
Elder <sup>25</sup>	7	$1.7 \times 10^{10}$	9.1	18.90	74.46
Seki et al <sup>28</sup>	480	$9.5 \times 10^8$	30	8.60	4.37
	480	$9.5 \times 10^8$	6	8.80	4.37
	480	$1.0 \times 10^9$	15	8.39	4.43
	480	$5.0 \times 10^9$	15	8.40	6.62
	480	$1.5 \times 10^{10}$	15	5.40	8.71
Elder <sup>25</sup>	1000	$2.5 \times 10^9$	19	4.17	3.86
	1000	$2.7 \times 10^9$	19	4.17	3.07
	1000	$3.4 \times 10^9$	19	7.98	4.17
	1000	$4.0 \times 10^9$	19	11.54	4.34
	1000	$4.7 \times 10^9$	19	8.57	4.52
	1000	$7.2 \times 10^9$	19	9.10	5.03
de Vahl Davis and Mallinson <sup>29</sup>	1000	$5.0 \times 10^8$	10	2.32	2.58
	1000	$9.5 \times 10^8$	10	4.36	3.03
	1000	$3.3 \times 10^9$	10	4.55	4.13

scale predicted by Eqs (54 and 55). The best agreement between  $(\lambda_{\min})_{\text{exp}}$  and  $(\lambda_{\min})_{\text{theory}}$  occurs at extreme Prandtl numbers ( $Pr = 0.035$  and  $Pr \geq 480$ ): This is a direct consequence of the fact that scales (54 and 55) are valid strictly in the limits  $Pr \rightarrow \infty$  and  $Pr \rightarrow 0$ , respectively. The in-between experimental results ( $Pr = 0.7$ ) are least accurately represented by either Eq (54) or Eq (55); nevertheless, the ratio  $(\lambda_{\min})_{\text{exp}}/(\lambda_{\min})_{\text{theory}}$  for  $Pr = 0.7$  is practically independent of  $Ra_H$ , stressing the earlier conclusion that  $\lambda_{\min}$  always scales with the thickness of the wall jet.

It is worth noting that the  $(\lambda_{\min}/H) \sim Ra_H^{-1/4}$  scaling law recommended by the time scale criterion (28) is consistent not only with the 27 experiments reviewed in Table 3 and Figs 6 and 7, but also with theoretical results known already from the hydrodynamic stability analysis of the vertical enclosure flow. Attention is drawn to Bergholz's comprehensive study of the flow stability in a vertical slot<sup>30</sup>. As 'base flow' for the stability analysis, Bergholz considered a counterflow velocity profile independent of altitude, as would be the case only in an infinitely tall cavity<sup>31</sup>. He then accounted for the finiteness of the cavity aspect ratio  $H/L$  by postulating the existence of a constant vertical temperature gradient through the slot,  $S$  [K/m]: note that in the vertical boundary layer regime, the thermal stratification  $S$  is of order  $\Delta T/H$ , where  $\Delta T$  is the temperature difference in the horizontal direction (Fig 5). By increasing the dimensionless stratification parameter  $\gamma = (\frac{1}{2} S(L/\Delta T) Ra_L)^{1/4}$ , Bergholz was able to make the base flow more jet-like, that is more like the vertical wall jets of Figs 1 and 3, which are known to prevail in vertical enclosures in the boundary layer regime<sup>24,25</sup>.

In Fig 7 of his study, Bergholz reported the critical wavenumber  $\alpha_c = 2\pi L/\lambda_c$  versus the stability parameter  $\gamma$  and the Prandtl number. One very interesting aspect of Fig 7 is that in the boundary layer limit ( $\gamma \gg 1$ ) and in the high Prandtl number limit  $Pr \rightarrow \infty$ , the wavenumber of travelling modes is proportional to  $\gamma$ :

$$\alpha_c \sim \gamma, \quad (56)$$

the proportionality constant being a number of order  $O(1)$  (in the same limits, the wavenumbers of the stationary modes are, numerically, not much different than those of the travelling modes, however, they do not appear to follow the line represented by Eq (56)).

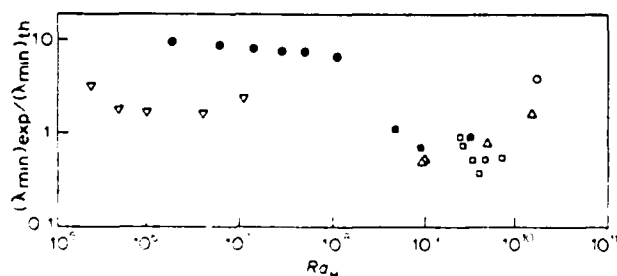


Fig 7 Experimental/theoretical inviscid wavelength ratio as a function of  $Ra$  and  $Pr$  ( $Pr$  notation as for Fig 6)

Noting the  $L$ -based definitions of both  $\alpha_c$  and  $\gamma$  employed by Bergholz<sup>30</sup>, it is easy to prove that the  $\alpha_c \sim \gamma$  scaling illustrated by Bergholz is actually:

$$\frac{H}{\lambda_c} \sim Ra_H^{1/4} \quad (57)$$

This scaling, predicted by the conventional stability theory<sup>30</sup> is the same as the scaling law (53) produced by a much more direct argument above.

The agreement between the present approach and conventional stability theory is illustrated further by the fact that  $\alpha_c$  reaches asymptotically a  $O(1)$  constant as  $\gamma$  approaches zero. This is shown by Fig 7 in Bergholz<sup>30</sup>, but is also predicted by the  $\lambda_{\min} \sim D$  scaling on which the present argument is based. Note that as  $\gamma$  decreases towards zero, the vertical jet thickness increases and so does the wavelength (Eq (56)); but this process cannot continue beyond the point where the jet thickness becomes of order  $L$  because, regardless of how small  $\gamma$  is, the slot of width  $L$  must house two jets in counterflow. According to the  $\lambda_{\min} \sim D$  scaling, both  $D$  and  $\lambda_{\min}$  must be of order  $L$  when  $\gamma < O(1)$ : this also means ' $\alpha_c \rightarrow O(1)$  constant as  $\gamma \rightarrow 0$ ', which is precisely the behaviour unveiled by classical stability analysis (travelling as well as stationary modes, Fig 7 of Ref 30).

Although the compatibility between the results of conventional stability theory and the scaling results based on the argument given earlier is relevant and interesting, one should not expect one theory to 'reproduce' the results of a different theory. Unlike stability theory, which is a mathematically precise approach, the present theoretical argument is approximate and based on the comparison of scales. This is why the success of the present argument should be measured in terms of its ability to predict the trends and orders of magnitude revealed by the many independent experiments collected in Tables 1-3.

## Concluding remarks

The published observations on transition to turbulence in natural convection were reviewed in order to test the validity of the time scale criterion (Fig 2) for transition  $O(N_B) = 1$  or  $O(Re) = 10^2$  formulated. It was found that laboratory observations and numerical simulations support the theoretical viewpoint that:

1. At transition, the wall jet exhibits a unique wavelength which always scales with the thickness of the jet.
2. Transition is marked by the equivalence of two time scales, both properties of the jet region of the flow, the minimum fluctuation period ( $t_{\min}$ ) and the time of viscous diffusion normal to the jet ( $t_v$ ). The empirical evidence on natural convection along vertical heated walls suggests that:
3. Transition along an isothermal wall is correctly anticipated by the criterion  $O(N_B) = 1$ , where  $N_B$  is given by Eq (48).
4. Transition along a vertical wall with uniform heat flux is correctly anticipated by the criterion  $O(N_B) = 1$ , where  $N_B$  is given by Eq (52).

5. The cellular flow exhibited by the core fluid in an enclosure is a reflection of the waviness of the two wall jets during transition. The cell size, or the wall jet wavelength, are correctly described by the scales shown in Eqs (54) and (55).

Finally, the theoretical argument leading to the  $O(N_R) = 1$  criterion provides a theoretical basis for the empirical notion that the transition Reynolds number is a flow constant considerably greater than unity.

## Acknowledgement

This research was sponsored by the US Office of Naval Research.

## References

1. Tani I. *Annual Review of Fluid Mechanics*, 1969, 1, 169-196
2. Reshotko E. Boundary-layer stability and transition. *Annual Review of Fluid Mechanics*, 1976, 8, 311-349
3. Gebhart B. Natural convection flow, instability and transition. *J. Heat Transfer*, 1969, 91, 293-309
4. Lamb H. *'Hydrodynamics'*, Dover, New York (1945), 670-671
5. Lord Rayleigh On the stability, or instability, of certain fluid motions. *Proceedings of the London Mathematical Society*, Vol XI, 57-70, 1880
6. Bejan A. Analytical prediction of turbulent heat transfer parameters, Report CUMER 83-4, Dec 1983, Dept. of Mechanical Eng., University of Colorado, Boulder
7. Schlichting H. *'Boundary Layer Theory'*, 4th ed., McGraw-Hill, New York, 1960, 72
8. Bejan A. On the buckling property of inviscid jets and the origin of turbulence. *Letters in Heat and Mass Transfer*, Vol. 8, 181-194, 1981
9. Patterson J. and Imberger J. Unsteady natural convection in a rectangular cavity. *J. Fluid Mechanics*, 1980, 100, 65-86
10. Gebhart B. *'Heat Transfer'*, 2nd ed., McGraw-Hill, New York, 1971, 331
11. Mahajan R. L. and Gebhart B. An experimental determination of transition limits in a vertical natural convection flow adjacent to a surface. *J. Fluid Mechanics*, 1979, 91, 131-154
12. Warner C. and Arpaci V. S. An experimental investigation of turbulent natural convection in air at low pressure along a vertical heated plate. *Int. J. Heat & Mass Transfer*, 1968, 11, 397-406
13. Colak-Antic P. Hitzdraht messungen des laminar-turbulenten Umschlags bei freier Konvektion. *Jahrbuch der WGLR*, 1964, 1972-1976
14. Cheesewright R. Turbulent natural convection from a vertical plane surface. *J. Heat Transfer*, 1968, 90, 1-8
15. Regnier G. M. and Kaplan C. Visualization of natural convection on a plane wall and in a vertical gap by differential interferometry. Transitional and turbulent regimes. *Proc. 1963 Heat Transfer Fluid Mech. Inst., Stanford University Press*, 94-110, 1963
16. Eckert E. R. G. and Soehngen E. Interferometric studies on the stability and transition to turbulence of a free-convection boundary layer. *Proc. Gen. Disc. Heat Transfer, London*, 321-323, 1951
17. Hugot, G., Jannot M. and Pirovano A. *Compte-rendu de Fin de Contrat DGST no. 69-01-773*, 1971
18. Szweczyk A. A. Stability and transition of the free convection layer along a vertical flat plate. *Int. J. Heat & Mass Transfer*, 1962, 5, 903-914
19. Jaluria Y. and Gebhart B. On transition mechanisms in vertical natural convection flow. *J. Fluid Mechanics*, 1974, 66, 309-337
20. Godaux R. and Gebhart B. An experimental study of the transition of natural convection flow adjacent to a vertical surface. *Int. J. Heat & Mass Transfer*, 1974, 17, 93-107
21. Vliet G. C. and Liu C. K. An experimental study of turbulent natural convection boundary layers. *J. Heat Transfer*, 1969, 91, 517-531
22. Lock G. S. and Trotter F. J. de B. Observations on the structure of a turbulent free convection boundary layer. *Int. J. Heat & Mass Transfer*, 1968, 11, 1225-1232
23. Sparrow E. M. Laminar free convection on a vertical plate with prescribed nonuniform wall heat flux or prescribed nonuniform wall temperature. *NACA TN3508*, July 1955, 18
24. Gill A. E. The boundary layer regime for convection in a rectangular cavity. *J. Fluid Mechanics*, 1966, 26, 515-536
25. Elder J. W. Laminar convection in a vertical slot. *J. Fluid Mechanics*, 1965, 23, 77-98
26. Jones I. P. *Numerical Predictions from the IOTA2 Code for Natural Convection in Vertical Cavities*, paper presented at the Winter Annual Meeting of the ASME, Nov. 1982, Phoenix, Arizona
27. Lee Y. and Korpela S. A. Multicellular natural convection in a vertical slot. *J. Fluid Mechanics*, 1983, 126, 91-121
28. Seki N., Fukusako S. and Inaba H. Visual observations of natural convective flow in a narrow vertical cavity. *J. Fluid Mechanics*, 1978, 84, Part 4, 695-704
29. de Vahl Davis G. and Mallinson G. D. A note on natural convection in a vertical slot. *J. Fluid Mechanics*, 1975, 72, Part 1, 57-93
30. Bergholz R. F. Instability of steady natural convection in a vertical fluid layer. *J. Fluid Mechanics*, 1978, 84, 743-765
31. Batchelor G. K. Heat transfer by free convection across a closed cavity between vertical boundaries at different temperatures. *Quarterly of Applied Mathematics*, 1954, 12, 209-233

## MECHANISM FOR TRANSITION TO TURBULENCE IN BUOYANT PLUME FLOW

SHIGEO KIMURA and ADRIAN BEJAN

Department of Mechanical Engineering, Campus Box 427,  
University of Colorado, Boulder, CO 80309, U.S.A.

(Received 21 July 1982 and in final form 25 January 1983)

**Abstract** This paper reports a theoretical and experimental study of the fundamental mechanism responsible for transition in natural convection plume flow. Theoretically, it is argued that the transition occurs when the time of viscous penetration normal to the plume becomes comparable with the minimum time period with which the plume can fluctuate as an unstable inviscid stream. It is also argued that at transition the plume wavelength must always scale with the local plume diameter. The experimental part of the study focused on transition in the axisymmetric air plume above a point heat source. Smoke visualization of the plume shape at transition led to extensive observations that support strongly the transition mechanism proposed theoretically. The transitional plume is seen to meander in a plane (two-dimensionally) and with a wavelength which scales with the plume diameter. If excited externally by many such wavelengths, the plume has the property to select the natural wavelength proposed theoretically. The equivalence between the present transition mechanism and the transition predicted by the buckling theory is discussed.

### NOMENCLATURE

$D$	local plume diameter [m]
$f$	disturbance frequency [ $s^{-1}$ ]
$g$	gravitational acceleration [ $m\ s^{-2}$ ]
$H$	loudspeaker height [m]
$k$	thermal conductivity [ $W\ m^{-1}\ K^{-1}$ ]
$N$	ratio between $t_v$ and $t_{min}$ ; same as buckling number $N_B$ [16, 21]
$Q$	heat input [W]
$t$	time [s]
$t_{min}$	minimum plume fluctuation time [s]
$t_v$	viscous communication time [s]
$U$	plume velocity [ $m\ s^{-1}$ ]
$x$	transition height [m]

### Greek symbols

$\alpha$	thermal diffusivity [ $m^2\ s^{-1}$ ]
$\beta$	thermal expansion coefficient [ $K^{-1}$ ]
$\lambda$	wavelength [m]
$\lambda_B$	buckling wavelength [m]
$\lambda_{min}$	minimum plume fluctuation wavelength [m]
$\nu$	kinematic viscosity [ $m^2\ s^{-1}$ ]

### Subscripts

$B$	buckling property
$0$	reference state

### 1. INTRODUCTION

THIS is a study of the fundamental mechanism which causes the transition to turbulence in buoyant plumes rising from a point heat source. The transition to turbulence is one of the most basic phenomena which is not yet fully understood. The importance of understanding this phenomenon is self-evident, considering the importance of predicting the ensuing turbulent motion of fluids. The transition phenomenon is particularly important in the field of heat transfer, environ-

mental engineering, atmospheric research, because turbulence is the most effective transport mechanism known to man.

The buoyant plume is one frequent type among the many occurrences of free-convection flows in engineering and other applications. In this paper we are specifically interested in the axisymmetric buoyant plume rising from a point heat source in a quiescent environment. Existing studies on such plumes and the plume transition phenomenon have been summarized by Gebhart [1], who showed that considerable effort has been devoted to this problem over the past few decades. For example, the laminar 2-dim. and axisymmetric plume has been studied by Yih [2, 3], and Brand and Lahey [4]. Probably the most thorough treatment of this problem is the numerical analysis by Fujii [5].

Experimental studies on the plane plume above the line source were reported by Brodowicz and Kierkus [6], Forstrom and Sparrow [7], and Schorr and Gebhart [8]. The latter two works are concerned with the plume behavior in the transition regime as well as in the laminar regime. Schorr and Gebhart observed by means of interferometric flow visualization a regular laminar 'swaying' motion at a large distance above a line heat source. This type of boundary layer swaying motion is amplified and eventually the flow becomes turbulent. Forstrom and Sparrow also observed the existence of swaying motion at a fixed point in space near transition, by means of a thermocouple placed midway between the mid-plane and the edge of the thermal boundary layer.

The theoretical research on transition in plume flow proceeded along the lines of hydrodynamic stability theory. For example, Pera and Gebhart [9] showed by integrating inviscid cases of the Orr-Sommerfeld type equation that the assumed 2-dim. plume base flow is less stable for the asymmetric mode than for the



symmetric one. A thorough study of buoyancy effect on hydrodynamic stability in the vertical round jet has been conducted by Mollendorf [10] who found that buoyancy strongly affects the stability of jets.

In the discussion of existing information on transition, the adopted theoretical view is rooted in the theory of hydrodynamic stability. This point of view consists of recognizing the existence of external disturbances of many wavelengths which, when superimposed on the laminar flow of interest, might render the flow unstable, thus triggering turbulence. The same comment applies to the existing experimental work on transition: this time the disturbances are introduced into the flow externally, for example, by using a loudspeaker. Thus, as we look back at the important advances made in this field of transition research, it is important to keep in mind that this research is not about flows alone, but about the response of certain flows to certain disturbances.


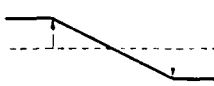
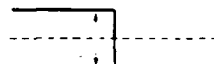
From the outset, it must be said that the point of view which stimulated the present study differs somewhat from the classical hydrodynamic stability approach. The difference lies in the fact that in this study 'transition' is viewed as an intrinsic property of the flow alone, i.e. a property which is not related to the nature or questionable presence of an external disturbance. It is shown in the next section that this intrinsic property stems from hydrodynamic stability results which have been known for one hundred years. However, it is apparent that the significance of these results *vis-à-vis* transition has not been emphasized until now.

## 2. THE MINIMUM WAVELENGTH FOR INVISCID FLOW INSTABILITY: TIME CRITERION FOR TRANSITION

The type of classical stability results which stimulated the present study is exhibited in Table 1. In a 1880 paper, Rayleigh [11] showed that an inviscid jet of triangular profile is unstable to disturbances whose wavelengths exceed a certain multiple of the jet thickness  $D$ . Rayleigh did not calculate explicitly the minimum wavelength of 'neutral' stability: his discussion focused primarily on another, longer wavelength ( $\approx 2\frac{1}{2}D$ ) for which an assumed disturbance exhibits the highest amplification rate ([11], p. 65). The minimum wavelength for instability,  $\lambda_{\min}$ , which results from Rayleigh's jet analysis is listed in row (a) of Table 1.

Similar results have been known from stability studies involving other basic flows. For example, Rayleigh considered also the free shear flow profile (b) and found instability for wavelengths greater than '5D' ([11], p. 63). Thus, for several velocity profiles of the base flow, the minimum wavelength for inviscid instability always scales with the transversal dimension of the flow. As shown in row (c) of Table 1, this scaling is consistent with another classical result, namely, the instability of a plane of velocity discontinuity to any wavelength [12]. In this case, the minimum wavelength is zero, i.e. of the same order as the shear layer thickness. The proportionality  $\lambda_{\min} \sim D$  is also encountered in the

Table 1. Minimum wavelength for instability in inviscid flow (after refs. [12-14])

Free jet		1.4 D
Free shear layer		4.34 D
Plane of velocity discontinuity		0

stability analysis of radially symmetric flows, for example, round jets [13] and annular shear layers [14].

The object of this study is the transition to turbulence in a buoyant plume. This flow is represented approximately by profile (a) in Table 1. The theoretical basis of the present research is the idea that the  $\lambda_{\min} \sim D$  scaling discussed in the preceding paragraphs is an intrinsic property of the inviscid flow, and that this property is responsible for transition. The mission of the experimental work outlined later in this paper is to verify the validity of this theoretical viewpoint. Below, a simple scaling argument is offered as a basis for the transition phenomenon, and as an analytical result to be verified by experiment.

Each longitudinal length scale  $\lambda (\geq \lambda_{\min})$  and the plume velocity  $U$  define a new time scale,

$$t \sim \frac{\lambda}{U/2} \quad (1)$$

This is the period in which the stream will fluctuate relative to the still environment. Note that  $U/2$  is the plume mean velocity which, from symmetry considerations, represents the order of magnitude of the velocity with which the  $\lambda$  wave rises. The same flow is unstable to an infinity of wavelengths  $\lambda > \lambda_{\min}$  [11], hence, the same flow can fluctuate with an infinity of periods

$$t \geq t_{\min} \sim \frac{\lambda_{\min}}{U/2} \quad (2)$$

However, since  $\lambda_{\min}$  is proportional to  $D$  (Table 1), the minimum fluctuation period  $t_{\min}$  is proportional to  $D$  also. The proportionality  $t_{\min} \sim D$  is shown as a straight line on Fig. 1, where  $D$  is plotted on the ordinate because in natural convection the plume becomes thicker with altitude. For any inviscid stream of thickness  $D$ , fluctuations with a period shorter than  $t_{\min}$  are stable.

The issue of whether the stream ( $U, D$ ) will become unstable is decided by examining the 'inviscid' of the flow. *Inviscid* or *viscid* is a *flow property*, not a *fluid property*. If the stream tends to fluctuate (wave), then plume fluid will tend to collide with the stagnant ambient intermittently, at time intervals  $t > t_{\min}$ . The plume stream remains inviscid if during each interval  $t$  it is not overcome by viscous effects, i.e. it does not learn

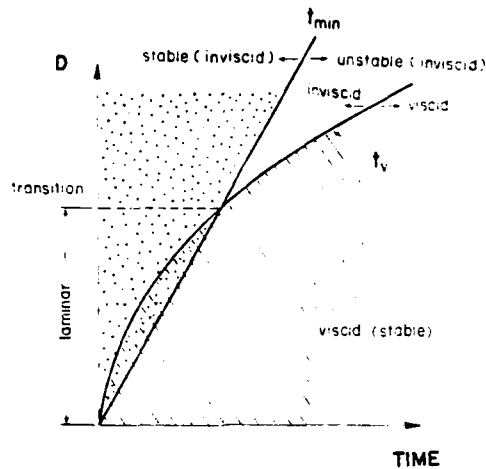


FIG. 1. The internal competition between the minimum period for inviscid instability ( $t_{min}$ ) and the viscous communication time ( $t_v$ ).

by viscous diffusion of the presence of a restraining ambient. The characteristic time of viscous penetration ( $t_v$ ) from the plume–ambient interface to the plume centerline (over a distance of order  $D/2$ ) is given by the classical solution to Stokes' first problem [15]

$$\frac{D/2}{2(\nu t_v)^{1/2}} \sim 1, \quad (3)$$

in other words,

$$t_v \sim \frac{D^2}{16\nu}. \quad (4)$$

Thus, at any level (height) in its development, no plume will remain inviscid forever. Figure 1 shows that if the fluctuation time exceeds the viscous penetration time  $t_v$ , the plume will remain laminar because its ambient will successfully continue to restrain it viscously.

The inviscid instability predicted by so many hydrodynamic stability studies (Table 1) is therefore possible only if  $t_v$  exceeds  $t_{min}$ . In Fig. 1, this condition corresponds to the intersection of the  $t_{min} \sim D$  line with the  $t_v \sim D^2$  parabola,

$$t_{min} \sim t_v. \quad (5)$$

The phenomenon of transition to non-laminar plume flow appears to be governed by the time criterion

$$O(N) = 1 \quad (6)$$

where

$$N = \frac{t_v}{t_{min}} \sim \frac{DU^2 v}{32(\lambda_{min} D)}. \quad (7)$$

Noting that  $\lambda_{min} D$  is a constant (Table 1), the  $O(N) = 1$  criterion is equivalent to stating that at transition the stream (local) Reynolds number  $DU^2 v$  is a certain (critical) constant considerably greater than unity. Thus, approximating  $\lambda_{min} \approx 1.714D$  from Table 1, the

transition criterion (6) becomes

$$\frac{DU^2 v}{v} > 55, \quad (8)$$

for transition to non-laminar flow.

The object of the following experimental study is to test the validity of the  $t_{min} \sim t_v$  scaling, as mechanism for transition in plume flow. It is worth noting from the outset that the theoretical time criterion is already compatible with two earlier conclusions regarding transition:

(1) Experimentally, it is a universal conclusion that transition is associated with a characteristic Reynolds constant considerably greater than unity.

(2) Theoretically, the same transition criterion is recommended by the buckling theory of inviscid jets [16], where  $\lambda_{min}$  is replaced by the buckling wavelength of the stream,  $\lambda_{kb} = (\pi/2)D = 1.57D$ .

An important distinction must be made, however, between the above theoretical criterion [equations (6)–(8)] and the universally accepted fact that the transition is characterized by  $DU^2 v = \text{constant}$ . To begin with, the notion of a 'critical' Reynolds number of transition is of purely empirical origin. On the theoretical side, the linearized (small-disturbance) equations of hydrodynamic stability theory can easily be subjected to scale analysis to show that the Reynolds number is indeed an important dimensionless parameter: comparing the Reynolds number with unity (one), we can say whether or not the viscous terms can be neglected in the stability analysis. Note, however, that this scaling argument is not about 'transition', rather, it is about the simplification of stability analysis. Also on the theoretical side, the Reynolds number appears in the solution to the complete Orr–Sommerfeld equation: however, unlike in criterion (8), the stability-derived transition Reynolds number is not a constant. (It is a function of the wavelength of each postulated disturbance.)

In view of this discussion, the time criterion (6)–(8) seems to provide for the first time a hydrodynamic stability scaling basis for "the Reynolds number = a constant considerably greater than unity" as transition criterion. The experimental observations summarized later in Section 6 show that at transition the order of  $UD^2 v$  is  $10^2$ , in agreement with the time criterion (6)–(8).

### 3. EXPERIMENTAL APPARATUS AND PROCEDURE

The experiments focused on a controlled version of the cigarette smoke phenomenon with which we are all familiar. As shown in Fig. 2, the apparatus consisted of a man-size, airtight, Plexiglas enclosure which was needed to isolate the experiments from ambient air currents present in the laboratory. Two adjacent side-walls and the top and bottom walls of the chamber were constructed of wood. The remaining two adjacent side walls were made of Plexiglas in order to permit the lighting and viewing of the smoke plume.

An axisymmetric air plume was generated above a small heat source placed in the center of the box.

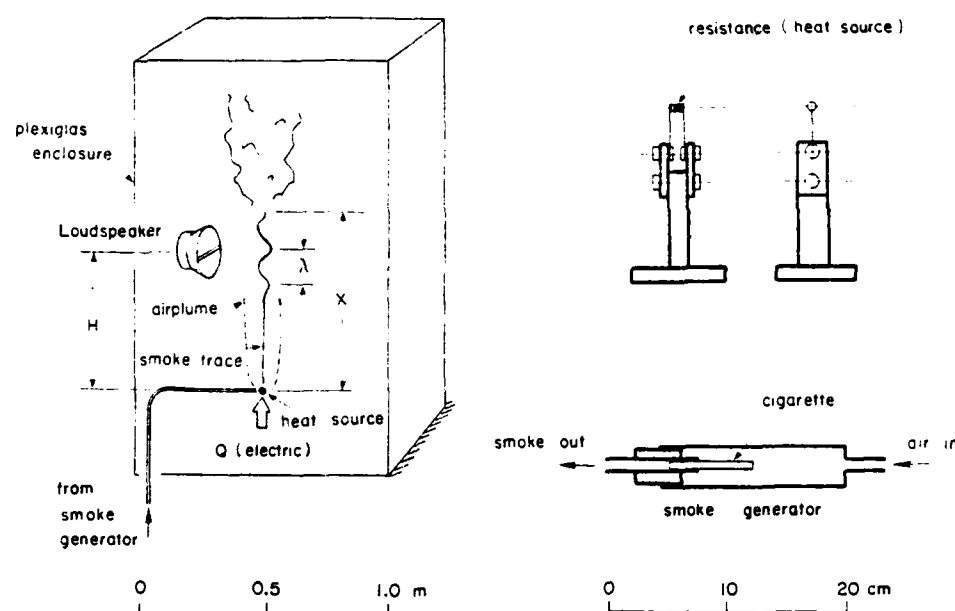


FIG. 2. Schematic of the experimental apparatus.

approximately 45 cm from the bottom. The heat source was constructed in the form of a nichrome resistance coil, as shown in Fig. 2. Electric power in the 0–50 W range was measured and dissipated in the coil: most of this energy was released into the buoyant air plume. (The estimated radiation heat loss was less than 6% at 22 W and less than 20% at 55 W.)

Cigarette smoke was generated in an external device constructed after a design described by Bradshaw [17]. The smoke was released directly beneath the nichrome coil very slowly so that it did not affect the air plume. This simple flow visualization technique worked very well, and the plume shape visualized by the smoke trace was photographed.

The experiments were designed to test the validity of the  $t_{\min} \sim t_v$  scaling during transition. For a certain (reference) power dissipated in the coil,  $Q_0$ , the plume shape was photographed 3–6 times. The photographs showed statistically the existence of a characteristic height  $x_0$  and wavelength  $\lambda_0$  for the beginning of transition (Fig. 2). The power setting  $Q$  was changed during the course of experiments and these changes reflected in the measured  $x$  and  $\lambda$ . The object of the experiment was to discover the dimensionless functions

$$\frac{x}{x_0} = \text{function} \left( \frac{Q}{Q_0} \right), \quad (9)$$

$$\frac{\lambda}{\lambda_0} = \text{function} \left( \frac{Q}{Q_0} \right). \quad (10)$$

The experimental findings were then compared with the theoretical functions recommended by the  $t_{\min} \sim t_v$  scaling. The theoretical functions  $x/x_0$  and  $\lambda/\lambda_0$  can be obtained by recalling that the diameter and velocity of a

laminar plume above a point heat source scale as [18]

$$D \sim Q^{-1/4} x^{1/2} \left( \frac{zg\beta}{v^3 k} \right)^{-1/4}, \quad (11)$$

$$U \sim Q^{1/2} \left( \frac{zg\beta}{vk} \right)^{1/2}. \quad (12)$$

At transition we expect  $\lambda \sim D$  and  $t_{\min} \sim t_v$  [or  $DU/v \sim \text{constant}$ , equation (8)], hence, the theoretical functions to be tested are

$$\frac{x}{x_0} = \left( \frac{Q}{Q_0} \right)^{-1/2}, \quad (13)$$

$$\frac{\lambda}{\lambda_0} = \left( \frac{Q}{Q_0} \right)^{-1/2}. \quad (14)$$

Note that the scaling represented by equations (11) and (12) is valid for Prandtl numbers of  $O(1)$  or greater.

#### 4. RESULTS

In the first series of observations the plume was photographed in the absence of any external noise which might act as a trigger for transition. The measured transition heights and wavelengths are shown in Fig. 3: both  $x$  and  $\lambda$  decrease as the energy content of the plume  $Q$  increases. The variation of  $\lambda/\lambda_0$  vs  $Q/Q_0$  parallels the theoretical curve, equation (14) but the measured transition heights are consistently greater than the theoretical levels. Comparing this first series of observations with the theoretical expectations [equations (13) and (14)], we conclude that in the absence of external triggers the transition wavelength scales with the plume diameter, however, the transition is delayed

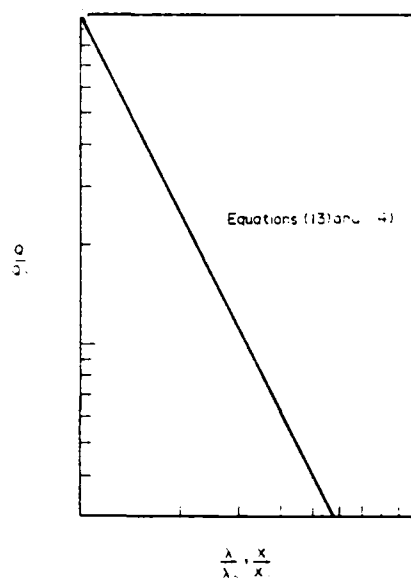


FIG. 3. The transition height and the wavelength as a function of heat input, in the absence of external noise.  $\circ$ ,  $x/x_0$ , transition height.  $\Delta$ ,  $\lambda/\lambda_0$ , wavelength.

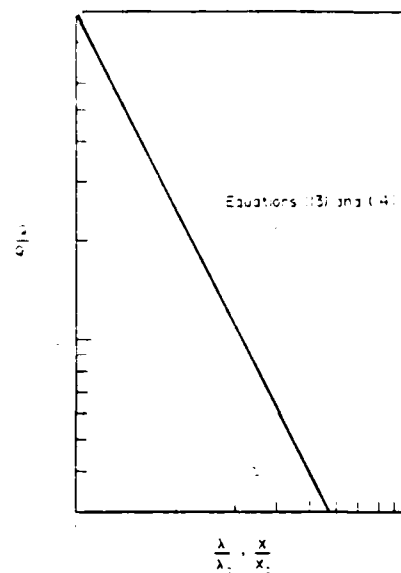


FIG. 4. The transition height and wavelength as a function of heat input. The enclosure wall was tapped by a finger.  $\circ$ ,  $x/x_0$ , transition height.  $\Delta$ ,  $\lambda/\lambda_0$ , wavelength.  $Q_0 = 55$  W,  $x_0 = 0.25$  m,  $\lambda_0 = 0.04$  m.

and occurs further downstream from the theoretical level.

Considerably more conclusive results were obtained by photographing the plume shapes immediately after tapping the enclosure once, with a finger. This sort of noise served to introduce disturbances of many (unspecified) wavelengths and amplitudes into the air plume flow. Figure 4 shows the measured variation of  $\lambda/\lambda_0$  and  $x/x_0$  with  $Q/Q_0$ ; the agreement with theory is very good in a relatively wide range of power settings  $Q/Q_0$ . It appears that the stream has the natural ability to filter [19] out of the disturbance spectrum the natural wavelength of transition. The measurements indicate that the natural wavelength scales with the plume diameter (because  $\lambda \sim Q^{-1/2}$ ). These results validate the theoretical basis for adopting  $t_{\min} \sim t_v$  as transition criterion (Section 2).

The repeatability of the above observations is demonstrated by the sequence of photographs presented as Figs. 5(a)–(c). These three photographs belong to the same plume, as the plume strength  $Q$  was held constant ( $Q = 31.1$  W). The transition wavelength and height are recorded instantly by means of the vertical scale mounted next to the plume, at the same distance from the camera [note that Figs. 5(a)–(c) were taken at different times, using different focusing lengths]. The photographs show clearly that, given a plume, the transition to non-laminar flow is characterized by a characteristic wavelength  $\lambda$  and a characteristic height  $x$ .

The relationship between  $\lambda$ ,  $x$  and  $Q$  at transition (Fig. 4) is illustrated in Figs. 6(a) and (b). From Fig. 6(a) to Fig. 6(b) the source strength  $Q$  increases by almost a factor of 2; correspondingly both  $\lambda$  and  $x$  decrease by a

factor of the order of  $1/\sqrt{2}$  predicted theoretically. Again, transition is characterized by a well-defined 'meandering' shape with a unique wavelength and at a unique height.

An important aspect of the plume shape during transition is its two-dimensionality. We investigated this aspect by conducting a separate series of experiments in which the plume was photographed simultaneously from two angles, from the front and from the side. The side-view was visible in a tall mirror placed vertically near the plume, at a  $45^\circ$  angle with respect to the camera-plume direction. The mirror view appears on the LHS of each of the photographs shown in Figs. 7(a)–(c).

By tapping the side of the box once, we had absolutely no control on the plane in which the plume would choose to meander during transition. Thus, we had to take many photographs in order to come across a few cases where the plane of deformation happened to be nearly perpendicular to the camera-plume direction. Two such cases are exhibited in Figs. 7(a) and (b): plume deformation during transition is clearly in one plane. Figure 7(c) shows one of the many cases in which the plane of deformation did not coincide with either the camera-plume direction or with the direction perpendicular to the camera-plume line: regardless of the misalignment, Fig. 7(c) shows that the elbows of the sinusoidal shape are all in the same plane.

The 2-dim., planar, character of the plume deformation during transition [Figs. 7(a)–(c)] is an important conclusion: it contradicts the hydrodynamic stability assumption [13] that the initial deformation (disturbance) in free jet flow is helical (3-dim.).

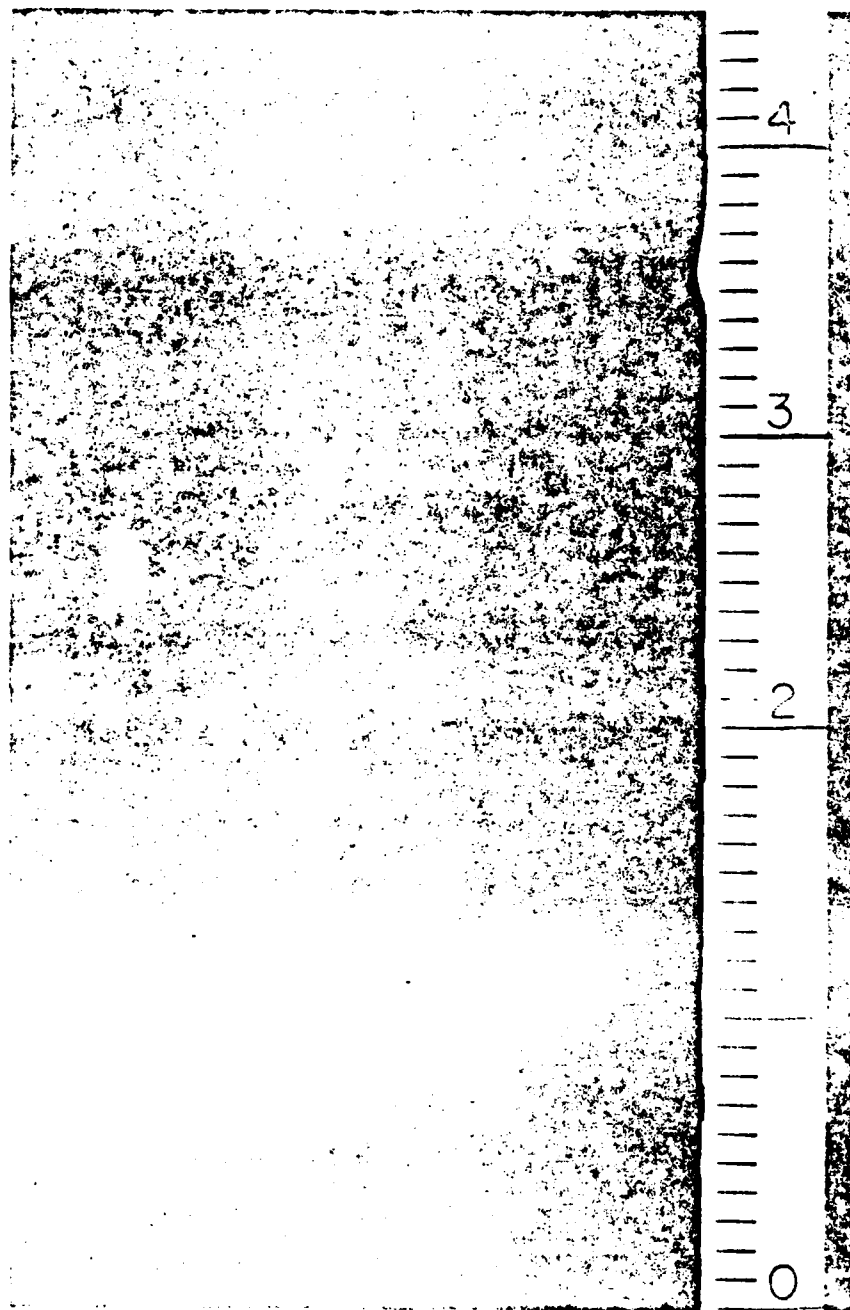


Fig. 5a

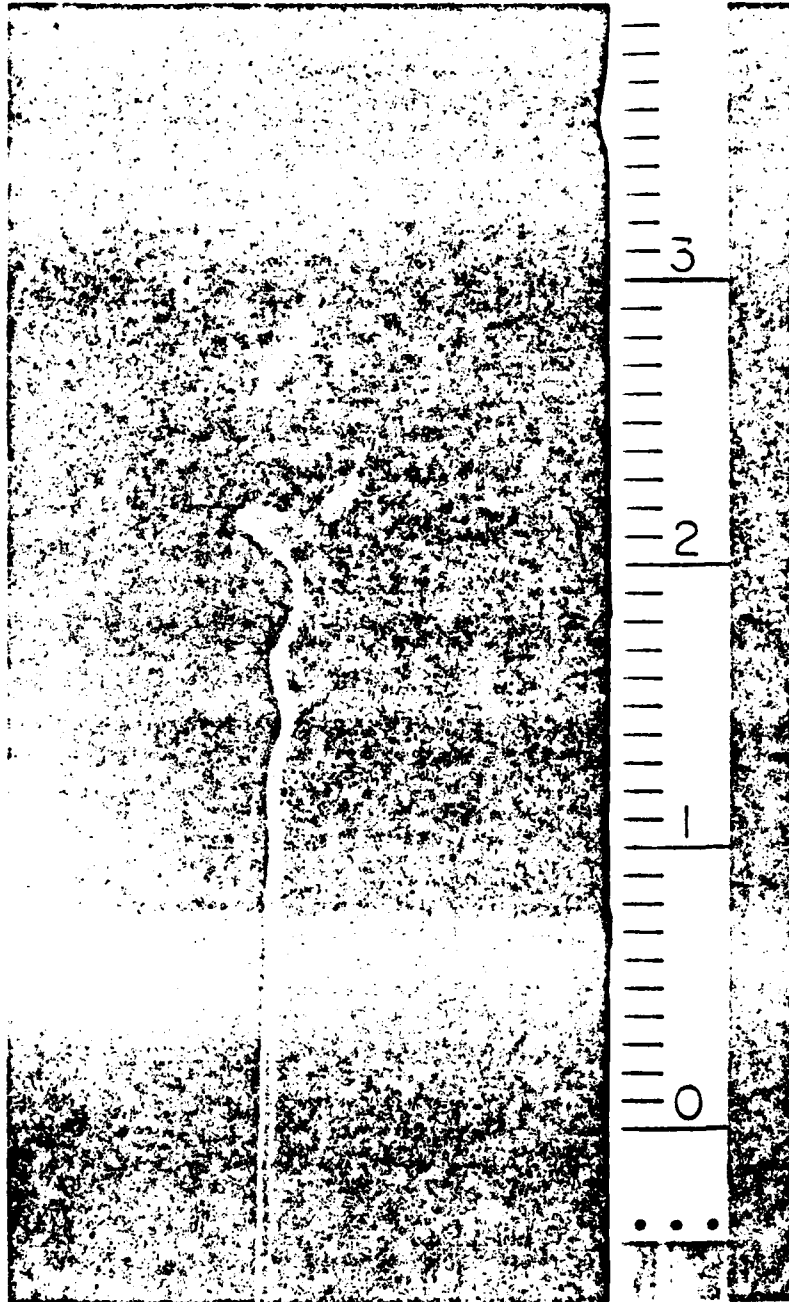


FIG. 5(b)

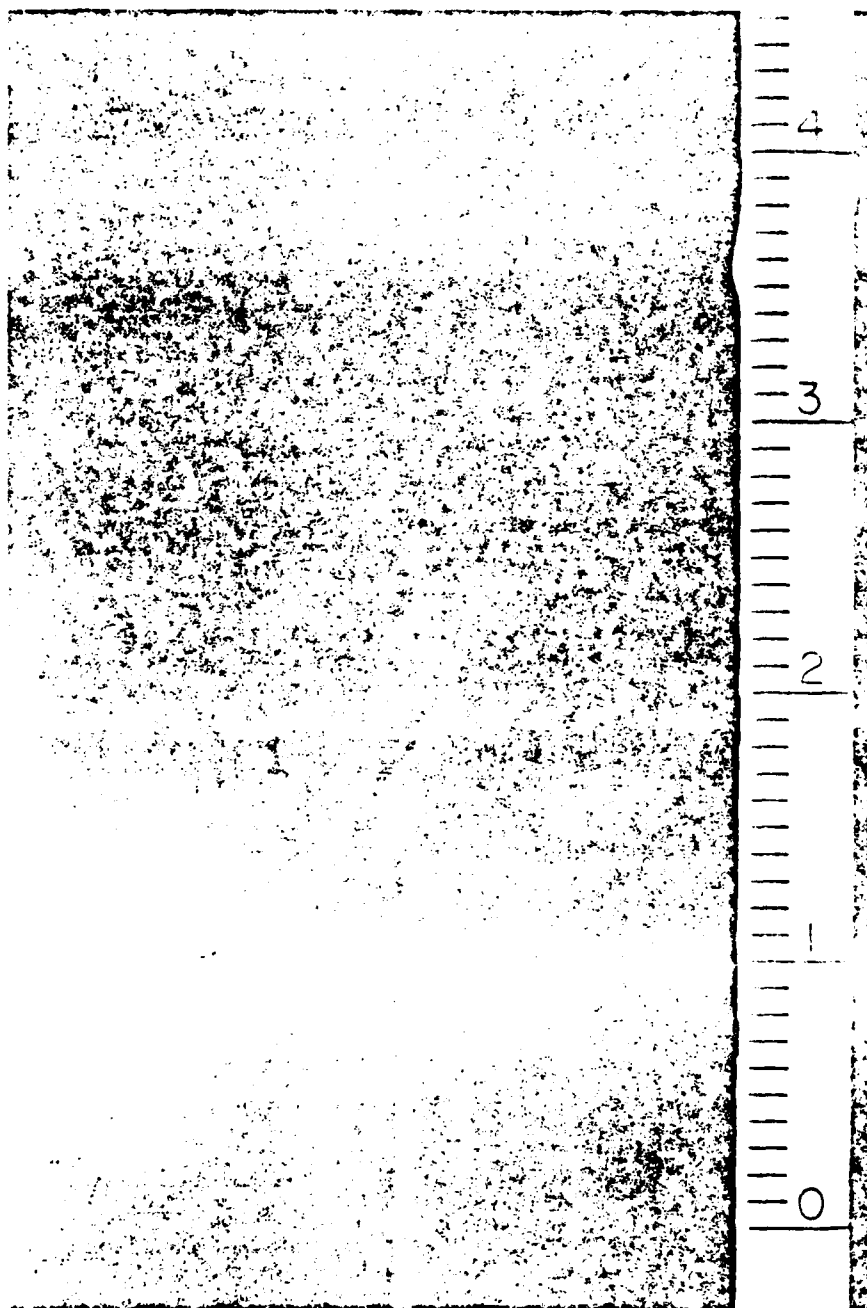


FIG. 5(a)

FIG. 5. Photographs showing the transitional shape of the same plume ( $Q^* = 31.1 W$ ).

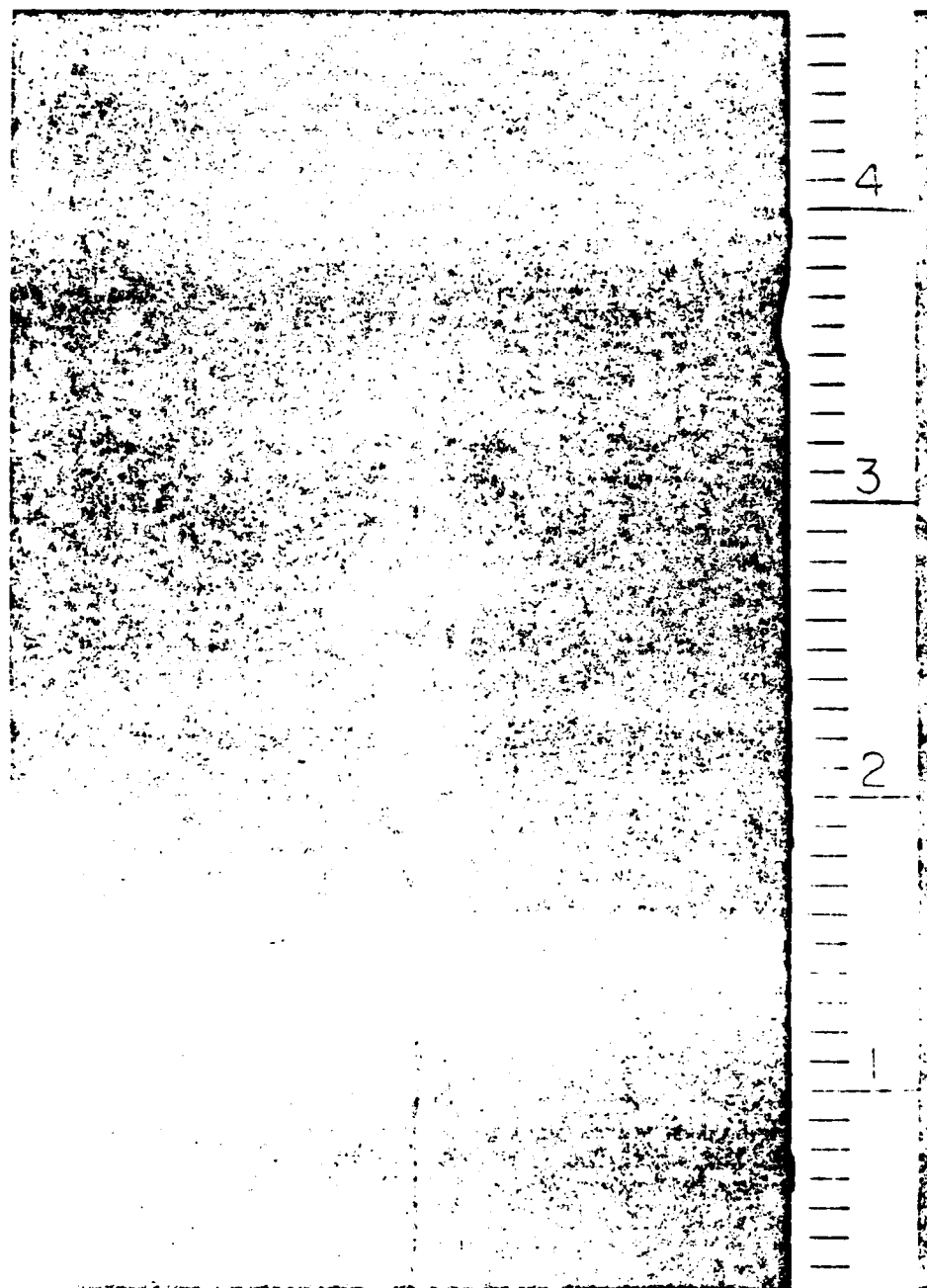


FIG. 9(a)  $Q = 21.9$  W



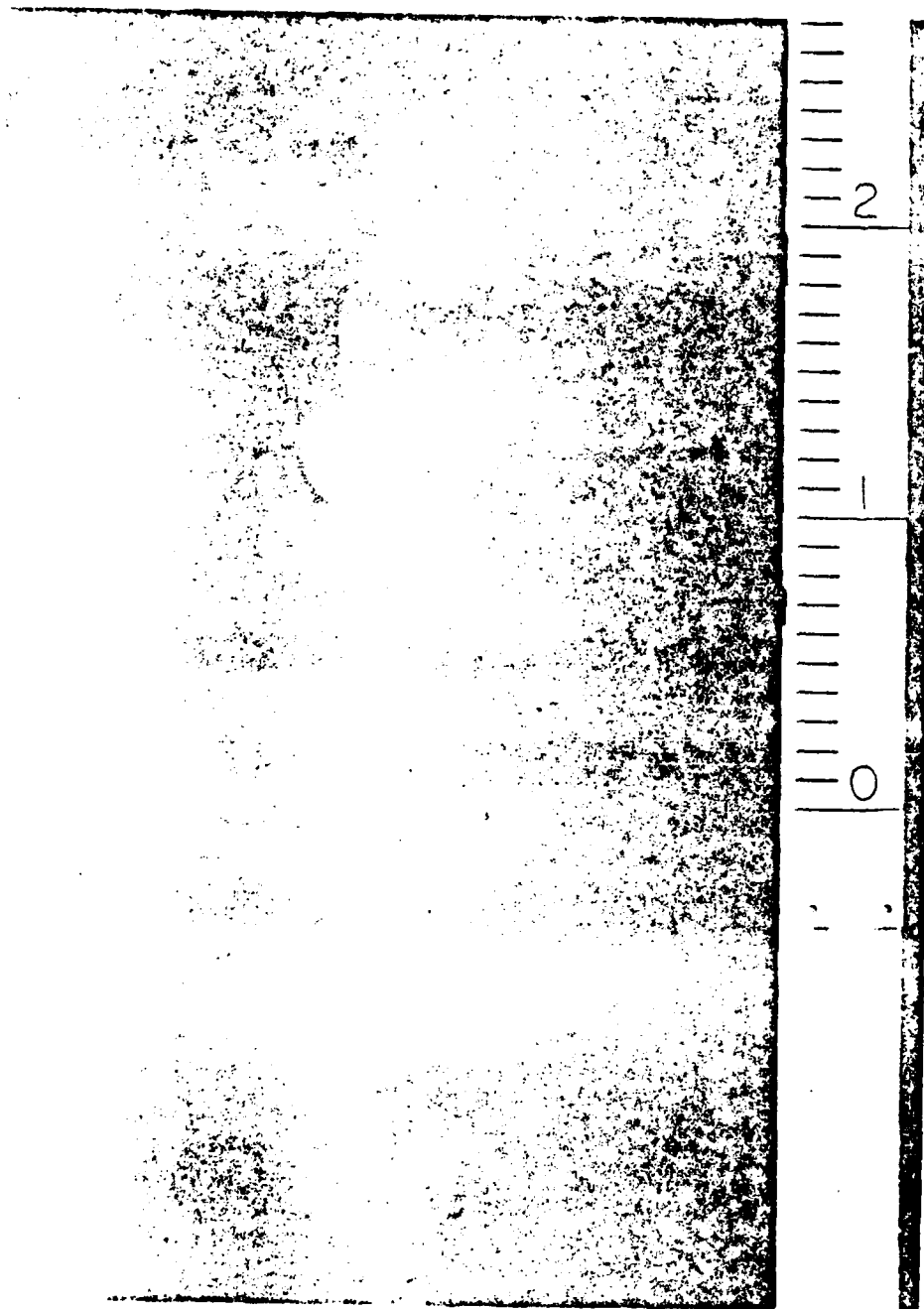
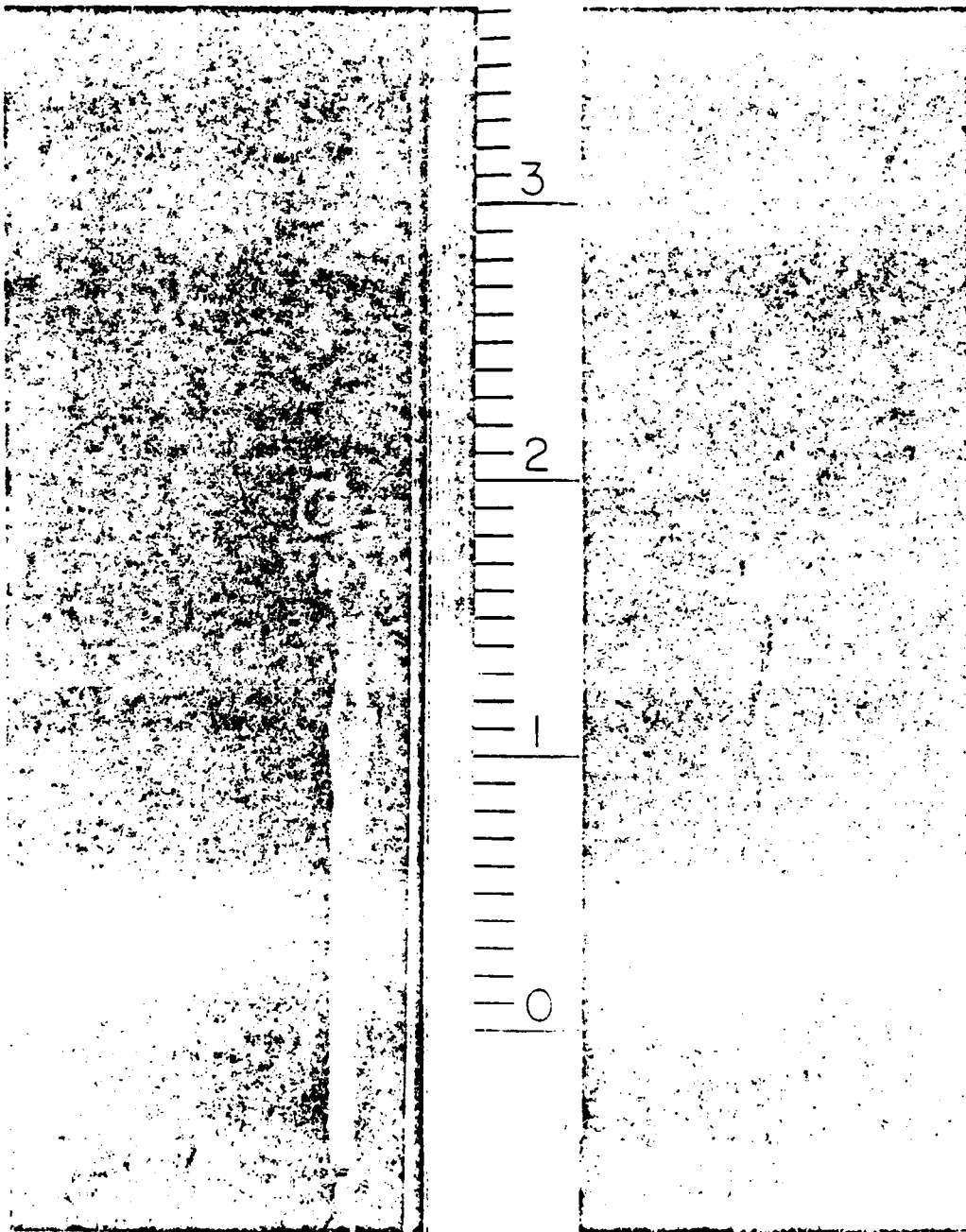
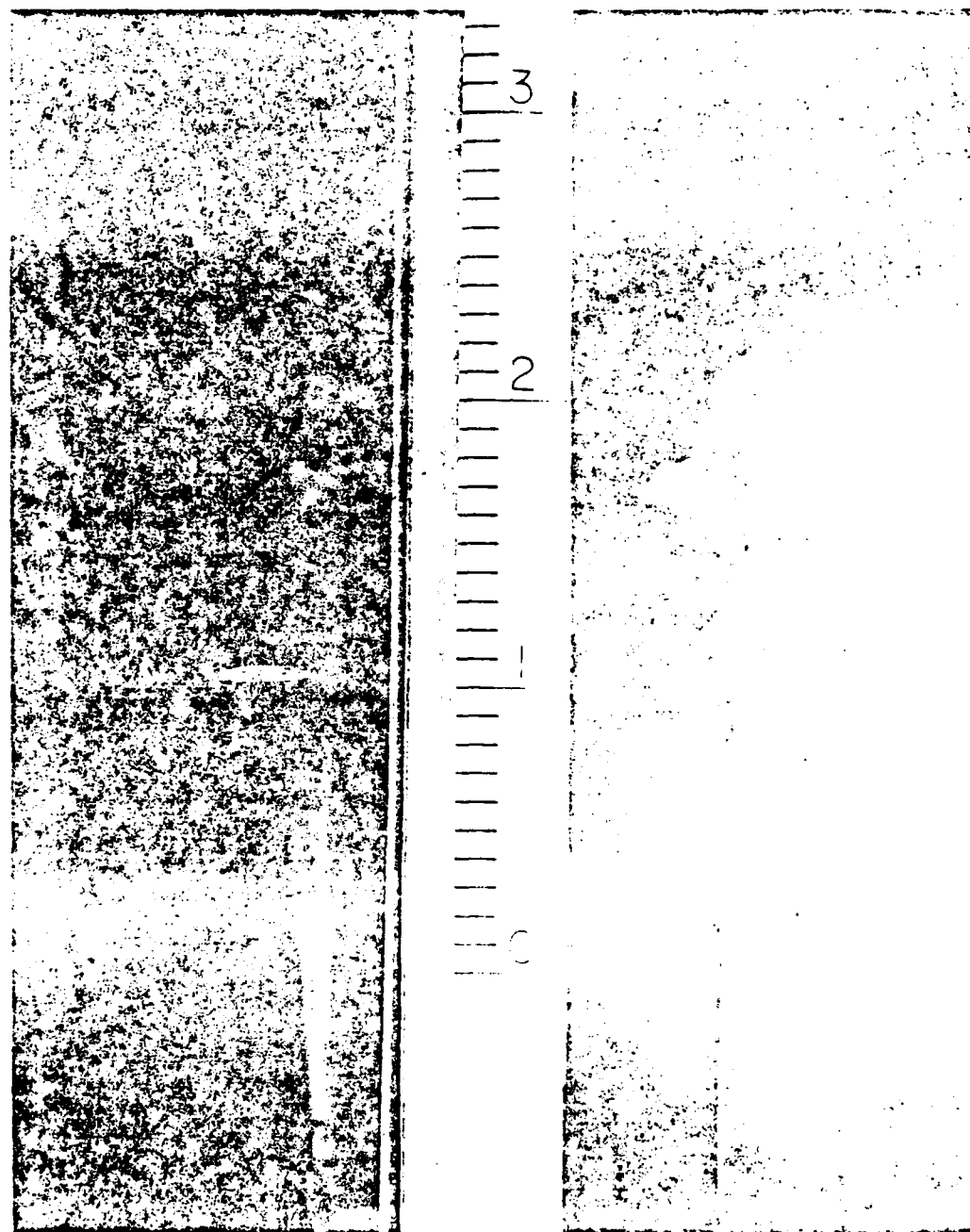
FIG. 6(b).  $Q = 38.9 W$ 

FIG. 6. The decrease in wavelength and transition height as the plume strength increases.

FIG. 7(a)  $Q = 5.7W$

FIG. 7(b)  $Q = 5.1$  W

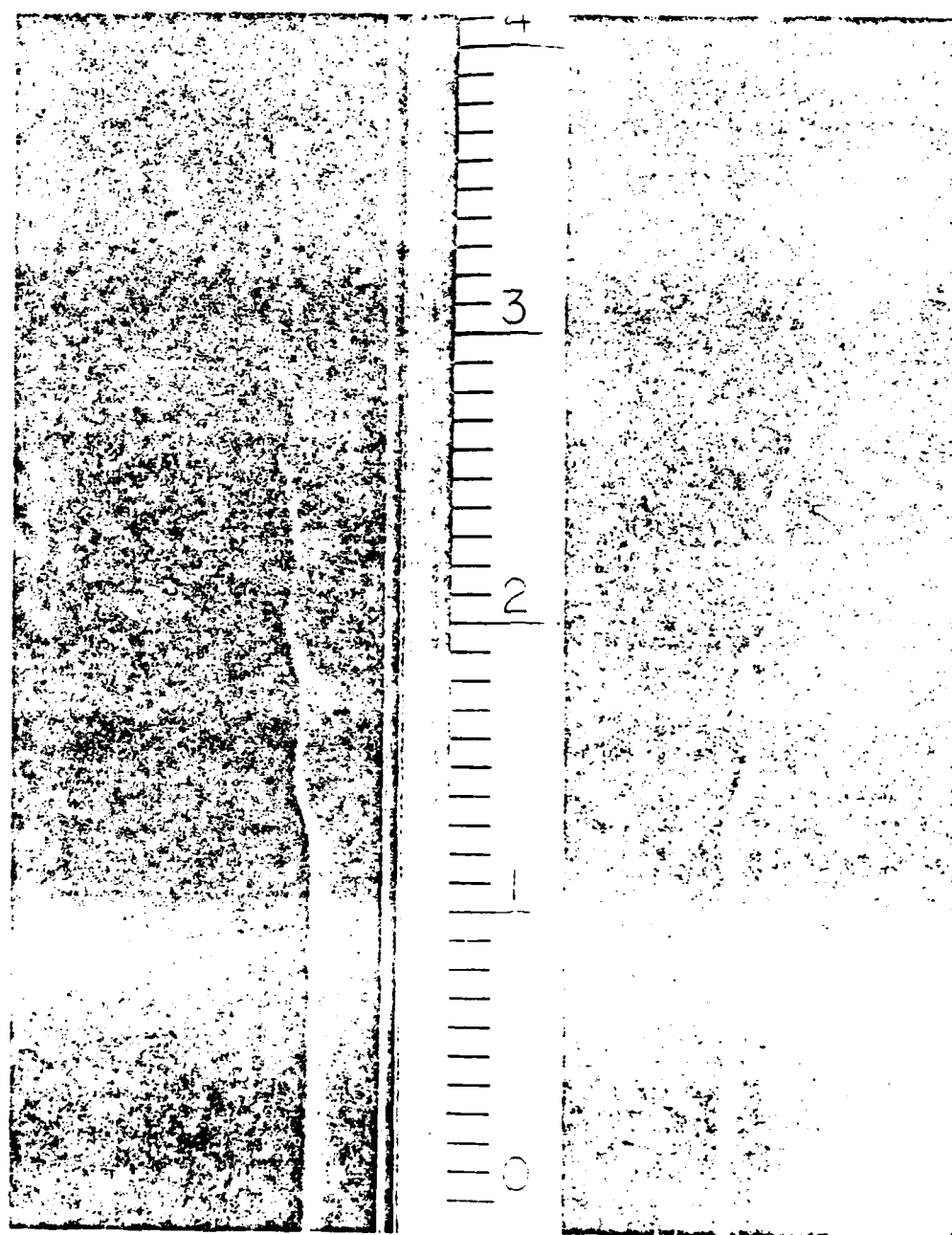


FIG. 7. (a)  $Q = 12$  W.

FIG. 7. The two-dimensionality of the mean axial plume shape during transition.

### 5. TRANSITION IN A HARMONICALLY-FORCED PLUME

The series of experiments described in the preceding section yielded convincing evidence that the transition phenomenon is the result of the scale properties discussed in Section 2. These properties were studied further in another series of experiments where, unlike in Section 4, the location, intensity and frequency of the 'trigger' disturbance were controlled. The disturbance was generated by a loudspeaker suspended at a certain height,  $H$ , next to the plume (Fig. 2). The face of the loudspeaker was covered by a wooden panel with a  $3 \text{ mm} \times 200 \text{ mm}$  horizontal slit cut into it. Thus, we were able to harmonically force only a narrow section of the rising plume, at a height determined by the position of the loudspeaker. The intensity of the harmonic forcing (relative to a reference intensity) was monitored by measuring the power needed to drive the loudspeaker.

The experiments were conducted in a manner similar to what led to the observations summarized in Fig. 4. For a fixed heat source strength  $Q$ , the plume was disturbed (shaken) at certain frequencies  $f$  of the same amplitude (the loudspeaker frequency varied, however, the maximum travel of its cone was held constant). It was observed that the transition height  $x$  depended strongly on the frequency of harmonic excitation,  $f$ . It was found that there exists a characteristic frequency  $f$  such that the transition takes place at a minimum height: frequencies higher and lower than this characteristic value triggered transition at higher altitudes. These 'resonance' characteristics have been studied extensively (visually and photographically [20]) and are amply documented in Figs. 8(a)–(f). In Figs. 8(a)–(c) the loudspeaker was held at a level 4.5 cm above the heat source, while in Figs. 8(d)–(f) the loudspeaker height was 13 cm.

The minimum transition height and the corresponding wavelength were found to decrease with the increasing heat source strength  $Q$ . These observations are summarized in Fig. 9: they are nearly identical to the results of Fig. 4 obtained by tapping the enclosure once with a finger. Thus, the plume resonates, hence, is deformed most effectively when it is harmonically forced at its natural frequency, with a wavelength that scales with the plume thickness at the transition height.

The acoustic excitation provided by the loudspeaker introduces two more variables in the experiment, the loudspeaker height and the excitation amplitude. In Figs. 8(a)–(f) we show the effect of disturbance amplitude. Increasing the disturbance has the effect of precipitating the transition, i.e. the effect of decreasing the transition height. Raising the loudspeaker from 5.4 cm to 13 cm above the plume origin, has the effect of placing the transition further downstream

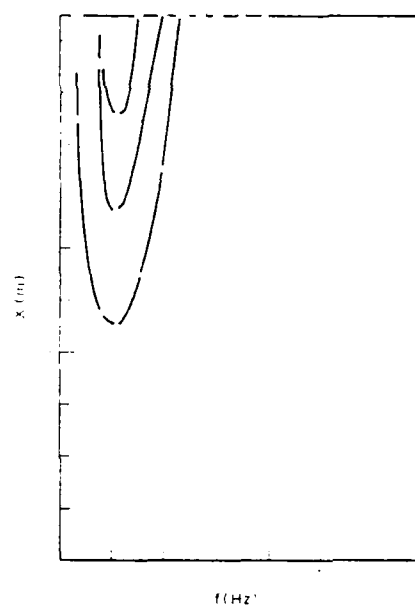


Fig. 8(a).  $Q = 1.03 \text{ W}$ ,  $H = 0.045 \text{ m}$ .  $\circ$  7V;  $\triangle$  4V;  $\square$  2V.

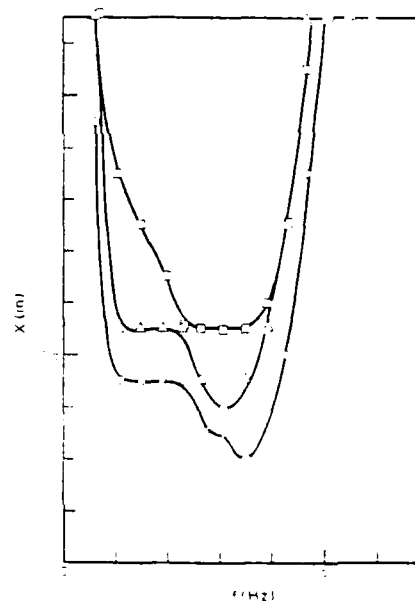


Fig. 8(b).  $Q = 4.13 \text{ W}$ ,  $H = 0.045 \text{ m}$ .  $\circ$  7V;  $\triangle$  4V;  $\square$  2V.

the characteristic wavelength and transition height (the same measurements are listed in Tables 2 and 3). It is evident that at transition the height  $x$  is proportional to the characteristic wavelength  $\lambda$ , in fact,

$$x \sim 10\lambda \quad (35)$$

is an order-of-magnitude fit for the data plotted in Fig. 10. The measured proportionality between  $x$  and  $\lambda$  at transition is anticipated correctly by the scaling

### 6. TRANSITION REYNOLDS NUMBER GREATER THAN UNITY

As a summary to the preceding series of observations, Fig. 10 shows the actual linear dimensions of

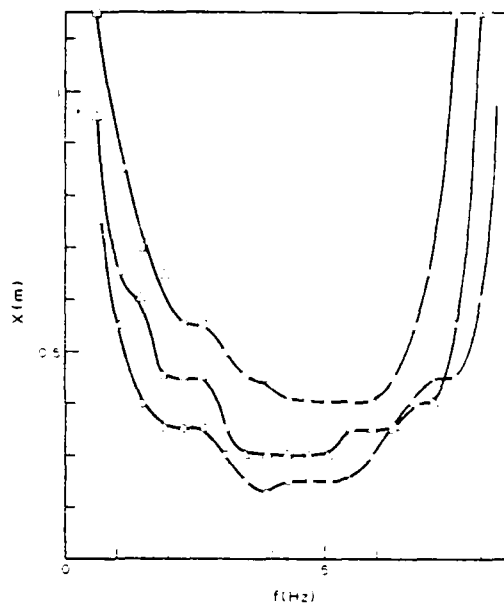


FIG. 8(c).  $Q = 8.44$  W,  $H = 0.045$  m.  $\circ$  4V;  $\triangle$  2V;  $\square$  1V.

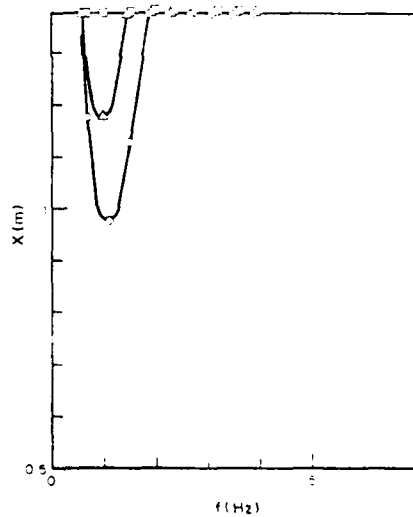


FIG. 8(d).  $Q = 1.02$  W,  $H = 0.13$  m.  $\circ$  8V;  $\triangle$  4V;  $\square$  2V.

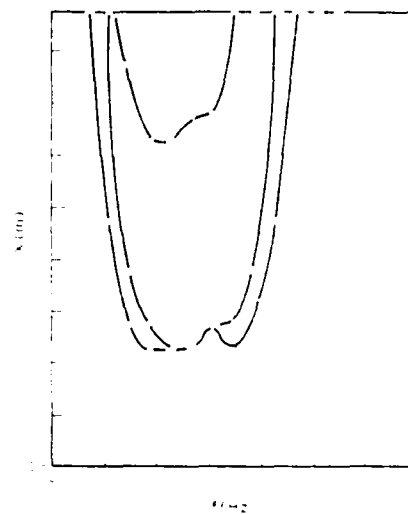


FIG. 8(e).  $Q = 4.68$  W,  $H = 0.13$  m.  $\circ$  8V;  $\triangle$  4V;  $\square$  2V.

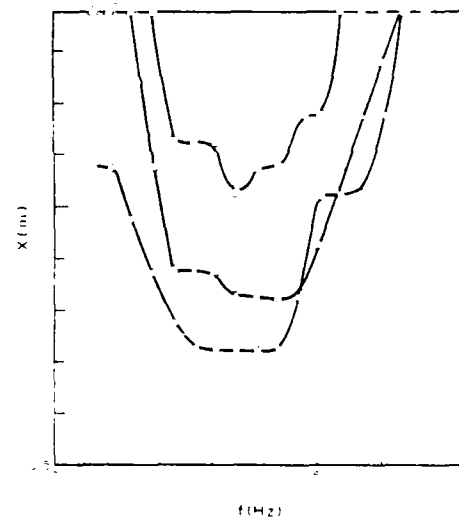


FIG. 8(f).  $Q = 8.5$  W,  $H = 0.13$  m.  $\circ$  4V;  $\triangle$  2V;  $\square$  1V.

FIG. 8. Effect of disturbance frequency and amplitude on the resonance characteristics of the plume. The voltage  $V$  represents the amplitude of the input signal to the loudspeaker.

argument presented in the beginning of this paper [see equations (13) and (14)]

In addition, note that the coefficient in equation (15) is a number greater than unity. This finding validates the time criterion of transitions, equation (8), which translated into a transition Reynolds number considerably greater than unity. For example, by using the  $D$  and  $U$  scales of the plume [equations (11) and (12)], the transition height  $x$  is eliminated from equation (15)

to obtain

$$\frac{DU}{\nu} \sim 10 \frac{z}{D} \quad (16)$$

According to Table 1,  $z/D$  can only be of the order of 2 or greater, hence, the transition Reynolds number  $DU/\nu$  must be a constant considerably greater than unity (in the range  $10^3$ – $10^4$ ). Thus, the present experimental observations support qualitatively and

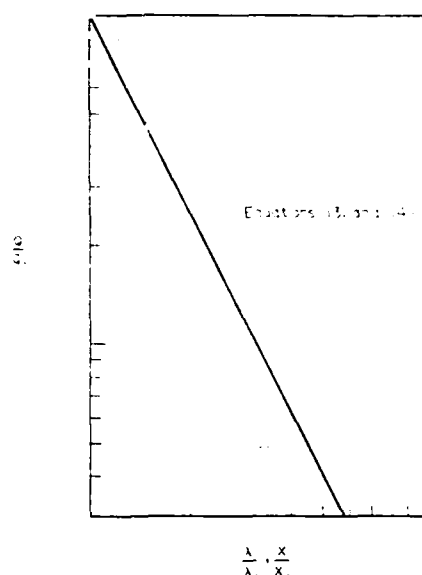


FIG. 9. The transition height and wavelength as a function of heat input, in air plumes excited harmonically by a loudspeaker.  $\circ$   $x$   $x_0$  transition height;  $\triangle$   $\lambda$   $\lambda_0$  wavelength;  $Q_0 = 21$  W;  $x_0 = 0.35$  m;  $\lambda_0 = 0.06$  m.

quantitatively the transition mechanism envisioned in Sections 2 and 3 and in Fig. 1.

It is worth noting that the local Reynolds number transition criterion  $On = 1$  or  $DU/v = O(10^2)$  stated in equations (6) and (8) and verified above, can be easily translated into the Rayleigh or Grashof number language used in natural convection. In fluids with  $Pr > O(1)$  the velocity boundary layer thickness scales as  $x Pr^{1/2} Ra^{-1/4}$  and the vertical velocity as  $(x/x_0) Ra^{1/2}$ , where  $Ra$  is the Rayleigh number  $g\beta x^2 Q/(xv\kappa)$ . Therefore  $DU/v = O(10^2)$  means that at transition the Rayleigh number is  $Ra = O(10^8 Pr^2)$ . For the air plumes

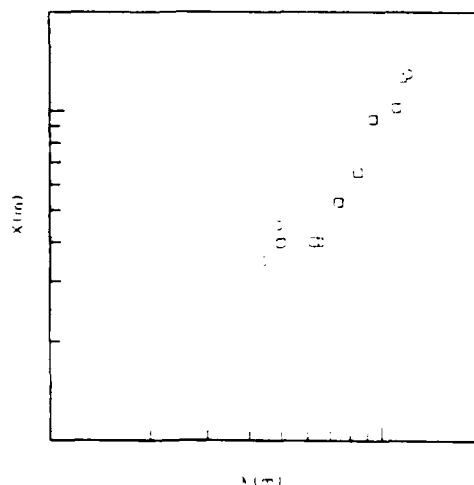


FIG. 10. The measured characteristic wavelength and transition height.  $\circ$  data from Table 2;  $\triangle$  data from Table 3.

Table 2. Transition height and wavelength measurements plotted in Fig. 4

$Q$ (W)	$x$ (m)	$\lambda$ (m)
2.0	0.13	0.12
5.6	0.48	0.095
22	0.48	0.049
31	0.38	0.044
39	0.26	0.040
55*	0.25	0.035

\* Reference power setting

considered in our study this prediction reduces to  $Gr = O(10^8)$ , which the commonly observed range of transition Grashof numbers (note that  $Gr = Ra Pr$ ).

## 7. CONCLUSIONS

This paper described a fundamental study of the phenomenon of transition to turbulence in natural convection plume flow. The experimental part of the study focused on a controlled version of the 'cigarette smoke' plume flow. The experiment demonstrated that:

- (1) at transition, the plume assumes a sinusoidal (meandering) shape of characteristic wavelength, and at a characteristic height above the plume origin [Figs. 5(a)–(c)];
- (2) the transition wavelength scales with the local plume diameter (Figs. 3, 4 and 9);
- (3) the transitional meandering shape is 2-dim., i.e. in one plane [Figs. 7(a)–(c)];
- (4) if the transition is triggered by 'noise', then it is a plume property to 'filter' out of the noise the characteristic transition wavelength which is proportional to the plume diameter at the transition height (Figs. 3 and 4);
- (5) if the transition is triggered by single-frequency forcing, then it is a property of the plume to 'resonate', i.e. to deform most when disturbed with a wavelength which scales with the plume diameter at transition height (Fig. 9).

These experimental conclusions support strongly the theoretical argument presented in Section 2. According to this argument, the phenomenon of

Table 3. Transition height and wavelength measurements plotted in Fig. 9

$Q$ (W)	$x$ (m)	$\lambda$ (m)	$H$ (m)	$f$ (Hz)
1.05	1.28	0.15	0.045	1.9
2.13	1.02	0.11	0.045	2.8
3.56	0.94	0.095	0.045	3.9
6.79	0.65	0.085	0.045	5.5
9.7	0.53	0.075	0.045	6.4
14.9	0.40	0.065	0.045	8
17.8	0.40	0.063	0.045	9.1
21.0*	0.40	0.050	0.045	10

\* Reference power setting

transition is:

- (a) an intrinsic property of the flow;
- (b) the result of the internal competition among two characteristic time scales of the stream, the minimum fluctuation period  $t_{\min}$  and the viscous penetration time  $t_v$ ;
- (c) characterized by a unique meandering wavelength which is always proportional to the local stream thickness.

The transition mechanism proposed in Section 2 evolved from a review of classical hydrodynamic stability results (Table 1) and led to the flow properties (scaling) embodied in the time criterion  $t_{\min} \sim t_v$  [equations (6) and (7)]. The same scales and time criterion have been brought to light earlier by the buckling theory of inviscid flow [16]. It was shown recently [21] that the buckling time criterion  $N_B = O(1)$  also predicts correctly the transition in free jet flow, shear flow and wake flow, as well as a series of turbulent boundary layer features such as the bursting frequency and the viscous sublayer thickness. Thus, the present study reveals an important relationship (equivalence) between stability theory and buckling theory with regard to explaining transition.

**Acknowledgements**—This research was supported by the Office of Naval Research.

#### REFERENCES

1. B. Gebhart, *Ann. Rev. Fluid Mech.* **5**, 213–246 (1973).
2. C. S. Yih, Free convection due to a point source of heat, *Proc. 1st U.S. Natl. Congr. Appl. Math.* **21**, 941–947 (1951).
3. C. S. Yih, Laminar free convection due to a line source of heat, *Trans. Am. Geophys. Un.* **33**, 669–672 (1962).
4. R. S. Brand and F. J. Lahey, The heated laminar vertical jet, *J. Fluid Mech.* **29**, 305–319 (1967).
5. T. Fujii, Theory of steady laminar natural convection above a horizontal line source and a point heat source, *Int. J. Heat Mass Transfer* **6**, 597–606 (1963).
6. K. Brodowicz and W. T. Kierkus, Experimental investigation of laminar free convection flow in air above a horizontal wire with constant heat flux, *Int. J. Heat Mass Transfer* **9**, 81–94 (1966).
7. R. J. Forstrom and E. M. Sparrow, Experiments on the buoyant plume above a heated horizontal wire, *Int. J. Heat Mass Transfer* **10**, 321–331 (1967).
8. A. W. Schorr and B. Gebhart, An experimental investigation of natural convection wakes above a line heat source, *Int. J. Heat Mass Transfer* **13**, 557–571 (1970).
9. L. Pera and B. Gebhart, On the stability of laminar plumes: some numerical solutions and experiment, *Int. J. Heat Mass Transfer* **14**, 975–984 (1971).
10. J. C. Mollendorf, The effect of thermal buoyancy on the hydrodynamic stability of a round laminar vertical jet, Ph.D thesis, Cornell University, Ithaca, New York (1971).
11. Lord Rayleigh, On the stability, or instability of certain fluid motions, *Proc. of London Math. Soc.* **11**, 57–70 (1880).
12. H. Lamb, *Hydrodynamics*, pp. 672–673. Dover, New York (1945).
13. G. K. Batchelor and A. E. Gill, Analysis of the stability of axisymmetric jets, *J. Fluid Mech.* **14**, 529–551 (1962).
14. J. L. Lopez and V. H. Kurzweg, Amplification of helical disturbances in a round jet, *Physics Fluids* **20**, 860–861 (1977).
15. H. Schlichting, *Boundary Layer Theory* (4th edn.), p. 72. McGraw-Hill, New York (1960).
16. A. Bejan, On the buckling property of inviscid jets and the origin of turbulence, *Lett. Heat Mass Transfer* **8**, 187–194 (1981).
17. P. Bradshaw, *An Introduction to Turbulence and its Measurement*, p. 19. Pergamon Press, Oxford (1971).
18. B. Gebhart, *Heat Transfer* (2nd edn.), Ch. 8. McGraw-Hill, New York (1971).
19. B. Gebhart, private communication to A. Bejan, Nov. 1981.
20. S. Kimura, Buckling flow and transition to turbulence in axisymmetric plumes, Ph.D thesis, Department of Mechanical Engineering, University of Colorado, Boulder, Colorado (1983).
21. A. Bejan, *Entropy Generation through Heat and Fluid Flow*, Ch. 4. Wiley, New York (1982).

#### MECANISME DE LA TRANSITION VERS LA TURBULENCE DANS UN ECOULEMENT DE PANACHE

**Résumé**—On étudie théoriquement et expérimentalement le mécanisme fondamental responsable de la transition dans la convection naturelle d'un panache. Théoriquement, la transition apparaît quand le temps de pénétration visqueuse normale au panache devient comparable à la période de temps minimale de fluctuation du panache comme un écoulement instable non visqueux. On suppose aussi qu'à la transition, la longueur d'onde du panache est en proportion du diamètre local du panache. La partie expérimentale de l'étude est focalisée sur la transition dans un panache axisymétrique d'air au-dessus d'une source ponctuelle. Une visualisation par fumée de la forme du panache à la transition conduit à des observations extensives qui soutiennent fortement le mécanisme proposé dans la théorie. Le sillage de transition serpente dans un plan (bidimensionnellement) et avec une longueur d'onde qui est à l'échelle du diamètre du panache. S'il est excité extérieurement par des longueurs d'onde, le panache a la propriété de sélectionner la longueur d'onde proposée théoriquement. On discute l'équivalence entre le mécanisme de transition proposé et celui de la théorie du flambement.



# Buckling of a turbulent jet surrounded by a highly flexible duct

Ren Anderson and Adrian Bejan

Department of Mechanical Engineering, University of Colorado, Boulder, Colorado 80309

(Received 24 February 1983; accepted 18 July 1983)

An experimental and theoretical study of the static buckling of a downward flowing stream surrounded by a highly flexible duct is reported. It is shown analytically that the stream buckles into a meandering shape that depends strongly on the flow velocity in the duct. The amplitude of the buckled shape is found to be governed by the magnitude of the transverse force created by nonzero curvature at the free end of the duct. Experimental measurements confirm the buckled shape described analytically.

## I. INTRODUCTION

In the course of flow visualization experiments with turbulent water jets we discovered that vertical jets surrounded by thin rubber ducts naturally buckle into a stable shape that is a strong function of the flow velocity in the duct. At small flow rates the buckling of the duct is limited to regions near its free end. As the flow rate is increased the buckled portion of the duct also increases, appearing to "climb" up the duct until its entire length is filled with small-amplitude standing waves. The equilibrium shape of the duct is roughly sinusoidal with a wavelength that is inversely proportional to both flow velocity and distance from the fixed end of the duct. Three photographs of a buckled duct containing flowing water are shown in Fig. 1. The flow velocity in these photographs increases from left to right.

Further increases in flow velocity beyond what is shown in Fig. 1 eventually lead to loss of stability and the initiation of self-excited vibrations of the duct and enclosed jet. These vibrations have been the major focus of previous studies using cantilevered ducts containing flowing fluid. The phenomenon of static buckling has not received as much attention as the self-excited vibrations, possibly because of misunderstandings concerning the conditions under which buckling develops. For example, Thompson<sup>1</sup> reports that cantilevered ducts which are *initially straight* cannot buckle under the influence of flowing fluids. He is correct in theory but not in practice, because real ducts are never perfectly straight. As shown below, any slight initial curvature of the duct causes a nonzero transverse force at its free end and leads to buckling, provided that the flow velocity is large enough.

Interest in the flow-induced instabilities of ducts conveying fluids has been largely motivated by the practical problems of pipeline and heat exchanger design. Niordsen<sup>2</sup> was one of the first to derive the correct form of the equations of motion. In the course of a study of flow through segmented pipes with flexible joints Benjamin<sup>3,4</sup> confirmed Niordsen's derivation by using Hamilton's principle. Gregory and Paidoussis<sup>5,6</sup> and Paidoussis<sup>7</sup> extended Benjamin's analysis to the case of continuous elastic tubing. Benjamin's study, like those of Gregory and Paidoussis, is devoted primarily to stability analyses aimed at determining the onset of self-excited vibrations. Bishop and Fawzy<sup>8</sup> observed static buck-

ling during their experiments with forced oscillations of vertical ducts filled with flowing fluid, but reported their observations without attempting to explain them. More recently Lundgren, Sethna, and Bajaj<sup>9</sup> observed large-amplitude buckling of a cantilevered duct when they attached an inclined nozzle to the free end of the duct. They calculated the static solution for the buckled shape which resulted from the attachment of the nozzle, and examined the stability of the static solution. They found that, with the nozzle attached, the orientation of self-excited oscillations was no longer random but occurred either in the plane of the nozzle or perpendicular to that plane.

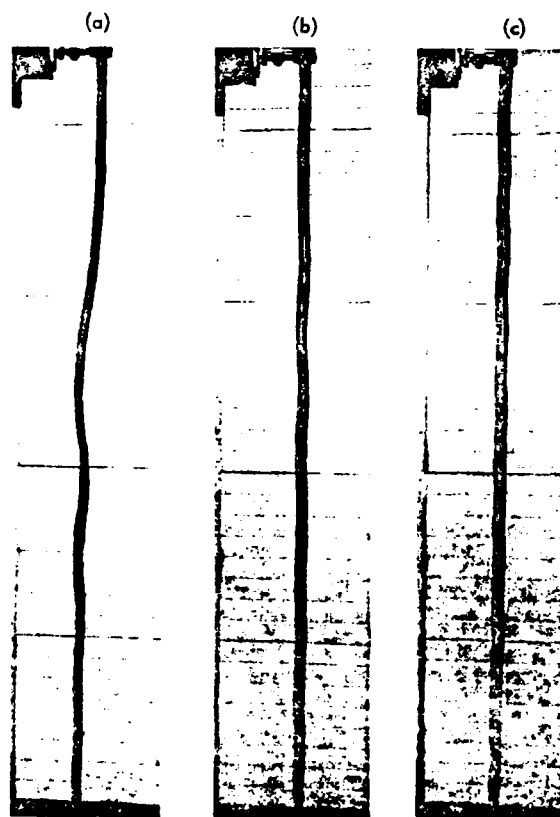


FIG. 1. Static buckling of a vertical hose with a diameter of 12.7 mm: (a)  $V = 1.9$  m/sec,  $\alpha\beta = 2.78$ ; (b)  $V = 3.15$  m/sec,  $\alpha\beta = 1.01$ ; (c)  $V = 4.73$  m/sec,  $\alpha\beta = 0.45$ .

Our objective in the present study is to focus on the small-amplitude static buckling which is exhibited by a turbulent jet which is bounded by a highly flexible duct. This is the "flow-dominated" regime of the pipe vibration phenomenon studied by earlier investigators. In the analysis presented below we will include a gravitational tension term not considered by Lundgren *et al.*<sup>9</sup> in their study of horizontal ducts. This gravitational term causes the wavelength of the buckled duct to decrease with increasing distance from the fixed end of the duct. In addition we will show that, if the flow through the duct is considered to be inviscid, then the effective bending stiffness of the duct/jet system is increased by nonuniform pressure and tension distributions created by the local curvature of the duct. After deriving the equilibrium equation describing the system, we will find perturbation solutions valid for short, flexible ducts in the limits  $V^2 = O(\epsilon)$  and  $V^2 = O(1/\epsilon)$ . We will conclude the paper by comparing the wavelength predictions made by a perturbation solution appropriate for long ducts to experimental measurements derived from photographs such as those shown in Fig. 1.

## II. MATHEMATICAL FORMULATION

The basic geometry of the problem considered in this paper is shown in Fig. 2. A flexible tube of radius  $r$  and length  $L$  houses a stream of mean velocity  $V$  and density  $\rho$ . The centerline of the flexible duct is described by the curve  $y(x)$ . The duct is assumed to undergo small-amplitude, beam-like deflections with no change in the shape of its cross section. These deflections are assumed to be small enough so that secondary flows can be ignored. The fluid mass per unit of duct length is  $m_f$ , while the wall mass per unit length is  $m$ . As shown in Fig. 2, the average pressure, tension force, shear

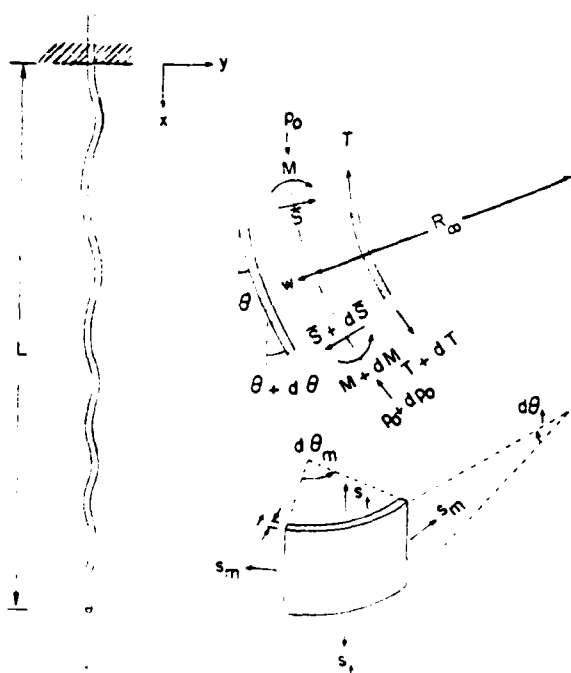


FIG. 2 Forces and moments acting on a duct element.

force, and bending moment are represented by  $p_0$ ,  $T$ ,  $\bar{S}$ , and  $M$ . Finally, in accordance with the notation employed in membrane stress analysis,<sup>10</sup> we write  $t$ ,  $s_m$ , and  $s_t$  for wall thickness, meridional stress, and tangential stress, respectively.

A force balance in the vertical direction ( $x$ ) yields

$$(m_f + m)g dx + (p_0 A - T) \cos \theta + [T + dT - A(p_0 + dp_0)] \cos(\theta + d\theta) = 0. \quad (1)$$

For small amplitudes,  $\cos(d\theta) \approx \cos(\theta + d\theta) \approx 1$ , and Eq. (1) can be simplified to the form

$$(m_f + m)g = \frac{d}{dx} (p_0 A - T). \quad (2)$$

Integrating Eq. (2) we obtain

$$(m_f + m)g(x - L) = p_0 A - T. \quad (3)$$

The constant of integration in Eq. (3) was evaluated by applying the free-end condition  $T = p_0 = 0$  at  $x = L$ .

The fluid velocity in the horizontal ( $y$ ) direction is

$$\frac{d}{dt} \{y[x(t)]\} = \frac{dy}{dx} \frac{dx}{dt} = V \frac{dy}{dx}, \quad (4)$$

and the acceleration of the fluid in the horizontal direction is

$$\frac{d^2}{dt^2} \{y[x(t)]\} = V^2 \frac{d^2 y}{dx^2}. \quad (5)$$

Applying Newton's second law of motion and ignoring second-order terms, we find

$$m_f V^2 \frac{d^2 y}{dx^2} = \frac{d}{dx} \left( (T - p_0 A) \frac{dy}{dx} \right) - \frac{d\bar{S}}{dx}. \quad (6)$$

Substituting for the pressure  $p_0$  and tension  $T$  from Eq. (3), reduces Eq. (6) to

$$m_f V^2 \frac{d^2 y}{dx^2} = \frac{d}{dx} \left( (m_f + m)g(L - x) \frac{dy}{dx} \right) - \frac{d\bar{S}}{dx}. \quad (7)$$

It is instructive at this point to examine the physical meaning of each of the terms in Eq. (7). As the fluid moves through the duct it undergoes centripetal acceleration by virtue of the fact that it is following a slightly curved path. The centripetal term on the left-hand side of the equation is balanced on the right-hand side by gravitationally induced wall tension and by a transversal shear force. In the limiting case of zero fluid flow and zero bending stiffness (i.e., zero shear force), Eq. (7) reduces to the equation describing a hanging chain. A surprising implication of Eq. (7) is that the static equilibrium of the duct does not depend on the viscosity of the fluid flowing through the duct. This result is due to the fact that the tension induced in the duct walls by frictional fluid drag is exactly offset by the pressure force required to force the fluid through the duct.

The transversal shear force  $\bar{S}$  can be evaluated by requiring rotational equilibrium about the bottom face of the duct segment shown in Fig. 2.

$$\bar{S} = \frac{dM}{dx}, \quad (8)$$

where  $M$  is the total bending moment acting over the duct cross section. As shown next, this bending moment is due to three independent effects: (a) the asymmetric distribution of

fluid velocity and pressures; (b) the asymmetric distribution of tangential stresses in the wall caused by jet flow; and (c) the  $EI$  bending stiffness of the tube, predicted by classical beam theory. Since in the limit of small-amplitude deflections these effects are not coupled with one another, each will be considered separately.

In an inviscid jet with an infinitely large radius of curvature  $R_\infty$ , the velocity and pressure distributions are<sup>11</sup>

$$V(w) = V(1 - w/R_\infty), \quad (9)$$

$$p(w) = p_0 + \rho V^2 w/R_\infty. \quad (10)$$

The "jet" bending moment  $M_j$  associated with these asymmetric profiles is<sup>11</sup>

$$M_j = \rho V^2 I_0 \frac{d^2 y}{dx^2}. \quad (11)$$

In Eqs. (9) and (10), coordinate  $w$  is measured radially from the jet centerline, away from the centerline of curvature (see Fig. 2). The symbol  $I_0$  denotes the area moment of inertia of the jet cross section (for a round jet,  $I_0 = \pi r^4/4$ ).

The membrane stresses induced in the wall by the pressure variation across the duct are shown in the bottom portion of Fig. 2. The horizontal components of these membrane stresses must balance the internal pressure force acting on the duct wall

$$s_m t ds d\theta_m + s_t t ds d\theta_t = p ds^2. \quad (12)$$

Since

$$\frac{ds}{r} = d\theta_m \quad (13)$$

and

$$\frac{ds}{R_t} = d\theta_t, \quad (14)$$

Eq. (12) becomes

$$\frac{s_m}{r} + \frac{s_t}{R_t} = \frac{p}{t}. \quad (15)$$

The relation between  $R_t$  and  $R$  is shown in Fig. 3. The hoop stress,  $s_m$ , can be found by integrating the pressure across a section of the duct as is shown in Fig. 3,

$$(R_\infty + w)s_m t \cos \phi = \int_0^{w_0} \left[ p_0 + \left( \frac{\rho V^2 w'}{R_\infty} \right) \right] (R_\infty + w') dw'. \quad (16)$$

Performing this integral and recognizing that

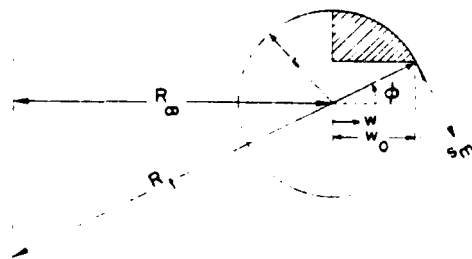


FIG. 3. Force balance for calculating the hoop stress  $s_m$ .

$$\left(1 + \frac{w}{R_\infty}\right)^{-1} = 1 - \frac{w}{R_\infty} + \left(\frac{w}{R_\infty}\right)^2 - \dots, \quad (17)$$

and

$$w_0 = r \cos \phi, \quad (18)$$

yields

$$s_m = (r/t) [p_0 + (r \cos \phi / 2R_\infty) (\rho V^2 - p_0)]. \quad (19)$$

The tangential stress distribution  $s_t$ , which is needed for calculating the bending moment, follows immediately from Eqs. (15) and (10),

$$s_t = (r/2t) (\rho V^2 + p_0) (1 + r \cos \phi / R_\infty). \quad (20)$$

The "membrane" contribution to bending moment,  $M_m$ , is therefore

$$M_m = 2 \int_0^\pi s_t r^2 \cos \phi d\phi, \quad (21)$$

$$M_m = \frac{2I_0}{R_\infty} (\rho V^2 + p_0) \approx 2I_0 (\rho V^2 + p_0) \frac{d^2 y}{dx^2}. \quad (22)$$

So far, the first two contributions to the bending moment, Eqs. (11) and (22) are due to the jet flow through the highly flexible envelope. The third and final contribution to the bending moment is a well-known result of classical beam theory. The bending moment due to the bending stiffness of the annular duct is<sup>12</sup>

$$M_b = EI \frac{d^2 y}{dx^2}, \quad (23)$$

where  $I = \pi r^3 t$ .

The total bending moment is obtained by adding Eqs. (11), (22), and (23)

$$M = [EI + I_0(3\rho V^2 + 2p_0)] \frac{d^2 y}{dx^2}. \quad (24)$$

Combining (24), (8), and (7), we obtain the equilibrium condition

$$[EI + I_0(3\rho V^2 + 2p_0)] \frac{d^4 y}{dx^4} + m_f V^2 \frac{d^2 y}{dx^2} + \frac{d}{dx} \left( (m_f + m)g(x - L) \frac{dy}{dx} \right) = 0. \quad (25)$$

This result indicates that the effective bending stiffness of the duct is increased by nonsymmetric pressure and tension distributions created by the slight local curvature of the duct.

The boundary conditions which must be satisfied at the upper (fixed) and lower (free) ends of the duct are

$$y = 0 \quad \text{at } x = 0, \quad (26)$$

$$\frac{dy}{dx} = 0 \quad \text{at } x = 0, \quad (27)$$

and

$$\frac{d^2 y}{dx^2} = 0, \quad (28)$$

$$(EI + 3\rho V^2 I_0) \frac{d^3 y}{dx^3} = m_f V^2 S \quad \text{at } x = L. \quad (29)$$

Equations (26)–(28) are the standard end conditions applied to the fixed and free ends of a simple cantilever and require no further comment. Equation (29) is unique to the problem

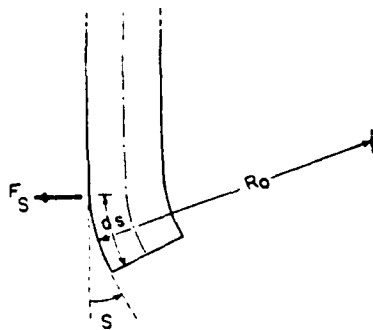


FIG. 4. Origin of the transverse force  $F_S$ . The magnitude of  $S$  has been greatly exaggerated.

of a highly flexible duct conveying fluid, and incorporates the important physical observation that no real duct is ever perfectly straight. The weight of the fluid flowing through the duct will tend to straighten it except for a short region of unknown length  $ds$  near its free end (Fig. 4). This results in a small transverse force  $F_S$  due to the reaction force of the fluid as it leaves the duct:

$$F_S = m_f V^2 \sin(ds/R_0) \approx m_f V^2 ds(y''_0)_{x=L}. \quad (30)$$

This reaction force is expressed in (29) in terms of the unknown constant

$$S = ds(y''_0)_{x=L}. \quad (31)$$

It is shown below that the sole function of  $S$  is to determine the amplitude of the buckled duct.

Dividing (25) by  $EI + 3\rho V^2 I_0$  and introducing the non-dimensional variables

$$\hat{y} = y/L, \quad (32)$$

$$\hat{x} = x/L, \quad (33)$$

reduces the equilibrium equation and boundary conditions to the form

$$[1 + \gamma(1 - \hat{x})] \frac{d^4 \hat{y}}{d\hat{x}^4} + \frac{d}{d\hat{x}} \left( \beta^2 [1 + \alpha\beta(\hat{x} - 1)] \frac{d\hat{y}}{d\hat{x}} \right) = 0, \quad (34)$$

$$\hat{y} = 0 \quad \text{at } \hat{x} = 0, \quad (35)$$

$$\frac{d\hat{y}}{d\hat{x}} = 0 \quad \text{at } \hat{x} = 0, \quad (36)$$

and

$$\frac{d^2 \hat{y}}{d\hat{x}^2} = 0, \quad (37)$$

$$\frac{d^3 \hat{y}}{d\hat{x}^3} = \beta^2 S \quad \text{at } \hat{x} = 1. \quad (38)$$

The centerline pressure in the duct,  $p_0$ , has been expressed as a linear function of  $\hat{x}$  by relating the pressure gradient to the dynamic head via a resistance coefficient  $\omega$ :

$$\frac{dp}{d\hat{x}} = \frac{\omega}{2} \left( \frac{L}{D} \right) \rho V^2, \quad (39)$$

$$p_0 = \frac{\omega}{2} \frac{L}{D} \rho V^2 (1 - \hat{x}). \quad (40)$$

For turbulent flow the resistance coefficient is small and approximately constant

$$\omega = O(\epsilon). \quad (41)$$

The nondimensional parameters appearing in (34) are

$$\alpha = \frac{1}{4} \left( \frac{m_f + m}{m_f} \right) \left( \frac{gD}{V^2} \right) \left( \frac{EI}{\rho V^2 I_0} + 3 \right)^{1/2}, \quad (42)$$

$$\beta = \frac{4L/D}{(EI/\rho V^2 I_0 + 3)^{1/2}}, \quad (43)$$

$$\gamma = \frac{\omega L/D}{EI/\rho V^2 I_0 + 3}. \quad (44)$$

Each of these parameters depends upon  $V^2$ , reflecting the strong influence of fluid velocity shown in Fig. 1.

The final character of the solution to (32)–(36) depends to a large degree upon the sign of the function

$$z = 1 + \alpha\beta(\hat{x} - 1), \quad (45)$$

which appears in the second term of Eq. (34). Function  $z$  changes sign when  $\hat{x}$  passes through the "turning point"

$$\hat{x}_{TP} = 1 - 1/\alpha\beta. \quad (46)$$

The location of this point defines the transition between the buckled and unbuckled portion of the duct [Fig. 1(a)], and is positive and nonzero provided that  $\alpha\beta > 1$ . This can be seen explicitly by considering the velocity-dependent behavior of a short, flexible duct with

$$L/D = O(1), \quad (47)$$

$$\frac{EI}{\rho V^2 I_0} = O\left(\frac{(\text{length/time})^2}{V^2}\right), \quad (48)$$

$$\frac{gD}{V^2} = O\left(\frac{(\text{length/time})^2}{V^2}\right), \quad (49)$$

$$(m_f + m)/m_f = O(1). \quad (50)$$

Conditions (48) and (49) are intended to simulate experimental conditions when the physical properties of the duct are held constant while the fluid velocity is varied. Under these conditions,  $\alpha$ ,  $\beta$ , and  $\gamma$  become

$$\alpha = O\left[\frac{EI}{\rho V^2 I_0} \left(\frac{EI}{\rho V^2 I_0} + 3\right)^{1/2}\right], \quad (51)$$

$$\beta = O[4/(EI/\rho V^2 I_0 + 3)], \quad (52)$$

$$\gamma = O[\epsilon/(EI/\rho V^2 I_0 + 3)]. \quad (53)$$

The velocity dependence of these parameters is summarized in Table I.

To demonstrate the general behavior of the solution we will first consider the small velocity limit  $\rho V^2 I_0/EI = O(\epsilon)$ . By neglecting  $\beta^2$  and  $\gamma$ , integrating once and introducing the change of variables

TABLE I. Velocity dependence of  $\alpha$ ,  $\beta$ , and  $\gamma$  for the case of a short, flexible duct.

$\rho V^2 I_0/EI$	$\alpha$	$\beta$	$\gamma$
$O(\epsilon)$	$O(\epsilon^{-1/2})$	$O(\epsilon^{1/2})$	$O(\epsilon^2)$
$O(1)$	$O(1)$	$O(1)$	$O(\epsilon)$
$O(1/\epsilon)$	$O(\epsilon)$	$O(1)$	$O(\epsilon)$

$$\zeta = -\alpha^{1/2}\beta(\hat{x} - 1), \quad (54)$$

$$\bar{y} = \frac{d\bar{y}}{d\zeta}, \quad (55)$$

we can transform (34) into the homogeneous Airy equation

$$\frac{d^2\bar{y}}{d\zeta^2} - \zeta\bar{y} = 0, \quad (56)$$

with the general solution

$$\bar{y} = C_1 \text{Ai}(\zeta) + C_2 \text{Bi}(\zeta). \quad (57)$$

However, application of conditions (36) and (37) produces the trivial result  $C_1 = C_2 = 0$  and the conclusion that the duct will not buckle when the velocity is small.

In the large velocity limit [ $\rho V^2 I_0 / EI = O(1/\epsilon)$ ] we proceed in a similar manner. Neglecting  $\alpha$  and  $\gamma$  and introducing the change of variables

$$\bar{y} = \frac{d\bar{y}}{d\hat{x}}, \quad (58)$$

Eq. (34) becomes

$$\frac{d^2\bar{y}}{d\hat{x}^2} + \beta^2\bar{y} = \beta^2 K(V), \quad (59)$$

$$K(V) = S + \bar{y}(1). \quad (60)$$

This is equivalent to the horizontal problem considered by Lundgren *et al.*<sup>9</sup> and leads to the solution

$$\bar{y} = S [\cos \beta - \cos \beta(\hat{x} - 1)], \quad (61)$$

and the conclusion that for large velocities the entire length of the duct is buckled. Note that the unknown parameter  $S$  serves only to determine the amplitude of the solution and does not influence the buckled shape.

Finally, in the moderate velocity limit [ $\rho V^2 I_0 / EI = O(1)$ ] we neglect  $\gamma$ , integrate once and introduce the change of variables

$$\eta = -z/\alpha^{2/3}, \quad (62)$$

$$y^* = \frac{dy}{d\eta}. \quad (63)$$

These steps reduce (34) to the form of a nonhomogeneous Airy equation

$$\frac{d^2 y^*}{d\eta^2} - \eta y^* = -\frac{K(V)}{\alpha\beta}, \quad (64)$$

with the solution<sup>13</sup>

$$y^* = \frac{-S [Gi(\eta) + C_1 Ai(\eta) + C_2 Bi(\eta)]}{\alpha\beta [Gi''(b) + C_1 Ai''(b) + C_2 Bi''(b)]}, \quad (65)$$

$$C_1 = \frac{[Gi'(b)Bi(a) - Gi(a)Bi'(b)]}{[Ai(a)Bi'(b) - Ai'(b)Bi(a)]}, \quad (66)$$

$$C_2 = \frac{[Gi(a)Ai'(b) - Gi'(b)Ai(a)]}{[Ai(a)Bi'(b) - Ai'(b)Bi(a)]}, \quad (67)$$

$$Gi(\eta) = \frac{1}{3}Bi(\eta) + \frac{dAi}{d\eta} \int_0^\eta Bi(t)dt - \frac{dBi}{d\eta} \int_0^\eta Ai(t)dt, \quad (68)$$

$$a = -(1 - \alpha\beta)/\alpha^{2/3}, \quad (69)$$

$$b = -1/\alpha^{2/3}. \quad (70)$$

The functions Ai and Bi are shown in Fig. 5. The solution (65) will exhibit buckling behavior when  $\eta$  is negative

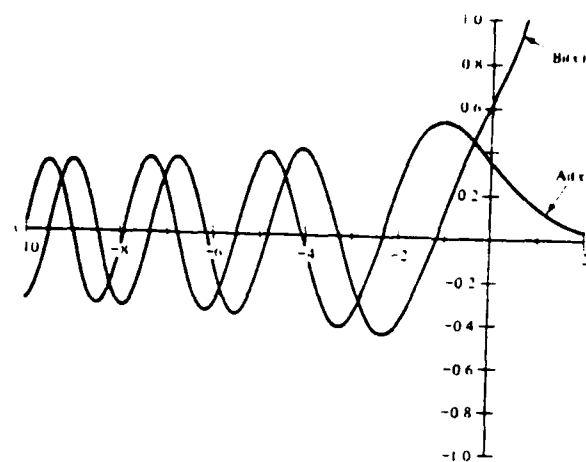


FIG. 5. Plot of the Airy functions Ai(x) and Bi(x). (Taken from Ref. 14, p. 69.)

and exponential behavior when  $\eta$  is positive. The transition between the two forms of behavior is defined by the location of the turning point expressed in (46).

### III. LONG DUCT EXPERIMENTS

In the previous section we have shown that the qualitative behavior of the solution to (34)–(38) agrees with the general observations described in the introduction. To test this agreement in quantitative terms we experimented with long ducts in the fully buckled regime ( $\alpha\beta < 1$ ). After testing several different materials, we chose to do our measurements using surgical drainage tubing made of latex rubber. We used two different tube sizes: the smaller had an inner diameter of 9.5 mm and a wall thickness of 0.3 mm, while the corresponding dimensions of the larger size were 12.7 mm and 0.34 mm. For both sizes, the length of the tube was one meter. The flexible tube was clamped to an inlet nozzle connected to the building water supply. The Reynolds number based on duct diameter varied from  $10^4$  to  $5 \times 10^4$ .

Figure 6 shows a schematic drawing of the experimental apparatus. In order to avoid the secondary effects asso-

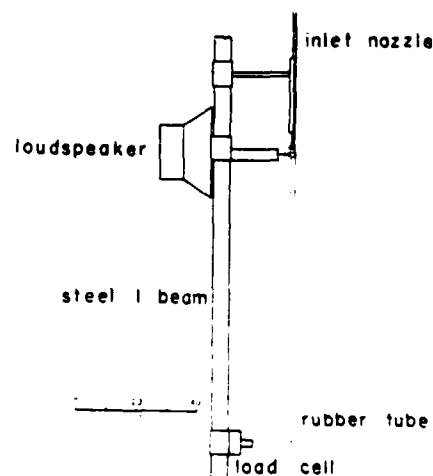


FIG. 6. Schematic of experimental apparatus.

ciated with bends (elbows) in the piping, the length of the inlet section was always greater than 50 times the rubber tube diameter. The inlet section had the same inner diameter as the rubber tube, and the inlet nozzle was tapered to a knife edge in order to avoid flow separation at the point where the water leaves the nozzle and enters the rubber tube. The flow was measured by taking timed volumetric samples of the water leaving the flexible tube. At each flow setting, the shape of the buckled tube was recorded photographically (see Fig. 1).

As argued in Sec. II of this paper, the bending stiffness of the flexible duct is a pivotal parameter in predicting the buckled shape of the duct. The bending stiffness of the tubing material was measured in two different ways. In the first method, Young's modulus was calculated using a load cell, by measuring the force required to elongate the tubing by a given amount. The experimentally measured Young's modulus was then multiplied by the area moment of inertia calculated from the physical dimensions of the tubing. This value was double checked by measuring the fundamental frequency of a short section of the water-filled tube. The corresponding value for  $EI$  was then calculated by using the formula for a simple cantilever beam. The frequency measurement was accomplished by shaking the tube with an arm attached to the cone of a loudspeaker (see Fig. 6). The Young's modulus determined by these methods was found to be  $1.7 \times 10^6 \text{ N/m}^2$  with the static test giving values 10%–15% higher than those determined by the dynamic test.

A typical experimental run was started with the tube hanging limp (collapsed, with elliptical cross section). When the water was turned on the duct began to buckle from its free end as described in the introduction. The length of the buckled portion of the duct increased with increasing flow velocity until  $\alpha\beta$  reached the value 0.35 for the larger diameter duct (0.43 for the smaller diameter duct) when self-excited vibrations began near the free end of the duct. The ducts were rotated end for end during the experiment to test for systematic error associated with the specific shape of the duct. The only quantity that was found to vary significantly was the amplitude of the buckled shape, in agreement with results (61) and (65).

The scaling that is appropriate for the ducts used during the experiment differs from the short ducts considered in the previous section:

$$gD/V^2 = O(\epsilon), \quad (71)$$

$$EI/\rho V^2 I_0 = O(1/\epsilon), \quad (72)$$

$$L/D = O(1/\epsilon), \quad (73)$$

$$(m_f + m)/m_f = O(1), \quad (74)$$

$$\alpha = O(\epsilon^{1/2}), \quad (75)$$

$$\beta = O(\epsilon^{-1/2}), \quad (76)$$

$$\gamma = O(\epsilon). \quad (77)$$

Neglecting  $\gamma$ , integrating once, and introducing the change of variables

$$u = \frac{d\hat{y}}{dz} \frac{\alpha\beta}{K(V)}, \quad (78)$$

reduces (32) to the form

$$\alpha^2 \frac{d^2 u}{dz^2} + zu = 1. \quad (79)$$

Functions  $K$  and  $z$  have been previously defined in (60) and (45). Because we expect a spatially periodic result, we will seek a solution in terms of an exponential WKB expansion<sup>14</sup>

$$u \sim \exp\left(\frac{1}{\alpha} \sum_n \alpha^n s_n(z)\right). \quad (80)$$

The functions  $s_n$  are determined by substituting this expansion into the homogeneous portion of (79)

$$s_0 = \pm i \frac{1}{2} z^{3/2}, \quad (81)$$

$$s_1 = -\frac{1}{4} \ln z. \quad (82)$$

When expressions (81) and (82) are introduced back into Eq. (80) we find the WKB solution for the homogeneous equation to be

$$u_h = \frac{1}{z^{1/4}} \left[ C_1 \cos\left(\frac{2}{3\alpha} z^{3/2}\right) + C_2 \sin\left(\frac{2}{3\alpha} z^{3/2}\right) \right]. \quad (83)$$

The corresponding particular solution is found by solving (79) in the limit  $\alpha^2 = 0$  and is

$$u_p = 1/z. \quad (84)$$

Combining (83) and (84), applying conditions (35)–(38) and transforming back to the nondimensional physical coordinate  $\hat{x}$ , leads to the final form

$$\frac{d\hat{y}}{d\hat{x}} = \frac{S}{\alpha^2 D} \left\{ \frac{1}{2} + \frac{1}{z^{1/4}} \left[ C_1 \cos\left(\frac{2}{3\alpha} z^{3/2}\right) + C_2 \sin\left(\frac{2}{3\alpha} z^{3/2}\right) \right] \right\}, \quad (85)$$

$$D = \left\{ 2 + \left( \frac{5}{16} - \frac{1}{\alpha^2} \right) \left[ C_1 \cos\left(\frac{2}{3\alpha} \right) + C_2 \sin\left(\frac{2}{3\alpha} \right) \right] \right\}, \quad (86)$$

$$C_1 = \frac{(1/C^{3/4})[\sin(2/3\alpha)/4 - \cos(2/3\alpha)/\alpha] - \sin(2C^{3/2}/3\alpha)}{[\cos(2/3\alpha)(C^{3/2} - 1)/\alpha + \sin(2/3\alpha)(C^{3/2} - 1)/4]}, \quad (87)$$

$$C_2 = \frac{\cos(2C^{3/2}/3\alpha) - (1/C^{3/4})[\sin(2/3\alpha)/\alpha + \cos(2/3\alpha)/4]}{[\cos(2/3\alpha)(C^{3/2} - 1)/\alpha + \sin(2/3\alpha)(C^{3/2} - 1)/4]}, \quad (88)$$

$$C = 1 - \alpha\beta. \quad (89)$$

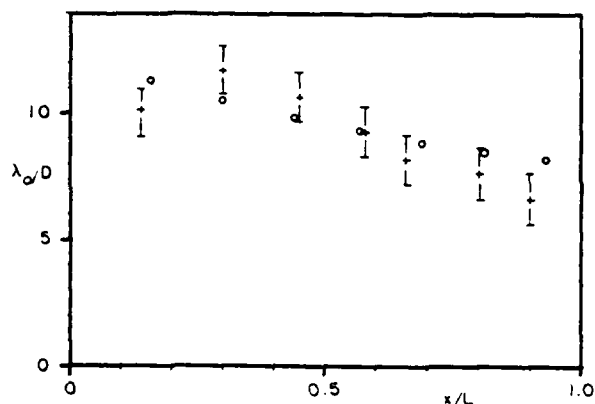


FIG. 7. Plot of  $\lambda_0$  when  $V = 4.05$  m/sec.  $\alpha = 0.01$ ,  $\beta = 57.4$ ,  $D = 12.7$  mm,  $L/D = 72$ ,  $EI = 4.65 \times 10^{-4}$  Nm<sup>2</sup>, and  $m_f/(m_f + m) = 0.895$ . (+ = experimental value, O = theoretical value.)

Equation (85) was integrated numerically from  $\hat{x} = 0$  to  $\hat{x} = 1$ . During the integration the distance between successive crossings of an imaginary line extending from the origin to the free end of the duct was recorded for comparison with measurements taken from photographs of buckled ducts. We define the distance between crossings to be  $\lambda_0$  and show the results of this comparison in Figs. 7–9. The experimental measurements are denoted by + 's and the numerical results derived from (85) are denoted by O's. The agreement is good, both in terms of the location of the crossings and the magnitude of  $\lambda_0$ . The total number of crossings measured from photographs agree with those predicted analytically, except for the case shown in Fig. 9. It is felt that this is a result of our inability to interpret the photographs accurately near the free end of the duct.

#### IV. CONCLUSIONS

We have shown analytically that static buckling of a highly flexible duct filled with flowing fluid is a result of the shear force created by the unavoidable initial curvature of the duct. We found that this shear force governs the ampli-

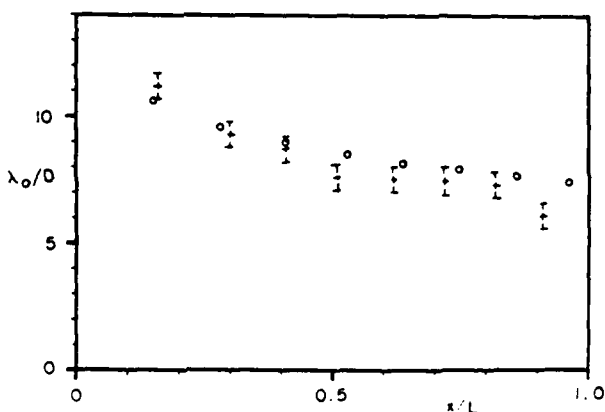


FIG. 8. Plot of  $\lambda_0$  when  $V = 4.43$  m/sec.  $\alpha = 0.008$ ,  $\beta = 62.0$ . All other parameters have the same value as Fig. 7. (+ = experimental value, O = theoretical value.)

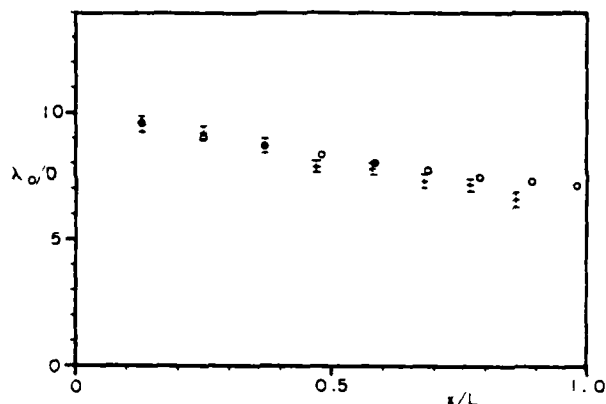


FIG. 9. Plot of  $\lambda_0$  when  $V = 4.56$  m/sec.  $\alpha = 0.005$ ,  $\beta = 75.2$ . All other parameters have the same value as Fig. 7. (+ = experimental value, O = theoretical value.)

tude of the buckled duct, but does not affect its general shape. In addition, we found that a vertical duct exhibits a transition between sinuous and exponential deformation. The location of this transition was found to depend upon the velocity of the fluid stream. We successfully tested our analysis by measuring the buckling wavelength of a long duct and comparing it with the predicted values.

It is important to note that the buckling property of a bounded jet, which has been explored in this paper, is in principle independent of the bending stiffness of the duct which surrounds the jet, because of the inherent jet bending stiffness defined by Eq. (11). In the present paper we have examined the general case where the duct walls have finite bending stiffness. However, a similar buckling phenomenon is observed in jets bounded by ducts with zero bending stiffness, for example, in fast capillary jets<sup>15</sup> and in inviscid jets that discharge freely into an infinite reservoir.<sup>16</sup> In the latter case, the hydrodynamic stability analysis demonstrates that the jet moves as if it were bounded by the annular shear layer which surrounds it, and selects a longitudinal wavelength that is a certain multiple of the jet diameter.<sup>16</sup> This is consistent with the buckling wavelength produced by the  $EI \rightarrow 0$  limit of the present analysis.<sup>11</sup> A compilation of photographs of buckling natural flows is presented in Ref. 17.

From the point of view of experimental methods in turbulence research, the present flexible-duct experiments illustrate an effective way to visualize the natural tendency of any turbulent duct flow to engage in large-scale, organized, motion. As the beam stiffness of the hose decreases, the hose wall molds itself to the large-scale sinuous path preferred by the turbulent jet, and the hose shape becomes a record of the large-scale structure of turbulent jet flow. As pointed out in the Introduction, the search for an effective jet flow visualization method is what led to the definition of the problem addressed in this paper.

#### ACKNOWLEDGMENTS

The contributions of Karl Rupp, Richard Cowgill, and Michael Hacker to the construction of the experimental apparatus are gratefully appreciated.

This research was supported by the Office of Naval Research. Ren Anderson also acknowledges the support received from the University of Colorado in the form of a University Fellowship.

- <sup>1</sup>J. M. T. Thompson, *Instabilities and Catastrophes in Science and Engineering* (Wiley, New York, 1982), p. 166.  
<sup>2</sup>F. I. N. Niordsen, *Trans. R. Inst. Technol., Stockholm* **73** (1953).  
<sup>3</sup>T. B. Benjamin, *Proc. R. Soc. London Ser. A* **261**, 457 (1961).  
<sup>4</sup>T. B. Benjamin, *Proc. R. Soc. London Ser. A* **261**, 487 (1961).  
<sup>5</sup>R. W. Gregory and M. P. Paidoussis, *Proc. R. Soc. London Ser. A* **293**, 512 (1966).  
<sup>6</sup>R. W. Gregory and M. P. Paidoussis, *Proc. R. Soc. London Ser. A* **293**, 528 (1966).

- <sup>7</sup>M. P. Paidoussis, *J. Mech. Eng. Sci.* **12**, 85 (1970).  
<sup>8</sup>R. E. D. Bishop and I. Fawzy, *Proc. R. Soc., Philos. Trans., Math. Phys. Sci.* **284**, 1 (1977).  
<sup>9</sup>T. S. Lundgren, P. R. Sethna, and A. K. Bajaj, *J. Sound Vib.* **64**, 553 (1979).  
<sup>10</sup>J. P. Den Hartog, *Advanced Strength of Materials* (McGraw-Hill, New York, 1949).  
<sup>11</sup>A. Bejan, *Lett. Heat Mass Transfer* **8**, 187 (1981).  
<sup>12</sup>J. P. Den Hartog, *Strength of Materials* (McGraw-Hill, New York, 1949).  
<sup>13</sup>M. Abramowitz and J. A. Stegun, *Handbook of Mathematical Functions* (U.S. Department of Commerce, Washington, D.C., 1972).  
<sup>14</sup>C. M. Bender and S. A. Orszag, *Advanced Mathematical Methods for Scientists and Engineers* (McGraw-Hill, New York, 1978), Chap. 10.  
<sup>15</sup>M. G. Stockman and A. Bejan, *Phys. Fluids* **25**, 1506 (1982).  
<sup>16</sup>R. Anderson, Ph.D. thesis, University of Colorado, Boulder, May 1983.  
<sup>17</sup>A. Bejan, *Entropy Generation through Heat and Fluid Flow* (Wiley, New York, 1982), Chap. 4.



Shigeo Kimura

Adrian Bejan

Department of Mechanical Engineering,  
University of Colorado,  
Boulder, Colo. 80309

## The Buckling of a Vertical Liquid Column

*This paper documents the sinuous flow of a vertical water column which impinges on a horizontal surface. It is shown experimentally that the solid obstacle buckles the column into a plane sinuous (static) shape whose wavelength scales with the local column diameter. The measured ratio (buckling wavelength)/(column diameter) is of order  $\pi/2$ , in agreement with the buckling theory of inviscid flow.*

### 1 Introduction

The object of this paper is to report a series of experimental observations concerning the buckling of a vertical water column, which is a phenomenon commonly observed by placing a flat obstacle under a faucet. The observations reveal the existence of an interesting scaling law, namely, the proportionality between the diameter of the water column and its longitudinal buckling wavelength.

The flow of vertical liquid columns is a topic which draws its importance from its many engineering applications, for example, gas-to-liquid chemical processing and condensation heat transfer in heat exchanger design. As shown below, this topic has been studied extensively, however, with only one exception, all previous studies have been focused on the free-fall of the liquid column: in the free-fall regime the column remains axisymmetric. In the present study we consider a vertical column which is interrupted by an obstacle and, as a result, assumes a sinuous (nonaxisymmetric) shape.

The two-dimensional inviscid flow issuing from a very large vessel through an aperture in a solid wall is one of the classical problems in hydrodynamics, pioneered by Kirchhoff [1] and Rayleigh (see Lamb [2]) Milne-Thomson [3] considered the same phenomenon under the effect of gravity. Since, under gravity, the "infinite height of the vessel leads to an "infinite hydrostatic pressure" paradox, Conway [4] redid the problem by inserting a horizontal lid above the wall with the orifice. He was able to obtain the smooth draw-down shape of the column, employing the free surface treatment proposed by Milne-Thomson [3].

Among the numerous theoretical studies reported in the literature, the work of Scriven and Pigford [5] appears to be the first in which the liquid flow was analyzed based on a boundary layer-type approximation. Lienhard [6] chose a similar approach and included also the effects of gravity and surface tension. Matovich and Pearson [7] formulated a one-dimensional flow model and were able to obtain several closed-form solutions for symmetric column shapes in various parametric domains. A more rigorous formulation was presented by Duda and Vrentas [8]. A one-dimensional Cosserat-type theory was developed by Green [9] and Bogoy [10]. The work of Bogoy is concerned primarily with the

condition of droplet formation at the lower end of a free-falling column. The subject of axisymmetric break-up and droplet formation has been studied extensively over the past 100 years; the core of this work was reviewed recently in the context of Hydrodynamic Stability Theory (Drazin and Reid [11]).

To our knowledge, Lienhard [12] is the only author to have analyzed the sinuous shape of a column impinging on an obstacle. Lienhard viewed the phenomenon as capillary waves which originate at the solid plane and travel upward at the same speed as the water velocity. It is interesting to note that the buckled shape of vertical water columns is sometimes accidentally photographed and published by researchers investigating an unrelated phenomenon (see, for example, Figs. 1(b) and 1(c) in Winston and Martin [13]).

### 2 Experiment

We carried out a series of controlled experiments in which we photographed the buckled shape of the liquid column. The purpose of this photographic record is to document the relationship between the geometry of the buckled column and physical parameters of the flow (velocity, column diameter, column height).

The experimental setup is shown schematically in Fig. 1. The apparatus consists of three basic components, the water supply reservoir, the nozzle, and the round table which interferes with the free-fall of the water column. The water reservoir is a cylindrical vessel (14 cm diameter, 60 cm height) which supplies water at a known flowrate to the nozzle section. The flowrate is known with 5 percent accuracy from preliminary calibration experiments which revealed the relationship between flowrate and reservoir water level. The reservoir and the nozzle are connected through a 1 m long vinyl tube with an inside diameter of 0.64 cm. The nozzle holder was designed to accommodate four different nozzles which produce water columns of varying diameters. As shown in the detail drawing of Fig. 1, in each nozzle the flow is first lead through a wire-mesh section in order to damp out potential disturbances originating from upstream. Water columns of different heights and diameters were established between the nozzle and the round table. Note that the table surface has a slight spherical curvature in order to prevent the irregular accumulation of water right under the column.

Contributed by the Fluids Engineering Division for publication in the JOURNAL OF FLUIDS ENGINEERING. Manuscript received by the Fluids Engineering Division, October 6, 1982.

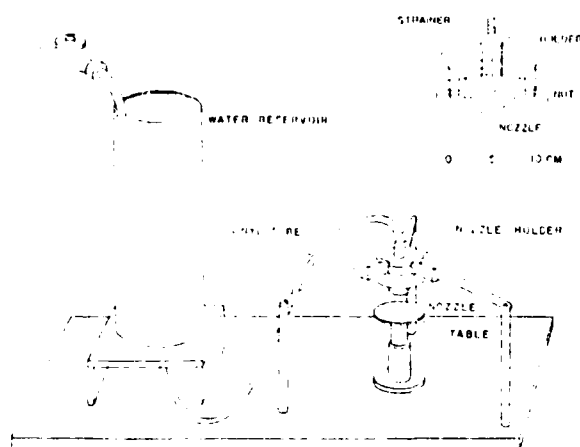


Fig. 1 Experimental apparatus

The parametric domain covered by the experiments is described in terms of two dimensionless groups,

$$W = \frac{\rho u_0^2 r_0}{T}, \text{ the Weber number} \quad (1)$$

$$B = \frac{\rho g r_0^2}{T}, \text{ the Bond number} \quad (2)$$

where  $\rho$ ,  $g$ ,  $u_0$ ,  $r_0$ , and  $T$  represent liquid density, gravitational acceleration, liquid velocity at the nozzle exit, nozzle radius, and water-air surface tension, respectively. We varied the Weber number by changing the flow rate: although the Weber number attained in the experiment depends on nozzle size, it falls consistently in the range of 0.1-4. The Bond number was varied from 0.085 to 1.37 by changing the nozzle size (the four nozzle diameters were 0.159 cm, 0.138 cm, 0.476 cm and 0.635 cm). The Reynolds number based on conditions at the nozzle exit,  $2r_0 u_0 / \nu$ , varied from 450 to 1100. The velocity profile in the water jet immediately below the nozzle was measured recently by Yamaguchi and Takahashi [17]: their Laser-Doppler measurements showed that the velocity profile becomes flat within a longitudinal distance of order  $r_0$  downstream from the nozzle exit. Therefore, in discussing the present experiments it is assumed that the velocity is approximately uniform in each jet cross-section.

Each experimental run was conducted as follows: first, we fixed the two parameters ( $W, B$ ) by selecting a certain nozzle and by keeping the flowrate constant (note that the water reservoir level could be maintained by replenishing the water supply during the run). The table directly under the nozzle was then lowered until a new (additional) elbow was observed in the buckled shape of the column. The height of the table and the counted number of elbows were recorded and a photograph of the column shape was taken. The procedure was repeated for various Weber and Bond numbers.

Representative photographs of the buckled liquid column are shown in Fig. 2. The experimental observations are summarized in Fig. 4, as the total number of elbows vs. the



Fig. 2(a)  $B = 0.34, W = 1.4, z/r_0 = 8.8$

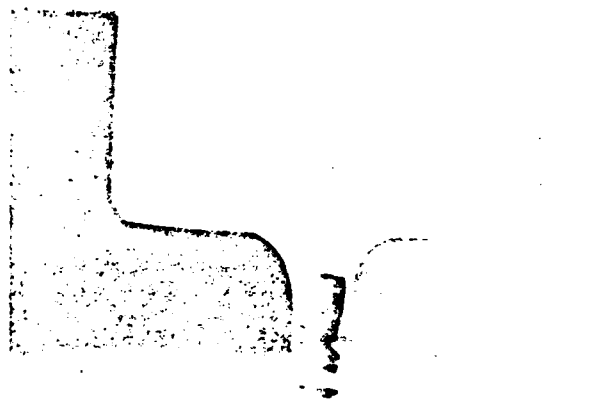


Fig. 2(b)  $B = 0.34, W = 3.65, z/r_0 = 7.68$

Fig. 2 Photographs showing the sinuous shape of buckled liquid columns

dimensionless height of the column  $z = z^*/r_0$ . We learn that in all cases the number of elbows increases almost linearly with the height of the column. This conclusion is of fundamental importance, because it points towards the existence of a *universal proportionality* between column diameter and buckling wavelength.

## Nomenclature

$B$  = Bond number given by  $(\rho g r_0^2)/T$

$D$  = water column diameter

$g$  = gravitational acceleration

$r_0$  = nozzle radius

$Re$  = Reynolds number,  $2r_0 u_0 / \nu$

$T$  = water-air surface tension

$u_0$  = liquid velocity at the nozzle exit

$W$  = Weber number given by  $(\rho u_0^2 r_0)/T$

$z$  = height of the water column

$\lambda$  = buckling wavelength

$\rho$  = density

$\nu$  = kinematic viscosity

## Superscript

\* = dimensional quantity

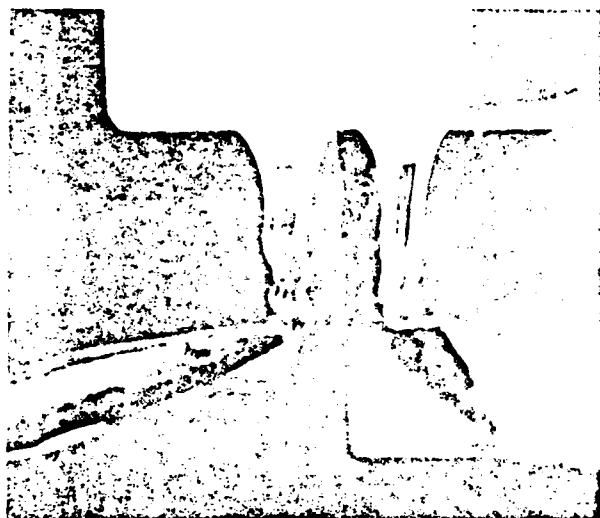


Fig. 3(a)  $B = 0.34$ ,  $W = 0.59$ ,  $z/r_0 = 9.4$



Fig. 3(c)  $B = 0.77$ ,  $W = 1.77$ ,  $z/r_0 = 6.5$



Fig. 3(b)  $B = 0.77$ ,  $W = 1.77$ ,  $z/r_0 = 7.5$

Fig. 3 The plane buckled shape of the liquid column. Left side: the direct view, right side: the side view through the mirror

view appears on the left side, while the mirror (side) view appears on the right side of the photographs. To focus on the column and its mirror image at the same time, the mirror had to be positioned no farther than 1 cm away from the liquid column. As the obstacle we used an asymmetric object, namely, the flat end of a screwdriver. The flat end was positioned so that it is made approximately a 10-degree angle with the horizontal plane (see Figs. 3a-3c).

Figures 3a-3c show very clearly that the liquid column prefers to buckle in a plane. The view from the direction normal to this preferred plane reveals a nearly straight column.

In conclusion, the symmetric (varicose) or asymmetric (sinuous) deformation of the liquid column depends on the degree of asymmetry of the obstacle. If the obstacle is from the side, as in Figs. 3a-3c, then the column buckles into a plane sinuous shape. If, on the other hand, the obstacle is symmetric (i.e., the same when seen from all directions) then the deformation tends to be symmetric also.

### 3 The Two-Dimensionality of the Buckled Shape

An important question arises in connection with the buckled shape of the liquid column: is this shape two-dimensional, i.e., in one plane, as the buckled shape of an elastic rod, or is it helical? In the course of photographing the columns displayed as Figs. 2(a, b), the liquid column exhibited the tendency to buckle in a way which made it visible only from a special direction. Indeed, the camera which recorded Figs. 2(a, b) had to be positioned so that the buckled shape appeared most visibly on film. However, in addition to plane buckling, tall columns showed a tendency to develop an axisymmetric (varicose) deformation at the lower end, near the round table serving as obstacle. It is important to establish whether this axisymmetric deformation is an integral part of the plane buckling phenomenon or simply a reflection of the geometric symmetry imposed by the obstacle on the liquid column.

In order to answer these questions, we conducted an additional series of experimental observations reported here via Figs. 3a-3c. The buckled column was photographed simultaneously from the front and from the side, by using a vertical mirror whose plane made a 45 deg angle with the camera-column direction. In Figs. 3a-3c the direct (front)

### 4 Discussion of Results

The total number of elbows measured experimentally is shown in Figs. 4a-4d. Each figure shows the total number of elbows as a function of column height  $z$  (dimensionless), for various values of  $B$  and  $W$ . In each experiment the Bond number is fixed; it was observed that below a critical Weber number the vertical column breaks up into droplets right under the nozzle, and that the buckled shape is most visible in the range where  $W$  is slightly higher than this critical value. The experimental observations summarized in Figs. 4a-4d have been performed in this optimum range of Weber numbers.

The measurements indicate that the number of elbows of the buckled column increases almost linearly with the height of the column, thus suggesting a local proportionality between buckling wavelength  $\lambda$  and column diameter  $D$ . The Weber number appears to have only a weak influence on the measurements of Figures 4a-4d. The Bond number effect is more noticeable, as the number of elbows for  $z = \text{constant}$  increases as the Bond number  $B$  increases. This dependence is illustrated in Fig. 5.

The proportionality between  $\lambda$  and  $D$  is illustrated further in Figs. 6 and 7. In general, both  $D$  and  $\lambda$  decrease as the

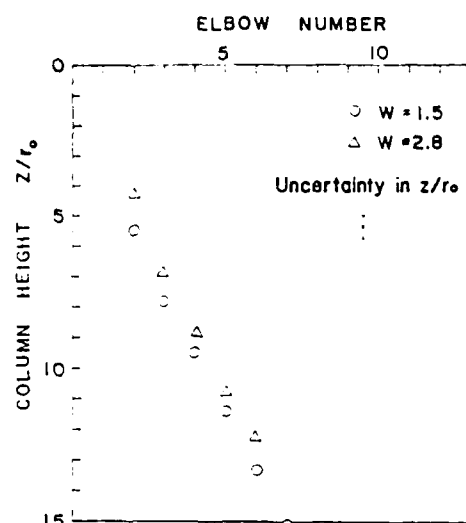


Fig. 4(a)  $B = 0.085 \pm 0.001$  (uncertainty in  $z/r_0 = \pm 0.5$ , in  $W = 1.5 \pm 0.2$ ,  $2.8 \pm 0.3$ )

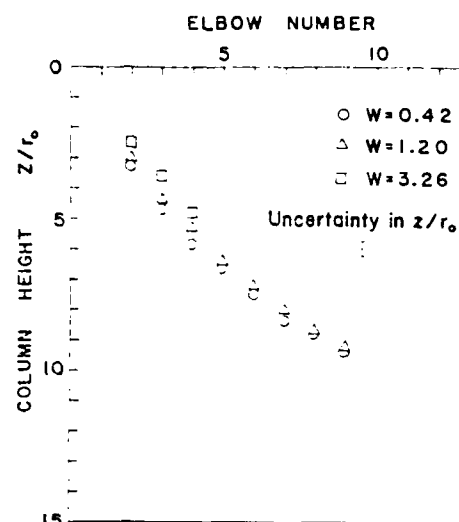


Fig. 4(c)  $B = 0.77 \pm 0.01$  (uncertainty in  $z/r_0 = \pm 0.25$ , in  $W = 0.42 \pm 0.04$ ,  $1.20 \pm 0.12$ ,  $3.26 \pm 0.33$ )

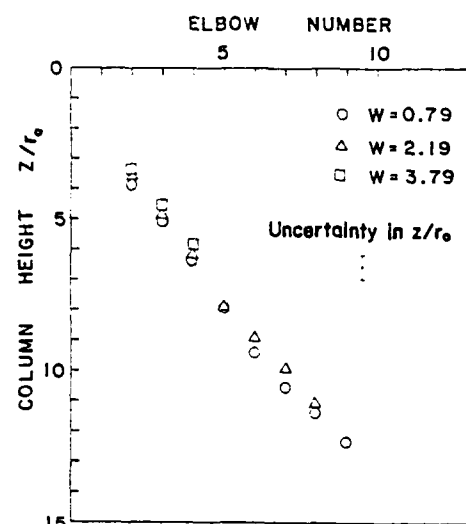


Fig. 4(b)  $B = 0.340 \pm 0.001$  (uncertainty in  $z/r_0 = \pm 0.5$ , in  $W = 0.79 \pm 0.08$ ,  $2.19 \pm 0.22$ )

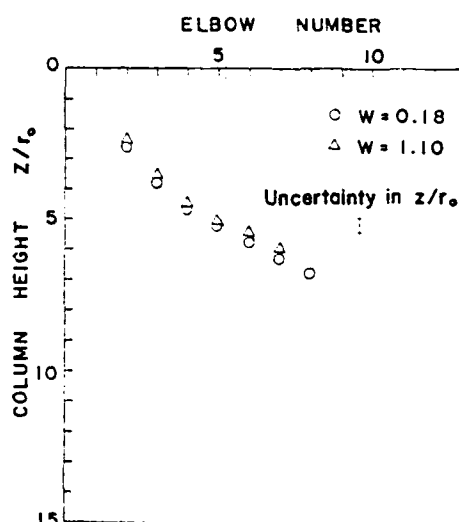


Fig. 4(d)  $B = 1.37 \pm 0.02$  (uncertainty in  $z/r_0 = \pm 0.25$ , in  $W = 0.18 \pm 0.02$ ,  $1.10 \pm 0.11$ )

Fig. 4 Total number of elbows as a function of column height

water column is accelerated downward (Figs. 2, 3) however, the measured ratio  $\lambda/D$  appears to be independent of the vertical position along the column (Fig. 6). For this reason, in Figure 7 we show only the  $\lambda/D$  measurements taken from the upper section of each column, where the first buckling takes place. The  $\lambda/D$  ratio is largely insensitive to changes in both Weber number and Bond number. Indeed, in the  $W$ - $B$  range documented by our experiments, the wavelength/diameter ratio appears to be a universal constant of order 1.5. Figure 7 shows also Lienhard's [12] theoretical curve and  $\lambda/D$  measurements for the axisymmetric (varicose) deformation: note that Lienhard's data merge with the present measurements in the vicinity of  $W=0(1)$ , and that Lienhard's theoretical wavelength of the varicose shape appears to be consistent with both sets of data. However, Lienhard's theory does not account for the sinuous (nonaxisymmetric) shape documented by the present experiments, nor does it account for the apparent constancy of the  $\lambda/D$  ratio of buckled (sinuous) shapes.

We feel that the universal proportionality between buckling wavelength and column diameter is of fundamental interest for the following reasons. First, a similar  $\lambda$ - $D$  proportionality is also exhibited by highly viscous fluid filaments, such as honey and corn syrup falling and folding on a horizontal surface (see the photographs of Cruickshank [14] and Cruickshank and Munson [15], where the folding wavelength is greater when the filament is thicker; the same scaling is revealed while experimenting with honey filaments of increasing thickness). The present experiments demonstrate that the buckling phenomenon and the  $\lambda$ - $D$  scaling law are not restricted to highly viscous columns, as originally thought, rather, they are observed even when "inviscid" fluid columns impinge on an obstacle. The buckling of inviscid columns was linked theoretically to the origin of turbulence [16]. Thus, the present measurements confirm not only the possibility of "buckling" in inviscid jets, predicted theoretically [16], but also the accuracy of the theoretical buckling wavelength,  $\lambda/D = \pi/2 = 1.57$  [16].

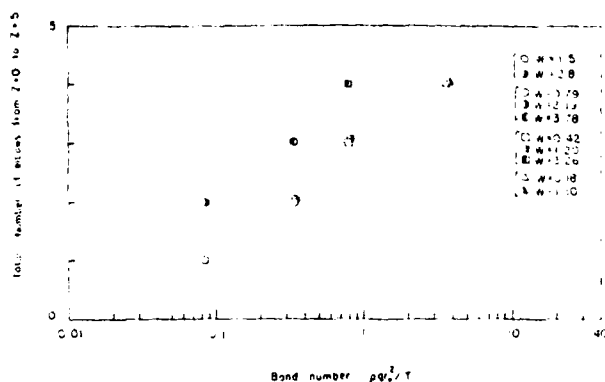


Fig. 5 The effect of Bond number on the total number of elbows over a fixed height

Finally, the agreement between the buckling theory of reference [16] and the  $\lambda/D$  data of Fig. 7 is thought-provoking, because the theory neglects the effect of surface tension, while the  $W=0(1)$  data correspond to cases where the surface tension effect is not negligible. At this stage, the agreement between theory and experiment suggests only that surface tension is not a major consideration in "buckling" (i.e., in the rotational equilibrium condition of a nearly straight column [16]). Whether or not this suggestion is correct can be decided by including surface tension in the buckling theory (this remains to be done) and by extending the present experiments to document the Weber number domain below  $W=0(1)$ . Note that recent experiments with fast capillary jets in the high Weber number range  $10^2 - 10^4$  [18] support the buckling theory of inviscid jets [16, 19].

### Acknowledgment

This research was conducted under the auspices of the Office of Naval Research. The experimental apparatus was constructed by Mr. Karl Rupp.

### References

- Kirchhoff, G., "Zur Theorie freier Flüssigkeitsstrahlen," *J. Grelle LXX*, 1896, pp. 289-298.
- Lamb, Sir Horace, *Hydrodynamics*, Cambridge University Press, 1932, pp. 98-99.
- Milne-Thomson, L. M., *Theoretical Hydrodynamics*, 5th ed. Macmillan Company, 1968.
- Conway, W. E., "The Two-Dimensional Jet Under Gravity from an Aperture in the Lower of Two Horizontal Planes which Bounds a Liquid," PhD thesis, University of Arizona, 1965.
- Scriven, L. E., and Pigford, R. L., "Fluid Dynamics and Diffusion Calculations for Laminar Liquid Jets," *AIChE Journal*, Vol. 5, 1959, pp. 397-402.
- Lienhard, J. H., "Effects of Gravity and Surface Tension upon Liquid Jets Leaving Poiseuille Tubes," *ASME Journal of Basic Engineering*, Vol. 90, 1968, pp. 262-268.
- Matovich, M. A., and Pearson, J. R. A., "Spinning a Molten Threadline," *Industrial and Engineering Chemistry Fundamentals*, Vol. 8, 1969, pp. 512-520.
- Duda, J. L., and Vrentas, J. S., "Fluid Mechanics of Laminar Liquid," *Chemical Engineering Science*, Vol. 22, 1967, pp. 855-869.
- Green, A. E., "On the Non-linear Behavior of Fluid Jets," *International Journal of Engineering Science*, Vol. 14, 1976, pp. 49-63.
- Bogy, D. B., "Steady Draw-down of a Liquid Jet under Surface Tension and Gravity," *Journal of Fluid Mechanics*, Vol. 105, 1981, pp. 157-176.
- Drazin, P. G., and Reid, W. H., *Hydrodynamic Stability*, Cambridge University Press, 1981.
- Lienhard, J. H., "Capillary Action in Small Jets Impinging on Liquid Surfaces," *ASME Journal of Basic Engineering*, Vol. 90, 1968, pp. 137-138.
- Winton, R., and Martin, H. R., "A Theoretical Model for the Transverse Impingement of Free Jets at Low Reynolds Numbers," *ASME Journal of Fluids Engineering*, Vol. 102, 1981, pp. 510-518.
- Cruickshank, J. O., "Viscous Fluid Buckling: A Theoretical and Experimental Analysis with Extensions to General Fluid Stability," PhD thesis, Iowa State University, 1980.
- Cruickshank, J. O., and Munson, B. R., "Viscous Fluid Buckling of Plane and Axisymmetric Jets," *Journal of Fluid Mechanics*, Vol. 113, 1981, pp. 221-239.
- Bejan, A., "On the Buckling Property of Inviscid Jets and the Origin of Turbulence," *Letters in Heat and Mass Transfer*, Vol. 8, 1981, pp. 187-194.
- Yamaguchi, R., and Takahashi, K., "Flow Pattern near the Outlet of a Straight Long Circular Tube," *Bull. of the JSME*, Vol. 23, No. 185, Nov. 1980, pp. 1798-1805.
- Stockman, M. G., and Bejan, A., "The Nonaxisymmetric (Buckling) Flow Regime of Fast Capillary Jets," *Physics of Fluids*, Vol. 25(9), 1982, pp. 1506-1511.
- Bejan, A., *Entropy Generation through Heat and Fluid Flow*, Wiley, New York, 1982, Chapter 4.

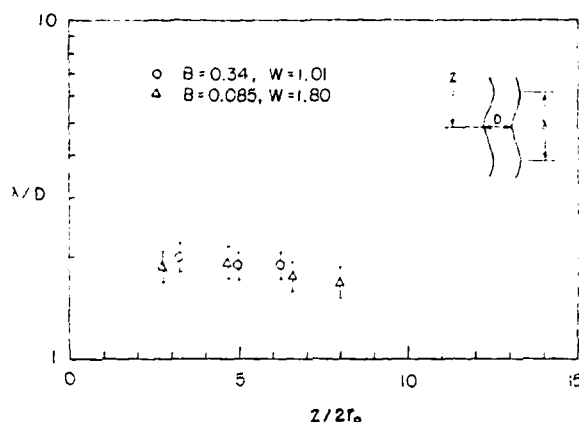


Fig. 6 Variation of  $\lambda/D$  with vertical position (uncertainty in  $\lambda/D = 10$  percent in  $B = 0.34 \pm 0.004$ ,  $0.085 \pm 0.001$ , in  $W = 1.01 \pm 0.05$ ,  $1.80 \pm 0.09$ )

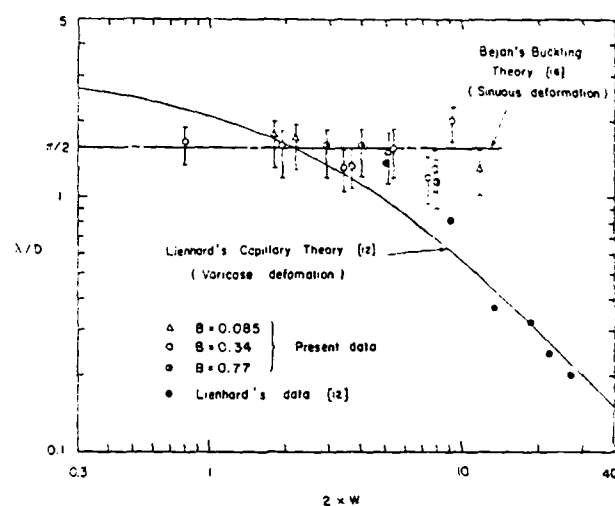


Fig. 7 Comparison of the present results with Lienhard's capillary theory. Note: In order to make the present results comparable with Lienhard's study, in this figure the Weber number is based on local jet radius and local jet velocity (uncertainty in  $\lambda/D = \pm 20$  percent, in  $W = \pm 20$  percent, in  $B = 0.77 \pm 0.01$ ,  $0.34 \pm 0.01$ ,  $0.085 \pm 0.001$ )

# Experiments on the Buckling of Thin Fluid Layers Undergoing End-Compression

K. R. Blake

A. Bejan

Department of Mechanical Engineering,  
University of Colorado,  
Boulder, Colo. 80309

*This paper reports a series of experiments concerning the buckling of a slender fluid layer in a state of longitudinal compression. The experiments consist of floating a layer of highly viscous oil on a pool of water and, manually, compressing the layer from the side. Photographs of the buckled layer show conclusively that the buckling wavelength is largely insensitive to either the rate of compression or the viscosity of the fluid layer. The observations suggest that the buckling wavelength is actually a characteristic length scale (a property) of the fluid layer, in contrast with the buckling theory of purely viscous layers (Buckmaster, Nachman, and Ting, [7]) where the buckling wavelength remains to be determined randomly by initial disturbances.*

## 1 Introduction

The concept of "fluid buckling" is relatively new in fluid mechanics research: during the past decade it has been used with increasing frequency to account theoretically for a number of flow phenomena, the explanation of which appears to shed new light on the theoretical origins of turbulence (Cruickshank [1], Bejan [2], Munson [3]). In the present paper, the buckling concept is used to describe a series of experimental observations of how a sheet of viscous fluid wrinkles as it is compressed from one end. As shown in Fig. 1, the fluid buckles and assumes a sinusoidal shape with characteristic wavelength  $\lambda$ . The objective of this experiment is to measure the buckling wavelength and to learn how this wavelength is influenced by the geometry (slenderness) of the fluid layer, the fluid properties and the rate of compression.

The buckling of highly viscous fluids was first studied by Biot [4]. In a series of papers, Biot developed the equations to describe the buckling of a multilayered viscous fluid. The equations were solved and were shown to be unstable when the viscous layers were subjected to an arbitrary finite strain with a small perturbation superimposed on the initial state. Solutions were determined numerically and were found to agree with solutions given by the theory of elasticity and viscoelasticity when the instability was of a significant magnitude. Biot's work was motivated by applications to the problems of tectonic folding of stratified geological structures.

The instability of jets, threads, and sheets of viscous fluids was studied qualitatively by Taylor [5]. In his paper, Taylor argues that the instability created by the compression of viscous fluids is the same as the Euler buckling of solid columns. Of the many experiments he conducts, two are

especially relevant to the work presented here. In one, Taylor compresses a thread of an extremely viscous fluid floating on mercury and compares the resultant shape with the shapes of elastica under compression as calculated by Love [6]. The other experiment was designed to determine when a sheet of a viscous fluid under compression would become unstable.

With Taylor's experimental results in mind, Buckmaster, Nachman, and Ting [7] considered theoretically the buckling of a thin viscous layer (the *viscida* problem). The problem was that of a two-dimensional *viscida* immersed in vacuum, whose ends are moved together slowly so that inertia terms could be neglected. Since their analysis was not limited to small deformations, it was a generalization of Biot's work. They derived a *global* equation for the evolution of the slope of the centerline as a function of time and distance from one end, by integrating the momentum equations over the thickness of the viscous layer. This equation was then solved using asymptotic expansions for the case of small centerline deviation. Based on these results the solutions for large centerline deviations were found numerically. The case where surface tension effects cannot be neglected was incorporated into this theory by Buckmaster and Nachman [8] in a subsequent paper.

In a more recent paper, Suleiman and Munson [9] investigated the buckling of a thin viscous fluid layer subjected to linear shear. They found that if the dimensionless shear stress exceeded a critical value, the layer would buckle in a manner similar to the buckling of a thin elastic plate. In another study, Munson [10] examined experimentally the buckling of a falling viscous jet flowing out of a vertical slit orifice onto a horizontal plate. In this experiment Munson observed that the jet sometimes buckles in a manner similar to the buckling of a cantilever beam. Another experimental study was conducted by Cruickshank and Munson [11] on the spontaneous oscillations of a falling viscous jet flowing from a horizontal orifice onto a flat plate. They determined the

Contributed by the Fluids Engineering Division for publication in the JOURNAL OF FLUIDS ENGINEERING. Manuscript received by the Fluids Engineering Division, February 8, 1983.

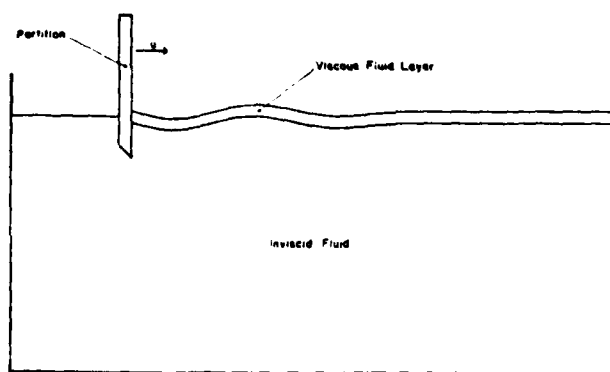


Fig. 1 The buckling of a thin viscous layer floating on top of a heavier inviscid fluid

minimum distance from the jet orifice to the flat plate for which the jet would buckle (termed the "buckling height") as a function of fluid and flow variables. They found that if the flow exceeded a critical Reynolds number, the jet does not buckle. Below this critical Reynolds number, surface tension becomes the dominant factor in influencing the buckling height. The origin of buckling was attributed to the jet flow transition from tension in the falling stage, to compression in the deceleration stage when the jet strikes the plate.

Commenting on Suleiman and Munson's paper, Bejan [2] noted that the buckling phenomenon is not only a property of highly viscous fluids, but also a property of inviscid columns (streams), and, as such, explains the "meander" phenomenon. The process of inviscid stream buckling was treated analytically by Bejan [12] who showed that all inviscid fluid layers buckle so that the wavelength is proportional to the layer thickness only. The proportionality between buckling wavelength and jet diameter was verified recently in two separate experiments, one involving the meandering of air streams driven by falling paper ribbons (Bejan [13]) and the other focusing on the buckled shapes of fast capillary jets (Stockman and Bejan [14]).

At this stage in our understanding of fluid buckling, an important discrepancy exists between the observed buckling behavior of viscous layers and the behavior predicted by the viscida theory [7]. The theoretical wavelength of the buckled shape is indeterminate and, presumably, dictated randomly by the original deformation (disturbance) of the straight layer. Experimental observations, on the other hand, seem to suggest that the buckling wavelength is not random [1, 5, 11]. Thus, the objective of the experimental work described in this paper is to establish whether the buckling wavelength of viscous layers is indeterminate, as in the viscida theory, or, in fact, a "characteristic" length. The experiment does not correspond fully to the geometry of Taylor [5] or Buckmaster et al. [7, 8], however, it does shed light on the uniqueness of the observed buckling wavelength.

## 2 Experiment

The experiment was designed to measure the buckling wavelength of a viscous fluid layer and to determine quantitatively what parameters affect the wavelength. The experiment is shown schematically in Fig. 1. A layer of viscous fluid, floating on a relatively inviscid fluid, is compressed by the partition. The partition extends into the inviscid fluid a distance on the order of the viscous layer's thickness and has a rate of compression  $u$ . The geometrical shape of the layer is given by the slenderness ratio  $L/d$  where  $L$  and  $d$  are the length and thickness of the unbuckled layer. The slenderness ratio was varied from about 20 to 70 by changing the thickness of the layer and leaving the length constant.

The experiment was carried out in an aluminum box with

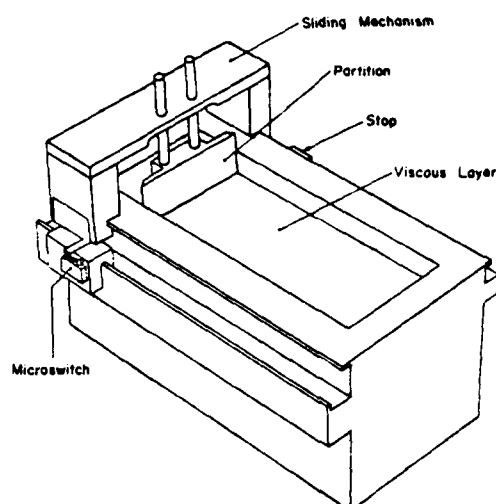


Fig. 2 Construction details of the experimental apparatus

inside dimensions measuring 20.3 cm in length, 7.6 cm in width and 10.2 cm in depth. The sides of the box serve as a track for a sliding mechanism carrying a partition (gate) which can be lowered into the box (see Fig. 2). It is by means of this partition that the layer is compressed. The sliding mechanism was designed to operate without vibrations and to hold the partition perpendicular to the viscous fluid layer and to the walls on each side. It also holds the partition in contact with the side walls preventing the fluid layer from escaping behind the partition as the viscous layer is compressed.

The sliding mechanism was moved by hand; in order to bring uniformity to the results, two stops were positioned to set the initial length  $L$  and to control the maximum excursion of the partition. As the sliding mechanism moved between the stops, it passed over a microswitch sending an electrical pulse to a timer and, at the same time, triggering the camera. The duration of the pulse was used to make a time of flight measurement, and with the assumption that the partition undergoes a constant acceleration, it was possible to determine the rate of compression at any instant. The accuracy of the velocity measurement is determined by the constant acceleration assumption. Since the compression stroke is very short (13 to 32 milliseconds) and the force applied by hand during that interval is approximately constant, the acceleration is also approximately constant.

Experiments were run to determine the effects of the excursion length and rate of compression on the buckling wavelength. In varying the excursion length, it was found that there exists an optimum range of lengths for the most accurate portrayal of the buckling phenomenon. This range was from 1 cm to 2 cm. If the excursion length was less, there was no visible buckling, and if it was greater, the buckling became so pronounced that the "waves" would collide. The effect of the rate of compression is discussed in greater detail in the next section.

It is important to note that although the buckled layer has the appearance of a propagating gravity wave, it is not. This is demonstrated by the observation that after the partition has stopped, the buckled shape remains stationary. In time, the amplitude decreases and eventually the layer reaches equilibrium again. In many cases the buckled shape and its wavelength remained visible and could be photographed for up to 30 minutes after the compression stroke. As shown in section 4, the observation that the amplitude of the buckled shape decreases away from the moving partition (Figs. 3, 4) can be explained by the fact that the layer is not uniformly compressed. The nonuniform compression rate can be due to



Fig. 3 Photograph showing the buckled layer as seen from above (the partition moves from left to right)

the no-slip condition along the side wall, or to the inertia of the fluid layer itself.

The buckling wavelength was measured photographically using a camera triggered by the trailing edge of the pulse created by the microswitch. Special lighting conditions were needed in order to make the buckling wavelength easy to measure on the photographs (Blake [15]). This system enabled one side of a "wave crest" to be illuminated while leaving the other side in darkness. The photograph then contained a series of light and dark bands where one light and one dark band together account for one wavelength. The sample photograph shown in Fig. 3 has three bands, implying that the buckled region extended one and one half wavelengths into the viscous fluid layer. The other photographs contained between two and five bands (see also Fig. 4).

In all the experiments involving data acquisition, Dow Corning 200 silicone oil was used as the viscous fluid and distilled water as the inviscid substance. The silicone oil has several desirable attributes such as its small variation in viscosity with temperature, its low surface tension, its immiscibility with water, and its availability over a wide range of high viscosities. In addition, any intermediate viscosity can be achieved simply by mixing a higher and lower viscosity in the proper proportions. Since, as shown in the next section, the buckling wavelength is not strongly dependent on viscosity, it was not necessary to know the precise viscosity, therefore, the oil viscosity reported in these experiments is the viscosity calculated based on Dow Corning information. Furthermore, the experiments were run at room temperature, which is within a few degrees of the temperature (75°F) at which the viscosity was measured. The viscosity of the silicone oil used in the experiments ranged from  $10^3$  to  $10^5$  centistokes (cSt) where one centistoke is approximately the viscosity of water and the units of stokes are centimeters squared per second. Lastly, the silicone oil was demonstrated to be a Newtonian fluid by Suleiman and Munson [9].

To set up the experiment, a flat, uniform layer of the viscous fluid, of a prescribed thickness, must be placed on the surface of the water. The method used was to put the silicone oil in a standard 100 ml buret with the following modifications: the tapered end of the buret was ground off, and the hole in the valve was drilled out to be the same size as the tube. The buret was held about a centimeter above the surface of the water and the oil was allowed to drain out until the desired thickness was obtained. Depending on the viscosity, it took from one to five hours to drain out the required amount. This extremely slow pouring rate allowed the oil to slowly creep across the surface of the water providing a flat, smooth layer. Knowing the volume of oil and the area of the layer, the thickness  $d$  could be calculated to an

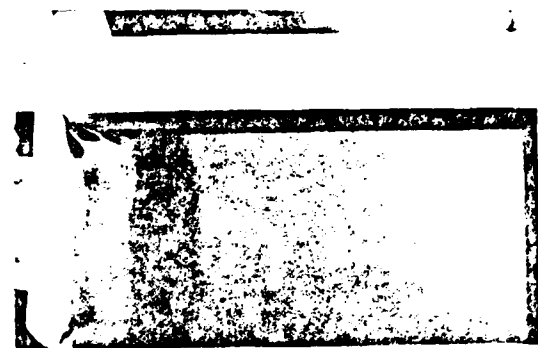


Fig. 4(a)  $d = .394 \pm .003$  cm,  $L = 16.35 \pm .03$  cm,  $u = 42.3 \pm .2$  cm/s,  $\nu = 10^4 \pm 400$  cSt



Fig. 4(b)  $d = .264 \pm .003$  cm,  $L = 16.35 \pm .03$  cm,  $u = 32.6 \pm .2$  cm/s,  $\nu = 10^5 \pm 4000$  cSt

Fig. 4 Two separate experimental runs:

accuracy of 0.003 cm with most of the error resulting from the meniscus on the edges of the oil layer.

Since the experiment sometimes took days to run, de-aerated (distilled) water was needed for the lower fluid. Otherwise bubbles of air would form under the layer of oil creating little bumps in the surface.

#### 4 Results

Despite the fact that in the present experiment the motion of the position is not mechanized, it is important to document the effect of changes in the rate of compression  $u$ . It is also important to report the minimum rate of compression necessary for buckling the layer. Referring to buckling in a purely two-dimensional layer geometry, Taylor [5] stated that when

$$-4\mu\epsilon d - T > 0 \quad (1)$$

the viscous sheet is unstable to disturbances of any wavelength, where  $\mu$  and  $\epsilon$  are the viscosity and the rate of strain. The total surface tension  $T$  is the sum of the oil-air interface  $T_{oa}$  and the water-oil interface  $T_{wo}$ . For two im-



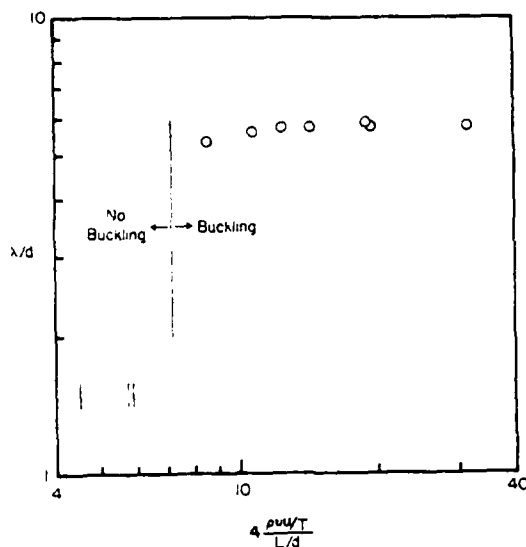


Fig. 5 The weak dependence between buckling wavelength ( $\lambda$ ) and rate of compression ( $u$ ). (Uncertainty in  $\lambda/d = \pm 0.08$ , in  $4(\rho vu/T)/(L/d) = \pm 0.06$  at 20:1 odds)

miscible liquids, the value of  $T_{wa}$  is approximately  $T_{wa} - T_{oa}$ , where  $T_{wa}$  is the surface tension of the water-air interface (Suleiman and Munson [9], Davies and Rideal [16]). Therefore,  $T = T_{oa} + (T_{wa} - T_{oa}) = T_{wa}$ , that is, the total surface tension  $T$  is just the surface tension of the water-air interface. Upon substituting  $-u/L$  for  $\epsilon$  in Taylor's equation and rearranging, it is found that the layer buckles when

$$4(\rho vu/T)/(L/d) > 1 \quad (2)$$

It should be noted that Taylor's conclusions do not apply exactly to the present experiment. As shown in Figs. 3 and 4, the no-slip condition along the side walls gives rise to a three-dimensional flow such that only the middle portion of the buckled layer shows parallel waves and can be regarded approximately as two-dimensional. Therefore, the substitution  $\epsilon = -u/L$  used to derive equation (2) can only be approximately valid. That  $-u/L$  is not the rate of strain everywhere in the layer is demonstrated by the fact that buckling does not occur throughout the layer but only near the compressed end. Figures 3 and 4 show that sufficiently close to the partition, the bands (waves) are relatively constant size, hence, it is reasonable to assume that in that region the rate of strain is relatively constant. In cases where the photographed bands are unequal in size, the reported wavelength was calculated by averaging the first two bands.

For this experiment the viscous fluid layer had a slenderness ratio ( $L/d$ ) of 25, a viscosity ( $\nu$ ) of  $3 \times 10^3$  cSt, a density ( $\rho$ ) of  $0.975 \text{ g/cm}^3$ , and a surface tension ( $T$ ) of  $72.8 \text{ dyne/cm}$ . The results of the experiment are given in terms of the buckling wavelength to thickness ratio  $\lambda/d$  versus  $4(\rho vu/T)/(L/d)$  and graphed as shown in Fig. 5. The data fall into two categories: points where the fluid buckled and points where the fluid did not. The cases in which buckling did not occur have no  $\lambda/d$  value and are indicated with short vertical lines at the bottom of the graph. The large vertical line indicates the approximate minimum value of  $4(\rho vu/T)/(L/d)$  that will buckle the layer. This value is approximately 7, i.e., greater than the value 1 appearing in equation (2) derived from Taylor's buckling criterion (1). This discrepancy is not surprising in view of the three-dimensional effects and nonuniform  $\epsilon$  that distinguish the present experiment from Taylor's two-dimensional geometry.

An important result of the present experiment is the independence of  $\lambda/d$  on the rate of compression, as witnessed

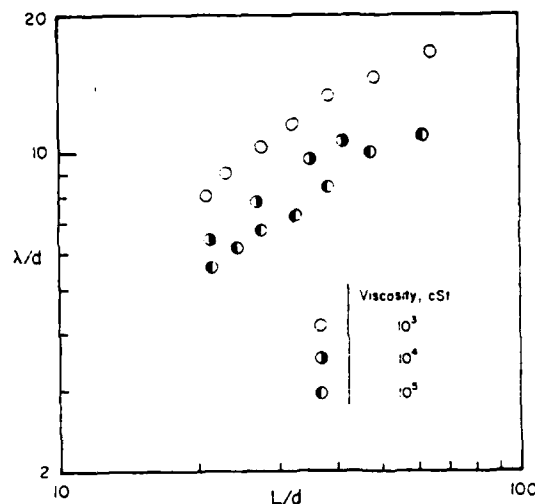


Fig. 6 The relationship between buckling wavelength ( $\lambda$ ) and both length to thickness ratio ( $L/d$ ) and viscosity ( $\nu$ ). (Uncertainty in  $\lambda/d = \pm 0.06$ , in  $L/d = \pm 0.01$ , in  $\nu = \pm 0.04$  at 20:1 odds.)

by the nearly horizontal distribution of the data on Fig. 5. The data was limited on the right by the inability to compress the layer at a faster rate. This conclusion is further supported by the results given in Fig. 6 where each datum is an average obtained from three different rates of compression. In each set of three, the group  $4(\rho vu/T)/(L/d)$  varies with an average 55 percent increase from the smallest to the largest value. However, the corresponding values of  $\lambda/d$  only have an average 5 percent increase, as indicated approximately by the size of the circles. Thus for a variety of  $L/d$  ratios and viscosities it can be seen that the sizable change in  $4(\rho vu/T)/(L/d)$  has only a marginal, if any, effect on  $\lambda/d$ .

To determine the relationship between the buckling wavelength and the slenderness ratio, a series of experiments were conducted varying the thickness of the layer and using different viscosity oils. The data were obtained in the following manner. The partition was placed at the maximum distance from the far end so that  $L = 16.4 \text{ cm}$ . The box was filled with water and then a thin layer of oil was poured onto the water surface from the buret. To obtain different slenderness ratios more oil was added from the buret, and allowed to reach equilibrium. For each slenderness ratio the layer was usually compressed three times. Between each compression the partition was moved back to its initial position and the oil layer was given enough time to reach equilibrium again. For each change in viscosity, the buret was drained of the previous oil and the new viscosity oil was poured in.

The results of these experiments are graphed as  $\lambda/d$  versus  $L/d$  in Fig. 6. The plot contains three sets of points indicated by an open circle and right and left half-filled circles for viscosities of  $10^3$  cSt,  $10^4$  cSt, and  $10^5$  cSt, respectively. It is clear from Fig. 4 that  $\lambda/d$  is dependent on  $L/d$ . For  $L/d$  less than 40 the slopes of the curves are almost unity, indicating that  $\lambda$  is proportional to  $L$ . Due to the construction of the experimental apparatus, the value of  $L/d$  could not be increased beyond 65.

The effect of viscosity on the buckling wavelength can also be interpreted from the data in Fig. 6. The value of  $\lambda/d$  decreases by about one-third when changing the viscosity from  $10^3$  cSt to  $10^5$  cSt and keeping  $L/d$  constant. This change is fairly consistent throughout the range of values of  $L/d$ . Within this range, then, the effect of viscosity on  $\lambda/d$  is seen to be very slight.

The error in the results presented here is governed primarily by the measured value of  $\lambda$ . The variables  $d$ ,  $L$ , and  $u$  have all

been calculated to within 1 percent. The other variables influencing the results, although unknown precisely, remain constant throughout each experiment and therefore do not effect the overall trends shown in the graphs.

## 5 Conclusions

The object of this experimental report has been to present a series of observations concerning the buckling wavelength of a highly viscous fluid layer undergoing end-compression. The motivation for designing and running these experiments stemmed from the unresolved issue of whether the buckling wavelength is arbitrary (as in the *viscida* theory, Buckmaster et al. [7]), or a characteristic length of the layer. Based on the measurement produced by the present study, the following conclusions may be drawn:

1 In a fluid layer of fixed geometry and viscosity, the buckling wavelength is practically independent of the rate of compression, that is, independent of the layer velocity relative to the fluid ambient (Fig. 5).

2 The viscosity of the buckled layer has only a minor impact on the buckling wavelength (Fig. 6).

3 In the range  $L/d < 100$  the buckling wavelength  $\lambda$  scales with the length of the compressed layer,  $L$  (Fig. 6).

In view of these findings, the wavelength of a buckled viscous layer emerges as a property of the layer (a characteristic length), as opposed to the undetermined length dictated by random initial disturbances assumed in the *viscida* theory.

## Acknowledgment

This research was supported by the Office of Naval

Research. The experimental apparatus and the instrumentation were constructed by Mr. Karl A. Rupp, Michael Hacker and Mr. Richard C. Cowgill.

## References

- 1 Cruickshank, J. O., "Viscous Fluid Buckling: A Theoretical and Experimental Analysis with Extensions to General Fluid Stability," PhD thesis, Iowa State University, 1980.
- 2 Bejan, A., "Comments on 'Viscous Buckling of Thin Fluid Layers'," *Phys. Fluids*, Vol. 24, 1981, p. 1764.
- 3 Munson, B. R., "Reply to the Comment by A. Bejan," *Phys. Fluids*, Vol. 24, 1981, p. 1766.
- 4 Biot, M. A., "Theory of Viscous Buckling of Multilayered Fluids Undergoing Finite Strain," *Phys. Fluids*, Vol. 7, 1964, p. 855.
- 5 Taylor, G. I., "Instability of Jets, Threads, and Sheets of Viscous Fluids," *12th Intl. Congr. Appl. Mech.*, Stanford, 1968 (Berlin: Springer-Verlag, 1969), p. 543.
- 6 Love, A. E. H., *A Treatise on the Mathematical Theory of Elasticity*, 4th Ed., Dover, New York, 1944, p. 404.
- 7 Buckmaster, J. D., Nachman, A., and Ting, L., "The Buckling and Stretching of a Viscida," *J. Fluid Mech.*, Vol. 69, Part I, 1975, p. 1.
- 8 Buckmaster, J. D. and Nachman, A., "The Buckling and Stretching of a Viscida," *Q. J. Mech. Appl. Meth.*, Vol. 7, Part II, 1978, p. 157.
- 9 Suleiman, S. M. and Munson, B. R., "Viscous Buckling of Thin Fluid Layers," *Phys. Fluids*, Vol. 24, 1981, p. 1.
- 10 Munson, B. R., "Viscous Buckling of Slender Horizontal Jets," *Phys. Fluids*, Vol. 24, 1981, p. 1780.
- 11 Cruickshank, J. O., and Munson, B. R., "Viscous Fluid Buckling of Plane and Axisymmetric Jets," *J. Fluid Mech.*, Vol. 113, 1981, p. 221.
- 12 Bejan, A., "On the Buckling Property of Inviscid Jets and the Origin of Turbulence," *Letters in Heat and Mass Transfer*, Vol. 8, 1981, p. 187.
- 13 Bejan, A., "The Meandering Fall of Paper Ribbons," *Phys. Fluids*, Vol. 25, 1982, p. 741.
- 14 Stockman, M., and Bejan, A., "The Nonaxisymmetric (Buckling) Flow Regime of Fast Capillary Jets," *Phys. Fluids*, Vol. 24, 1982.
- 15 Blake, K. R., "Viscous Buckling of Thin Fluid Layers Undergoing End Compression," Master's thesis, University of Colorado, Boulder, 1982.
- 16 Davies, J. T., and Rideal, E. K., *Interfacial Phenomena*, Academic Press, New York, 1961.

DISTRIBUTION LIST

HEAT TRANSFER

One Copy except  
as noted

Mr. M. Keith Ellingsworth  
Mechanics Division  
Office of Naval Research  
800 N. Quincy Street  
Arlington, VA 22203

2

Defense Documentation Center  
Building 5, Cameron Station  
Alexandria, VA 22314

12

Technical Information Division  
Naval Research Laboratory  
4555 Overlook Avenue SW  
Washington, DC 20375

6

Professor Paul Marto  
Department of Mechanical Engineering  
U.S. Naval Post Graduate School  
Monterey, CA 93940

Professor Bruce Rankin  
Naval Systems Engineering  
US Naval Academy  
Annapolis, MD 21402

Mr. Doug Marron  
Code 05R13  
Crystal Plaza # 6  
Naval Sea Systems Command  
Washington, DC 20362

Steam Generators Branch, Code 5222  
National Center #4  
Naval Sea Systems Command  
Washington, D.C. 20362

Heat Exchanger Branch, Code 5223  
National Center #3  
Naval Sea Systems Command  
Washington, D.C. 20362

Mr. Ed Ruggiero, NAVSEA 08  
National Center #2  
Washington, D.C. 20362

Dr. Earl Quandt Jr., Code 272  
David Taylor Naval Ship R&D Center  
Annapolis, MD 21402

Mr. Wayne Adamson, Code 2722  
David Taylor Naval Ship R&D Center  
Annapolis, MD 21302

Dr. Win Aung  
Heat Transfer Program  
National Science Foundation  
Washington, DC 20550

Mr. Michael Perlsweig  
Department of Energy  
Mail Station E-178  
Washington, DC 20545

Dr. W.H. Theilbahr  
Chief, Energy Conservation Branch  
Dept. of Energy, Idaho Operations Office  
550 Second Street  
Idaho Falls, Idaho 83401

Professor Ephriam M. Sparrow  
Department of Mechanical Engineering  
University of Minnesota  
Minneapolis, MN 55455

Professor S.V. Patankar  
Department of Mechanical Engineering  
University of Minnesota  
Minneapolis, MN 55455

Professor Daryl Metzger  
Chairman, Mechanical and  
Energy Systems Engineering  
Arizona State University  
Tempe, AZ 85281

Professor Ronald So  
Mechanical and Energy Systems  
Engineering  
Arizona State University  
Tempe, AZ 85281

Professor J.A.C. Humphrey  
Department of Mechanical Engineering  
University of California, Berkeley  
Berkeley, CA 94720

Professor Brain Launder  
Thermodynamics and Fluid Mechanics Division  
University of Manchester  
Institute of Science & Technology  
PO88 Sackville Street  
Mandhester M601QD England

Professor Shi-Chune Yao  
Department of Mechanical Engineering  
Carnegie-Mellon University  
Pittaburgh, PA 15213

Professor Charles B. Watkins  
Chairman, Mechanical Engineering Department  
Howard University  
Washington, DC 20059

Professor Adrian Bejan  
Department of Mechanical Engineering  
University of Colorado  
Boulder, CO 80309

Professor Donald M. McEligot  
Department of Aerospace and Mechanical Engineering  
Engineering Experiment Station  
University of Arizona  
Tucson, Arizona 85721

Professor Paul A. Libby  
Department of Applied Mechanics and Engineering Sciences  
University of California San Diego  
Post Office Box 109  
La Jolla, CA 92037

Professor C. Forbes Dewey, Jr.  
Fluid Mechanics Laboratory  
Massachusetts Institute of Technology  
Cambridge, MA 02139

Professor William G. Characklis  
Dept. of Civil Engineering and Engineering Mechanics  
Montana State University  
Bozeman, MT 59717

Professor Ralph Webb  
Department of Mechanical Engineering  
Pennsylvania State University  
208 Mechanical Engineering Bldg.  
University Park, PA 16802

Professor Warren Rohsenow  
Mechanical Engineering Department  
Massachusetts Institute of Technology  
77 Massachusetts Avenue  
Cambridge, MASS 02139

Professor A. Louis Loudon  
Mechanical Engineering Department  
Bldg. 500, Room 501B  
Stanford University  
Stanford, CA 94305

Professor James G. Knudsen  
Associate Dean, School of Engineering  
Oregon State University  
219 Covell Hall  
Corvallis, Oregon 97331

Professor Arthur E. Bergles  
Mechanical Engineering Department  
Iowa State University  
Ames, Iowa 50011

Professor Kenneth J. Bell  
School of Chemical Engineering  
Oklahoma State University  
Stillwater, Oklahoma 74074

Dr. James Lorenz  
Composet Technology Division  
Argonne National Laboratory  
9700 South Cass Avenue  
Argonne, Illinois 60439

Dr. David M. Eissenberg  
Oak Ridge National Laboratory  
P.O. Box Y, Bldg. 9204-1, MS-0  
Oak Ridge, Tennessee 37830

Dr. Jerry Taborek  
Technical Director  
Heat Transfer Research Institute  
1000 South Fremont Avenue  
Alhambra, CA 91802

Dr. Simion Kuo  
Chief, Energy Systems  
Energy Research Laboratory  
United Technology Research Center  
East Hartford, CT 06108

Mr. Jack Yampolsky  
General Atomic Company  
P.O. Box 81608  
San Diego, CA 92138

Mr. Ted Carnavos  
Noranda Metal Industries, Inc.  
Prospect Drive  
Newton, CONN 06470

Dr. Ramesh K. Shah  
Harrison Radiator Division  
General Motors Corporation  
Lockport, New York 14094

Dr. Ravi K. Sakhuja  
Manager, Advanced Programs  
Thermo Electron Corporation  
101 First Avenue  
Waltham, MASS 02154

Mr. Robert W. Perkins  
Turbotec Products, Inc.  
533 Downey Drive  
New Britain, CONN 06051

Dr. Keith E. Starner  
York Division, Borg-Warner Corp.  
P.O. Box 1592  
York, PA 17405

Mr. Peter Wishart  
C-E Power Systems  
Combustion Engineering, Inc.  
Windsor, CONN 06095

Mr. Henry W. Braum  
Manager, Condenser Engineering Department  
Delaval  
Front Street  
Florence, New Jersey 08518

Dr. Thomas Rabas  
Steam Turbine-Generator Technical Operations Division  
Westinghouse Electric Corporation  
Lester Branch  
P.O. Box 9175 N2  
Philadelphia, PA 19113

**END**

**FILMED**

---

***1-86***

**DTIC**